3D Printed Components for Quantum Devices

Reece William Saint

School of Mathematical and Physical Sciences
University of Sussex

This thesis is submitted for the degree of
Doctor of Philosophy

January 2020

Declaration

I hereby declare that this thesis has not been and will not be, submitted in whole or in part to another University for the award of any other degree.

. . . . . .
Signature

Reece William Saint
January 2020

Abstract

Since the first demonstrations of laser cooling of atomic vapors in the late 1970s, the field of ultracold atoms has seen rapid advancements in the preparation, control and measurement of atomic gases. Ultra-cold atomic systems, either as individual atoms or in larger ensembles, provide a powerful tool for experimenters. Their large deBroglie wavelengths make them particularly useful for interferometric applications, and their isotropic properties when unperturbed make them ideal candidates for frequency standards. A recent drive has seen experimenters looking to develop scalable, portable and robust atomic systems as a metrological tool *outside* of the typical laboratory environment. This could see unprecedented sensitivities made available for areas as diverse as GPS-free navigation, biomedical imaging and non-invasive underground mapping.

Over the course of this thesis we explore additive manufacturing (3D printing) as a production technique for quantum technology. 3D-printing offers unrivalled design freedom and rapid prototyping, allowing us to develop a number of printed structures to test the viability of selective laser melting as a technique to produce metallic components that survive within, and also hold, the ultra-high vacuum environment necessary for ultracold physics. The technique has the potential to improve the efficiency and compactness of devices.

We begin first by printing an Al-Si-Mg vacuum flange, which is then solution heat treated in post processing and milled to have a standard vacuum-sealing knife edge on its surface. By installing the flange on a test vacuum set-up, baking out over a week at 200 °C and pumping down, a pressure of 10^{-11} mbar is achieved. In the same material, a conductive structure called the cylinder trap is printed as a proof of concept ultracold atom source producing the fields necessary for a magneto-optical trap. A complete cold atom experiment is constructed to test the device, including a simple microcontroller-based control system. Dissipating as little as 20 mW electrical power, the atom trap generates 10^8 atoms with an average temperature on the order of (20.1 ± 0.2) μK, whilst having no measurable effect on the vacuum pressure, measured as $< 10^{-10}$ mbar.

A next-generation device is then investigated, building on the work of the cylinder trap and consideration of contemporary work on cold-atom sources. This device would output an even colder source of atoms, with a tapered design to both act as a differential pump and for atom compression for transport to a secondary trap. With calculations on optimal trapping regimes, an Ioffe-Pritchard style magnetic trap layout is created to efficiently capture atoms from the magneto-optical trap. Atoms would then be transported through a three-dimensional funnel structure into a secondary magnetic trap where fast, evaporative cooling could occur. Simultaneously the next thermal cloud can be captured to improve the average cycle time. Encouraged by collaborative work on a additively manufactured chamber, called the coral trap, a prototype design is developed and presented consisting of the funnel structure split across a multi-chamber printed architecture.

Acknowledgements

This thesis and the work that contributed to it was written across two cities and across four and a half years, during which I have met and been helped by so many people, to list them all would be impossible.

Firstly, I want to thank my supervisors Peter Krüger and Fedja Oručević for offering me the DSTL studentship back in Nottingham, and for Peters guidance in particular throughout not just my PhD but during the whole of my undergraduate degree. That's almost ten years of supervision! Thank you too, to Ricky Wildman, Ian Maskery, Ehab Saleh, Sarah Everton and Laurence Coles from the Additive Manufacturing school and Added Scientific. The collaboration made my PhD possible.

The move to the University of Sussex, uprooting almost our whole research group, was a challenge for us all but it would not have been successful without Fedja and my laboratory partner Will Evans. The many drives between the two cities, helping each other move and even living together at Church Street was not what any of us expected at the start. The pay-off was well worth it though, and their patience with me as I adjusted to a very different lifestyle in Brighton was, and is, massively appreciated.

Our research group has always been incredibly collaborative, both in our research and socially. I must thank everyone in Nottingham for the endless discussions (arguments?) on physics, coffee, board games and dungeons and dragons, logic puzzles about British cooking, or lack thereof. Elisa, Sindhu, Fabio, Jorge, Amruta, Tim and Shob, Nathan and Sophie, and Xiaoke. Thank you all for being there for my (in)famous cocktail parties, and I can only apologize for butchering your languages after far too many pints at the Johnson Arms. A special thank you to Amruta and Anjan for letting me, Elisa and Sindhu be part of their wedding in India. A truly one in a lifetime experience I will never forget.

The time in Sussex introduced a new cohort of students and postdocs to the 'old gang' from Nottingham, without whom the group would be nowhere near as vibrant or interesting. We have boated, Mölkyy-ed, and played cricket together, although the last one caused an unfortunate wardrobe incident. Thank you to Helen, Rebecca and Emma for being the only truly organized ones out of us, and for your conversation up in the SINC office space. Thank you to Matt, for being as picky about coffee as I am, as well as always being up for a chat.

To all my Brighton friends, you can finally ask me what I was studying and I will actually answer properly. A massive thank you to Aimie and Spooner for Ibiza, superbed, and countless long nights, but especially for letting me be part of your wedding day. Thank you to the Orange Row gang, as well as Dexter, Igor, Grant, Ze, Duncan, Kelsey, Adam and Liam for being amazing friends over the last three years.

To all my family, thank you for being supportive over the many years of seemingly endless studying. I am *finally* no longer a student. My dad, for the many ale-fueled discussions on politics and science. My mum, for your constant support, and superhuman strength when stopping my kitchen being flooded. And to Adam, for keeping me grounded, and forcing me to learn how to cook my own Bolognese.

Finally, to Nick. Writing my thesis was perhaps equally as, if not more, stressful to you than it was for me. Yet throughout the process you have been supportive, loving and understanding. We made it to the other side together.

Table of contents

List of figures

Nomenclature

Roman Symbols

c	Speed of light in a vacuum inertial system
g	Gravitational Constant
h	Plank Constant

Acronyms / Abbreviations

AM	Additive Manufacturing
AOM	Acousto-Optical Modulators
BB	Baseball (trap)
BEC	Bose Einstein Condensate
CAD	Computer Aided Design
CF	Con-flat (flange)
FWHM	Full Width Half Maximum
GM	Grey Molasses (cooling)
GMOT	Grating Magneto-Optical Trap
HSF	Hyper-Fine Splitting
IGBT	Insulated Gate Bipolar Transistor
IP	Ioffe-Pritchard (trap)
LIAD	Light Induced Atomic Desorption
MOT	Magneto-Optical Trap
OPM	Optically Pumped Magnetometers
QUIC	Quadrupole Ioffe Configuration (trap)
Rb	Rubidium

RF Radio frequency

RMS Root Meat Squared

SHT Solution Heat Treatment

SLM Selective Laser Melting

SQUID Superconducting Quantum Interference Device

TTL Transistor-Transistor Logic

UHV Ultra High Vacuum, $< 10^{-10}$ mbar

Chapter 1

Introduction

1.1 Ultracold Atoms Intro

This thesis is written at an exciting time for the relatively new field of ultracold atoms, which is now a broad title covering a diverse number of disciplines with distinct aims. It would be ill-convinced to try and cover each of these sub-fields in detail. However, they all have one common theme, which is the manipulation of individual, or ensembles, of atomic systems with lasers, microwave and electromagnetic fields. Atoms make the ideal tool for physicists, being universal in their unperturbed behavior, and readily addressable with visible-light that is producible with cheap laser diodes. This makes them an ideal candidate for sensing and metrological applications where accuracy and consistency is critical. Conversely, the precise control of atoms, and their interactions, through magnetic or electrical manipulation has shown promise to use them as a toolbox for quantum simulation and computing applications.

The distinction between sub-fields has become more complex with a recent drive to begin developing experimental atomic systems as tools to be used *outside* of tightly controlled laboratory environments. Common elements between experimental laboratories are being re-evaluated, collated and streamlined to lay a pathway towards a truly portable atomic, and quantum, based device. The work presented in this thesis is part of this new wave of work, spanning the divide between purely fundamental physics and more applied systems engineering. Specifically we will consider the pursuit of a cold atom source through novel manufacturing processes. This source would be used as a first-step in an atomic, or quantum, device, providing a high flux of $10^7 - 10^8$ sub-millikelvin atoms directed towards a science chamber without being a detriment to its extremely-high vacuum (XHV, sub 10^{-11} mbar) environment.

This introductory chapter describes a brief historical timeline of the physics leading up to the development of ultracold atoms as a field. Following this, the general application of atomic systems as tools for sensing and metrology is discussed, outlining some of the current proposed techniques and implementations. This cannot rightly be considered alone, and as such a discussion of other applications of quantum systems is presented. Finally, an outline of the thesis is given to help guide the reader.

1.2 Historic timeline

The choice of where one choses to begin an historic overview of the physics around ultracold atoms is somewhat arbitrary. I choose to begin at the turn of the twentieth century to coincide with key experimental work on the nature of radiation pressure on light [1]. The idea of light having a measurable effect on matter was not at all novel, with references as far back as the 1600s speculating that part of the dust tails of comets were caused by light from the sun [2]. The contemporary measurements of the force imparted by light arrived in the context of a broader revolution in the understanding of thermodynamics, with Kirchoff's and Wien's discovery of the nature of blackbody radiation, and the debate over the nature of light itself. This debate saw the first twenty five years of the century being dominated by the 'household' names in physics such as Planck, Bohr, Compton and Einstein. This work saw the first theoretical framework for the *discreet* nature of light, coming in packets of $h\nu$, with ν being the frequency of the light and h being Planck's constant, which we now call photons. Parallel to this, experimental work on atomic systems suggested that atoms themselves have similarly discreet properties, both in their energy levels and angular momentum [3–7].

Further complicating the mixture of theoretical models and experimental work, Louis de Brogile suggested, in his PhD thesis no less, the wave-like nature of matter in 1924. This was quickly experimentally confirmed through electron diffraction and interference measurements [8]. It took the work of Heisenberg, Schrödinger and Born to weave together the patchwork of models and experimental data to form what we now refer to as *Quantum Mechanics*. The two formalisms presented, which are commonly referred to as the Heisenberg or Schrödinger pictures, gave the final keys to understanding the phenomena seen so far, and still form the backbone of quantum theory today [9, 10].

The relevant story for ultracold atoms jumps forward to the development of laser technology by Schawlow, Townes and Maiman [11] in the early 1960s. The technological advancement of a coherent and narrow-linewidth source of light was instrumental in many scientific fields, though for particular relevance to atomic physics it won Schawlow the joint Novel prize in 1981 with K. Siegbahn and N. Bloembergen for the precision determination of atomic energy levels.

Schawlow, Hänsch and Askin saw the early potential of lasers for use in trapping and cooling [12] of atomic systems in 1975, see also Wieman's review of diode lasers for atomic physics [13]. Askin first trapped micron-sized particles using counterpropagating beams [14], and proposed an atomic velocity selector [15], then finally suggesting a, now called, optical dipole trap for trapping individual atoms or gases [16]. This was followed by a surge of work first considering and then realizing the cooling (or de-acceleration) of atomic vapors using lasers [17–20]; however, critically this was not the *trapping* of atoms. The 'viscous confinement' reported in Ref. [20] became known as optical molasses, generating volumes of slow-moving atoms which would gradually escape the region through Brownian motion. This being the slow, random walk of particles experiencing random kicks resulting from the medium it occupies. It was soon proposed by Phillips, Metcalf and Prodan [21] to use a mixture of laser light paired with electromagnetic potentials in order to both cool *and* trap atoms, being achieved a few years later by Raab et al. in 1987 [22]. This construction of lasers and magnetic fields, which we now designate the magneto-optical trap (MOT), and the molasses method alone, achieved temperatures much lower than expected. Atoms were measured to

be only several microkelvin, far lower than the theoretically-predicted Doppler limit. Understanding and then making use of the sub-Doppler temperature effects became a key field of research [23–25]; however atoms in optical fields were still temperature-bound by the fundamental recoil-limit due to their spontaneous emission. Parallel research into sub-recoil techniques through more complex optical arrangements, such as through velocity selective methods or polarization gradients, were and still are an active field of research. [26, 23]

Transferring atomic ensembles into purely magnetic traps allowed for evaporative cooling methods to be carried out [27], where in a crude picture the hottest atoms are 'blown' away through the manipulation of the trapping potential with radio frequency fields. Given time to re-thermalize, the average ensemble temperature drops as a result. Evaporative cooling allowed for phase-space densities not accessible within MOTs, and was the last keystone in the seventy year puzzle of creating a Bose-Einstein condensate (BEC) with a weakly interacting gas. 1995 saw not just the first evidence of such a state of matter, but three separate groups achieving Bose-Einstein condensation with rubidium [28], sodium [29] and lithium [30]. The production of BEC with a weakly interacting system paved the way to explore new microscopic phenomena, and provided the tools necessary to better understand how inter-atom interactions behave and, critically for us, the potential to better exploit atomic systems for sensing and metrological purposes, which is the topic of the next section.

1.3 Sensing and metrology

Whilst the historic timeline above has taken us to the first demonstration of Bose-Einstein condensation in weakly interacting gases, it is worth now taking a step back to discuss the potential of atomic systems in the context of sensing and metrological measurements. The discussion will provide motivation to the importance of the work that follows in the later chapters. Further, the division between the fields is arguably artificial, and in reference to atomic sources there is a lot of overlap as much of the experimental apparatus is comparable, and so too are many of the applications. I direct the reader to some of the more recent reviews of the topic [31–33].

Time standard We first consider time measurements, and the development of optical frequency atomic clocks. The pursuit of a stable frequency reference, and so a fixed basic unit of time, has been historically driven by navigation on oceanic trade routes. Mechanical oscillators such as pendula, springs and later the vibration of quartz crystals became standard. The nineteen century saw the demand not only for much greater precision, but also a more universal standard with which to measure against. Precision devices could see applications not only in improving navigation, via the global positioning service (GPS), but also in questions as to the nature of the fundamental constants, forces and the accuracy of general relativity. Atomic systems, isotropic in their unperturbed properties, were proposed in the late 1800s [34, 35], where it was clear that the universality of atoms in regards to their 'vibrational modes' would make them ideal candidates.

It took until the 1950s for an atomic based reference to become more accurate than contemporary quartz standards [34, 36, 37], based on addressing the unperturbed hyperfine ground state transition of cesium 133 ($\sim 9.19 \times 10^9$ Hz), which now forms the standard by which we still define the

second[1]. The basic principle, see [34, 38], of the clock is based on Ramsey spectroscopy, whose accuracy is, in very simple terms, improved in accordance with Heisenberg's uncertainty principle. This is to say that the measurement uncertainty is reduced as the measurement time is increased, where the ratio of the two is loosely given by some factor of Planck's constant. The atomic reference experiences a two-stage microwave interaction separated by a time, ΔT and a resultant frequency uncertainty, $\Delta\nu$, of the measurement, which are related by $\Delta T \Delta\nu \sim L$, where L is the spatial length of the interaction area. Attempts to increase the interaction time and so lower the uncertainty on the frequency, led to initial developments into atomic fountains, where atoms are projected upwards and allowed to fall under the influence of gravity, almost simultaneously to the first cesium clocks [34]. However these were unsuccessful, being limited by the thermal distribution of the source atoms, which in turn also reduced the number of atoms returning in the second interaction phase. More recently atomic *optical* transitions, rather than microwave, are considered to be the next phase of national standards [35], where the achieved quality factor (Q-factor) has direct effects on the final clock stability and accuracy [38].

The relevance of atomic clock systems to this work, and a key step-change for the field, was the introduction of optical molasses to cool the ensemble prior to launching in fountain-based Ramsey spectroscopy techniques, first successfully implemented in the late 1980s [34, 39]. This method reduced the Doppler broadening effect on the cloud due to its overall temperature and so improve the final clock measurement. The ultimate lifetime of the launched ensemble, which is limited both by inter-atomic collisions in the cloud itself but also by background atoms, is a critical factor and is indirectly related to the cloud temperature.

Atomic interferometry and inertial measurement Parallel to the development of atomic clocks, the field of atomic interferometry has rapidly expanded in the last several decades, with a number of significant reviews into the topic being available [33, 40, 41]. Heavy atom interferometers, typically alkali metals, required similar developments in cooling mechanisms, such that their deBroglie wavelengths became significant enough (i.e. larger than the atomic radius) to make wave-like properties accessible to experiments. Optical based atom 'beam splitters' based on Raman transitions, first carried out by Chu [42], allowed for matter waves to be split coherently in two. After some interrogation time, T, the matter waves are made to recombined, having picked up a phase difference, leading to interference detectable through measurement of the population of one of the atomic states, see Ref. [33] for details. The imparted phase can be a result of a vertical path different due to gravitation effects, in which the gravitation-related phase difference, $\Delta\Phi_g$, goes as $\Delta\Phi_g \propto gT^2$ where g is the acceleration due to gravity [33, Sec. 2.1]. Similarly a *rotational* phase can be imparted, as is the case with Sagnac interferometers where the split matter waves are sent counterpropagating about a guided loop. Rotational motion in the plane of a ring around which the matter waves are sent can be found to scale as $\Delta\Phi_{rot} \propto \nu\Omega T^2$, where ν is the atoms linear velocity and Ω is the rotation rate of the Raman lasers [40].

Many of the applications of atomic clocks are similar to interferometric measurements, such as investigations into fundamental forces; however they have a particularly critical role in navigational precision, see the quite extensive state of the art review in Ref. [32, 33]. Similar too are the typical

[1] I could not rightly mention this definition of the second without also pointing out that now, since 2019, *all* Système International d'Unités (SI units) are derived from this and fixed definitions of fundamental constants.

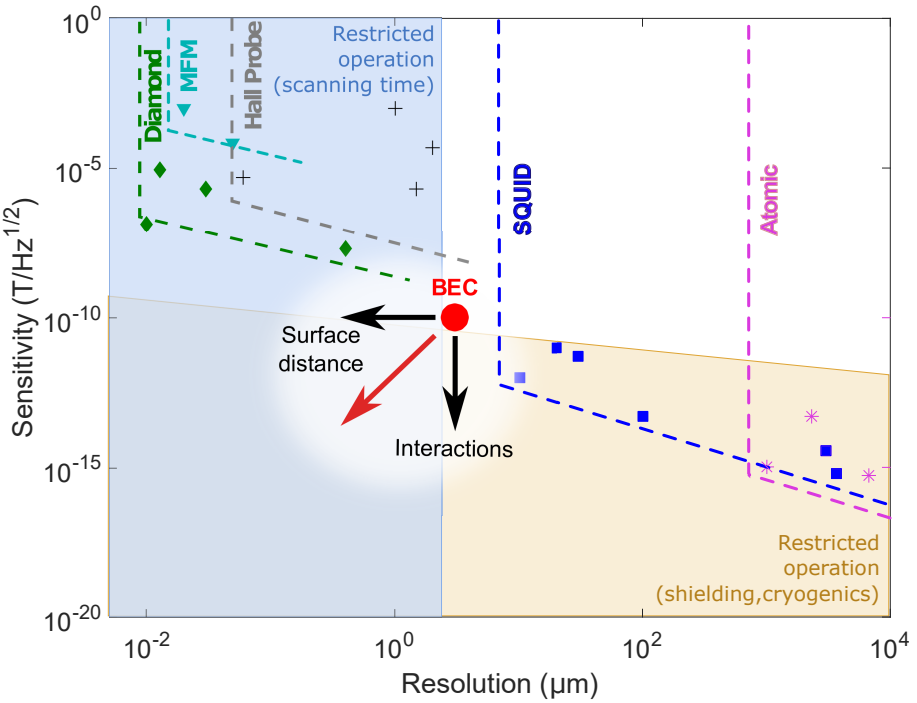

Fig. 1.1 A plot of different magnetometer's sensitivity vs resolution. Image edited from [51].

hurdles, in particular increasing the interrogation time under which the 'split' matter waves can be considered coherent and without significant losses due to collisions. Signal-to-noise ratios can be improved too through increasing the atom number. These examples are not at all exhaustive of methods to improve interferometric measurements specifically, but share a common link to our discussion on optical clocks.

Magnetometry The applications of non-invasive magnetometers are vast, having been a pivotal industrial and navigational tool long before more modern and widespread application in detecting sea mines in the 1940s. Modern magnetometry techniques are equally as broad in their realizations and I direct the reader to some of the more recent reviews on the topic [43, 44]. We can for our purposes categorize devices into those which typically measure [2] the total *scalar* magnetic field strength, such as optically pumped magnetometers (OPMs) [45, 46], nuclear/proton precession magnetometers [43], nitrogen vacancy (NV) centers [47], or magnetic force microscopy [48]; or devices which can measure the vector components of the field, e.g. flux gates, microelectromechanical magnetometry systems (MEMS, e.g. microscopic mechanical oscillators), hall effect sensors [44, 49], or superconducting quantum interference devices (SQUIDs) [50].

The above examples are not at all exhaustive, however they provide the necessary context in regards to their sensitivity and resolution, best summarized in Figure 1.1, to introduce the use of Bose-Einstein condensates as a more recent tool for measuring magnetic fields [51–53].

Bose-Einstein condensates offer a powerful improvement across all of the sensing and metrological applications discussed above. In regards to magnetometry, they can achieve both high resolution and sensitivity when compared to other techniques. The ultra-cold temperatures required by BECs

[2] Strictly many of the devices and techniques mentioned can be constructed to be either scalar or vector magnetic field sensors.

make them ideal for interferometric and frequency-time metrology [31], simply because they have a larger deBroglie wavelength. Getting to a BEC is technically challenging, with the typical hurdles experienced in metrology (collisional loses, temperature, signal-to-noise, to name a few) being completely destructive to the process. Portable, cold atoms sources, as we will consider in the next few sections, offer a potential solution to these issues both for BEC and cold atomic-vapor based technology.

1.4 Towards portable devices

The significant body of experimental work done since the development of laser cooling, slightly over forty years ago, would make it unfeasible to discuss every variation on the procedures used to experimentally realize atomic vapor-based devices. We will restrict out consideration to more recent work which attempts to develop complete atom-based systems which are portable[3]. This drive has required experimenters to rethink the experiments that, up to now, have had the benefit of laboratory infrastructure to support and house equipment. The result is that one must account for the whole experimental apparatus, including supporting electronics, vacuum structures, laser systems, computer/software control and power supplies.

It is ill-advised to take the leap directly from a laboratory-based experiment to a fully realized portable device, and so we will consider here the miniaturization efforts of a number of sub-components of a typical cold-atoms experiment. Namely, the reduction in optical components; the design of magnetic trapping geometries and vacuum technology. This discussion will form the basis on which we will then introduce *cold-atom sources*. This source will not aim to be a fully operative quantum sensor, but will be a sub-assembly with a specific functional aim: the output of a steady source of cold, or ultra-cold, atoms. This is distinct from the source of the atoms within the device, which is commonly a heated alkali dispenser.

Optical confinement A reduction in the number of optical components required is perhaps the simplest first-step one can take for miniaturization, as beams can be almost completely reflected with modern mirrored surfaces. In its simplest form, a magneto-optical trap typically requires three pairs of counter propagating beams, and so reflected three-beam MOTs are common place, and early work demonstrated a four-beam MOT [56]. However, *single-beam* realizations have been demonstrated. In these the beam is retro-reflected such that, with the correct reflector shape, all the necessary beams for a MOT are generated with the correct optical polarizations. Concave conical, pyramidal and tetrahedral single-beam reflectors have been shown to work well [57–60], with both interferometers [61] and gravimeters [62] being demonstrated. Where atom chips provide a significant simplification in the design of conductor geometries to generate magnetic potentials, single beam designs offer a similar simplification in the optical requirements on the overall device.

Microfabricated diffraction gratings are a natural successor to three dimensional reflectors and have shown great promise in the trapping and cooling of atomic species [63–66]. Diffraction gratings, like atom chips, are significant as they are very amenable to modular and scalable designs by being easier to produce in bulk than large macroscopic conductor structures. Although they

[3]The full breadth of the technological and industrial implications I will leave to Refs. [33, 32, 54, 55].

do suffer in their achieved atom numbers, often only reaching $\sim 5 \times 10^6$ atoms. Magnetometry measurements have been carried out in Refs. [66], and gravitometry measurements planned in this same reference suggest that such devices may be 'good enough' for a first generation proof of principle.

Magnetic trapping structures With the establishment of laser and evaporative cooling of atoms, there was then a rapid development of bespoke magnetic potentials with which to manipulate the clouds. The first attempts were free standing wires [67–70], which in their proximity to the atoms in comparison to large mounted coil systems would be better suited to the design of complex magnetic geometries. This process truly took off with the development of what we now call *atom chips*, in which metallic conductors are layered in two-dimensional geometries generating magnetic potentials only sub-millimeters from the surface. See Refs. [71–73] for a more in-depth review of the field.

Atom chips fall incredibly well into the goals of a miniaturized device, being able to produce highly-confining, complex traps with only modest currents when compared to older BEC experiments. Advances in manufacturing methods have seen bespoke atom chips designs better fitting the various sensing and metrological applications we have already discussed [74]. Modern atom chips typically employ a staged series of traps, initially capturing atoms from a magneto-optical trap, whose magnetic potential is provided by a separate coil structure, then bringing the now purely magnetically trapped atoms in closer to the chip surface to be transferred to tighter confinement traps. Correct arrangement of this sequence of traps has allowed total BEC formation cycle times to shrink below one second [75]. However, in having the MOT in the same volume there still exists a detrimental background pressure to contend with. Nevertheless, such chips are likely to be a critical component in any future BEC-oriented experiment, being the final stage of manipulation and interrogation atoms experience until imaging.

Vacuum systems As systems get smaller, the typical processes used to 'pump-down' the interior volumes of quantum devices from air pressure to ultra-high vacuum (UHV), $\sim 10^{-11}$ mbar, become more constrained. Vacuum pumping is of course not necessary for all applications; hot-atom OPMs for example make use of buffer gas effects on the sensing atoms such that they can operate at room temperatures and pressures, sometimes even being heated to increase the pressure. Miniaturized UHV chambers have restrictive volumes, by design, with only narrow connecting passaging to which vacuum pumping devices could be connected. Novel pumping processes based on passive adsorption elements paired with smaller active pumps could be a solution [76]. Conversely there has been work in improving the atom source, typically hot dispensers, either through redesigned dispensers [77] or through ultra-violet light driven emission [78] of atoms into the chamber.

Cold atom sources Attempts to miniaturize systems have obvious cross-overs with attempts to develop a reliable source of (ultra-) cold atoms, as the cooling of atoms from a hot atomic vapor to sub-millikelvin temperatures requires a significant volume of equipment. The methods used are often identical across research labs, and so many experiments are either maintaining systems that have been in place for many years or re-inventing the same solutions for newer experiments. A

modular device which outputs a flux of cold atoms, in a crude plug-and-play analogy, would be a remarkable simplification to the typical cold-atom experiment.

Reflector- and grating-based systems are a noteworthy example a potential modular source of atoms [59, 64]. This method has been extended with attempts to create a grating-Zeeman slower hybrid [79], showing a three-fold increase with respect to just a grating. A controllable 'atom faucet' where a continuous push beam ejects atoms from a three-dimensional MOT shows some promise [80], as well as compact and low-optical power two-dimensional MOT systems [81, 82]. The common theme of these latter cases being the production of MOT-temperature atoms in a specific region, to then be transported or pushed to another area. Magnetic guiding of atoms from a MOT has been proposed too, either using permanent magnets [83, 84], with the potential benefit being overcoming the laser-imposed recoil limit on the temperature. A noteworthy example of a BEC source, rather than a thermal atom cloud, is in Ref. [75] where a 1.6 s production rate is achieved from vapor to condensate with a multi-staged atom-chip design.

1.5 Additive manufacturing as a tool for quantum technologies

Collating the different approaches to miniaturization of ultra-cold atom based devices, it becomes clear there are still a significant number of hurdles to overcome. There is, however, some very encouraging work on complete experimental packages, especially in the field of space-based applications [85–88].

Outside of large international collaborations, one promising avenue of research is the exploration of new manufacturing processes to replace, or augment, existing technology and techniques. Having set the contextual framework of the field of ultra-cold atoms in precious sections, we now introduce additive manufacturing (AM) as a novel method for the creation of quantum devices. Additive manufacturing, or 3D-printing which we will use interchangeably, has the potential to be incredibly disruptive to the manufacturing industry. The most common benefits being material savings, ease of customization and the production of complex, almost arbitrary geometries not easily possible through traditional manufacturing methods. Please see Ref. [89] for an in-depth review.

3D-printing has now become an umbrella term to capture quite a broad range of processes, from the production of nanoscale devices to the printing of whole components for aerospace or industrial applications. The choice of technique sets practical limits on the dimensions of the device, but also on the available materials. The application to ultra-cold atom experiments imposes further criteria: structures must not *outgas*, that is desorb particles into the vacuum, and must be dense enough to restrict particles diffusing through the material; structures must also survive temperatures up to 200 °C and be ridged enough to be self supporting. As one of the key methods in producing components for aerospace applications, selective laser melting (SLM) presented itself as a strong contender to fit our requirements. This technique, in brief, is the construction of monolithic components through melting of successive layers of a power-based metallic alloy, producing objects with a resolution in the range of $100 - 250\,\mu$m. It became an interesting avenue to pursue as the materials currently available fit into the 'tried and tested' material library of typical experiments, that being titanium, stainless steel, silver and aluminum.

We consider this technique for two applications within quantum technology. One being the production of bespoke monolithic vacuum-containing structures, i.e. vacuum chambers, with unique and complex features not achievable through standard processes. Similar attempts to create UHV-sufficient chambers were unable to reach the level of vacuum required for typical cold and ultra-cold experiments [90–93]. The second application is the more novel use of AM structures as conductors within UHV environments producing magnetic fields, which has not been carried out before as far as the author is aware. Conductors printed with complex geometries fitting around, or within, the bounds of miniature devices could provide significant benefits in terms of overall system size and electrical power consumption to produce magnetic trapping potentials. Whilst the previous work to produce UHV quality devices with AM technology suggested it may not be feasible [92], we benefitted from a collaboration with a additive manufacturing research group within the University of Nottingham who suggested that newer developments in printing technology may prove fruitful.

1.6 Applications of AM in portable quantum technology

So far the discussion of atomic systems and additive manufacturing has outlined applications in physics and engineering. However, one of the major driving forces in atomic research establishments, and the agencies which fund them, is the potential of atom-based technology as an enabling tool for fields well outside of the traditional sphere of influence associated to physics. Precision timekeeping is fundamental to financial institutions, electrical distribution grids and tamper-free GPS navigation to name a few. Similarly, measurement and sensing devices are hidden, yet keystone technologies in nearly every industrial field, e.g precision metallurgic analysis, civil engineering, geological exploration.

The true revolutionary potential of atom-systems really comes to light in devices which have the same, or similar, accuracy of lab-based experiments but are portable, robust and reliable. The author points the reader to reviews such as in Refs. [32, 55], though there exists similar politically-aimed reports for the EU, the United States and elsewhere. Researchers and engineers have speculated about atomic sensors which can be mounted onto drones to map landscapes, oceans, or even measure the heartbeat of farm animals. Archeological digs could measure minute gravitational irregularities to detect structures, while submerged craft would be more able to navigate underwater hurdles and even remain submerged longer if their measurement equipment were more precise. This work explores additive manufacturing as a stepping-stone towards such a device. As a novel production technique there is the potential to make significant mass reduction, while integrating complex geometries to create a space-efficient measurement device, potentially even reducing power consumption. Researchers typically do not have to worry about the mass, power consumption or size of their experiments; however, real-world applications require a thorough understanding of how to reduce each.

1.6.1 Thesis overview/structure

The investigation of additive manufacturing in the context of quantum devices is the focus of the work in this thesis. One publication is derived from it directly, *3D-printed components for*

quantum devices [94], and a second paper written in collaboration with the University of Nottingham and industry partner Added Scientific is pending acceptance, with a preprint available under the title *Additively manufactured ultra-high vacuum chamber below* 10^{-10} *mbar* [95]. These papers demonstrate, for the first time, additively manufactured material used within, and containing, a UHV environment. In application to quantum devices, these publications open the door to drastically improve integrated structures, which will further reduce size and assembly complexity.

- **Chapter 2: Cooling and trapping of atomic species** In this chapter an outline of the necessary physics to understand the cooling and trapping of atomic species is given. This begins with a review atomic structure and the nature of light and matter interactions, followed by a discussion of the principles of optical molasses, magneto-optical trapping and finally magnetic trapping. Magnetic trapping structures, in particular how we calculate simple and more complex geometries, will be reviewed such that a comparison can be drawn between trap types, seeding the design of additively manufactured conductors.

- **Chapter 3: The cylinder trap** As a proof of principle, we first consider the production of a 3D-printed structure designed to exist in a UHV environment and producing the fields required for a magneto-optical trap. This chapter covers the design process and considerations of the device which we call the cylinder trap, which is eventually printed via SLM in an aluminum-silicon-magnesium alloy. Following this, a simple cold-atom experiment is outlined and constructed to test the performance of the cylinder, both in terms of the achieve atom number with respect to the power consumption, but also if there are measurable vacuum pressure effects due to the material.

- **Chapter 4: Blueprint for a cold-atom source** Building on the results of the cylinder trap, I then discuss a next-generation device which is designed to output a colder, high-number cloud of atoms at a increased cycle rate than the cylinder trap. A series of calculations are carried out in order to maximize the efficient transfer of atoms as they are manipulated between trapping stages along a three-dimensional funnel structure, before they are rapidly cooled and then ejected into a secondary science region. The coral chamber, a additive manufactured vacuum chamber, is presented along side these calculations. A prototype design is presented, combining the funnel like structure with a 3D-printed two-staged vacuum chamber.

- **Chapter 5: Summary and outlook** The main results and findings from the thesis are presented for reference, with an outline of some of the challenges encountered in the experimental work. Prospective for additive manufacturing in quantum technologies are discussed in the context of these findings.

Chapter 2

Cooling and Trapping of Atomic Species

In this chapter will provide an overview of the theoretical concepts required to understand the cooling, trapping and manipulation of atom species in reference to the production of magneto-optical traps (MOTs) and magnetic traps. The very basic models and physical processes described are not novel, and so the descriptions will be concise when appropriate as now countless textbooks, review articles and lecture series provide a broader picture, a selection of which will be given for reference. I will begin with an overview of the atomic structure of rubidium, followed by the interaction of atoms in magnetic and optical fields. These lead naturally into a discussion of the Doppler cooling, molasses effects, and the production of MOTs; this of course necessitates a description of sub-Doppler effects. Calculations of magnetic trapping potentials for various structures will be considered and compared for their use as magnetic traps for atomic species. As the aim of this work was the production and development of a cold-atom source, the above provides the necessary background. Only a very brief discussion of Bose-Einstein condensation will be given to paint the prospective landscape and motivations of the work.

2.1 Atomic structure

Alkali atoms have become the dominate choice for (ultra-)cold atomic experiments due to their relative ease in being cooled and trapped [96, Sec. 4], as well as having conveniently accessible energy levels via now standard off the shelf laser diode systems. Further, introducing such atoms into an experimental volume is readily achievable with heated atomic dispensers providing a reliable and consistent source of thermal atomic vapors. The multi-electron alkali atoms do not have exact analytical solutions to their Schrödinger equation, making it difficult to accurately capture their full dynamics. However their main attraction from other many electron atoms is their ready approximation to a hydrogen-like system [97, Sec. 10]. While having a number of electron shells, each designated by the *principle quantum number n*, alkali metals have all but one of these shells filled, leaving a singular electron in an outer shell. The inner core of filled shells are spherically symmetric when time averaged, resulting in a net atomic core that is effectively neutral, allowing for the outer electron to dominate the overall atomic properties. The extend of the core is small enough in this model that one need only consider a slightly approximated version of the Coulomb potential [98, Sec. 6.3] when calculating interactions. In the case of rubidium, as will be the sole

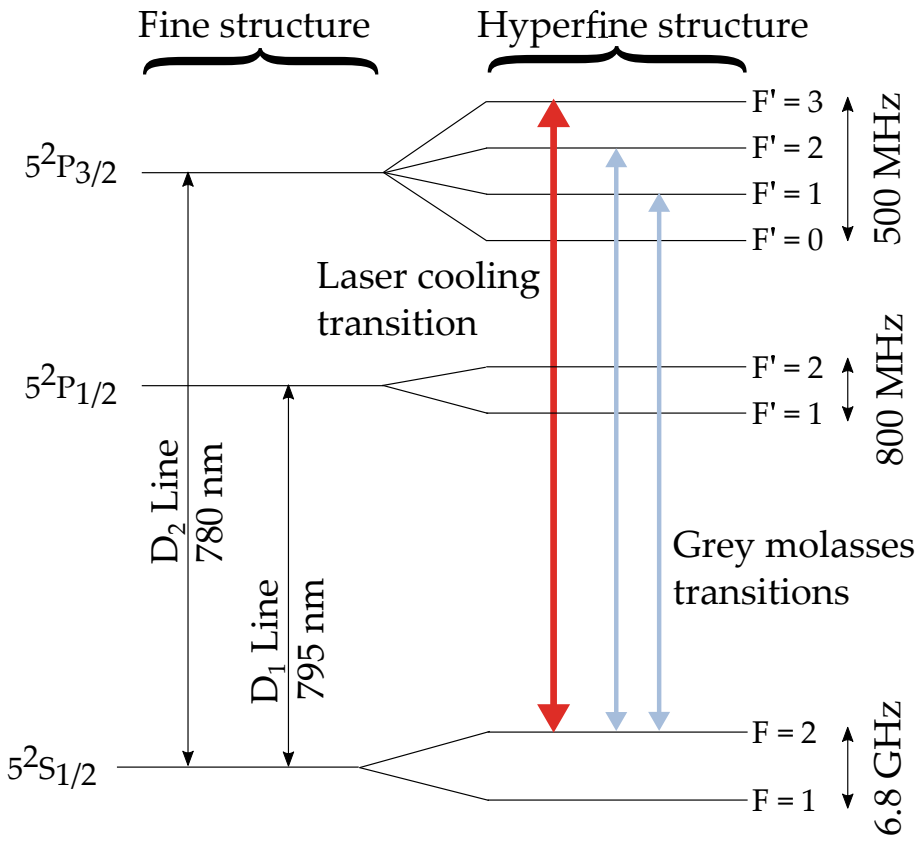

Fig. 2.1 The D1 and D2 lines for ^{87}Rb including both the fine and hyperfine structure, see check for details. Depicted too is the main laser cooling transition and the two commonly used Grey Molasses cooling transitions used for sub-Doppler cooling, see Sec. 2.2.4.

considered atomic species in this work, we can then consider only its outer electron designated 5s in standard electronic configuration notation.[1]

Similar to the route standard texts follow for hydrogen, we can then understand the various atomic energy levels of alkali systems within an adjusted formalism. The single electron in our Rubidium 'hydrogen-like' system, omitting the nucleus for now, is completely determined by its orbital angular momentum l and spin angular momentum s. As the closed shells are disregarded we can go ahead and consider the *total* orbital and *total* spin angular momentums as $\vec{L} = \vec{l}$ and $\vec{S} = \vec{s}$, respectively, where we define the total electronic angular momentum of all electrons as $\vec{J} = \vec{L} + \vec{S}$. These allow us to now introduce the standard Russell-Saunders notation [96] where $n^{2S+1}L_J$. It is the coupling interaction between the electrons orbital motion and its internal magnetic moment, aka the *spin-orbit interaction*, which generates what we refer to as the fine-structure of the atom, lifting the degeneracy on states that have differing orientation of the vectors $\vec{L}$ and $\vec{S}$. More explicitly, we have states of values J between $|L-S| \leq J \leq L+S$. The most common occurrence of this splitting are the D lines which result from transitions between states with $\vec{L} = 0$ and $\vec{L} = 1$ [9, Sec. 6.5.2], as are shown in Fig. 2.1 for the case of ^{87}Rb.

With non-Doppler-limited measurement techniques it is possible to resolve atomic structure with a much finer separation than the fine-structure produces, denoted as the *hyperfine structure*.

[1] The full electron shell configuration is $1s^2 2s^2 2p^6 3s^2 3p^6 3d^{10} 4s^2 4p^6 5s$ where the notation $n\ell^e$ gives the principle quantum number, n, the angular momentum, ℓ, and the exponent is the shell occupancy [99].

This results from the as-of-yet disregarded atomic nuclei's angular momentum, I, also called the nuclear spin, related to a nuclear magnetic moment. This nuclear magnetic moment interacts both with the internal magnetic field generated by the nuclear electrons (those in filled shells), and with the single outer electrons magnetic moment [98, Sec. 5.7]. As a result we introduce a new term, the total atomic angular momentum $\vec{F} = \vec{I} + \vec{J}$ which can take the values $|J - I| \leq F \leq J + I$. In the case of ^{87}Rb, $I = 3/2$ and so the ground state $J = 1/2$ splits in to two levels, $F = 1$ or $F = 2$; similarly the $5^2P_{3/2}$ level splits into four sub-levels between $F = 0 \rightarrow 3$, both cases are shown in Fig. 2.1.

2.1.1 Zeeman splitting

The majority of this work considers atomic species in the presence of externally-applied optical and magnetic fields. We will not explicitly deal with the effects of optical fields on atomic energy levels, i.e. the Stark shift, but will touch on it later when we consider sub-Doppler cooling effects in atomic vapors. Magnetic fields specifically can be shown to lift the degeneracy of the so-called Zeeman sublevels of the atomic structure [96], which for each fine structure level can be shown to be made up of $(2J+1)$ sub-states. Considering, just for now, the effect of an externally applied magnetic field one reaches the regime of the so-called (anomalous) Zeeman effect[2]. At low field the Zeeman interaction energy can be written as $\Delta E_{Zeeman} = m_F g_F \mu_B B$ where m_F is the projection of the angular momentum along the vector $\mathbf{B}$ which is the magnetic field strength; μ_B is the Bohr magneton; and g_F is the Landé g-factor which is a correction to the usual g_J which accounts for the nuclear spin, given below. We define low fields here in terms in interaction energy, such that the Zeeman interaction energy $\Delta E_{Zeeman} < \Delta E_{HFS}$ where the latter term in the hyperfine structure interaction energy [98].

$$g_J = 1 + \frac{J(J+1) + S(S+1) - L(L+1)}{2J(J+1)}, \tag{2.1}$$

and

$$g_F = g_J \frac{F(F+1) + J(J+1) - I(I+1)}{2F(F+1)}. \tag{2.2}$$

For ^{87}Rb, the Zeeman effect is approximately linear for fields $\lesssim 300\,\mathrm{G}$ [100]. For fields greater than this, where $\Delta E_{Zeeman} > \Delta E_{HFS}$ the coupling between the electron and nuclear spin becomes negligible and the levels are completely determined by the electron spin interaction with the external field. This is the *Paschen-Back* effect, and will in general not be approached in this work [10].

2.2 MOT principles

2.2.1 Forces on an atom

The ability to manipulate large numbers of atoms in order to then probe fundamental physics, or as a tool to measure other systems, is a non-trivial achievement. It requires the confinement of

[2] There is a potential source of confusion here. Anomalous is typically used for the Zeeman effect for externally applied magnetic fields, distinguishing it from the Zeeman effect from, say, internally generated magnetic fields.

atoms within a region of interest for a sufficiently long time, free from interactions with other systems or particles such that significant measurements can be taken [98]. Experimentally these requirements mean that atoms must not be too hot, i.e. have a low average velocity, such that their preparation and interrogation time within a bound experimental region is sufficiently long. They must also exist within an environment free from contaminants or stray electromagnetic fields. These stray fields are removed experimentally through special consideration of materials and in some cases shielded environments, while contaminants are removed through vacuum pumping and bake-out techniques. In regards to atom temperature, the preparation of, or more specifically the cooling of, atoms is underpinned by the realization that light itself imparts not only energy but also momentum onto matter, which was considered in the early nineteenth century [1, 2]. However it took the development of reliable coherent laser sources to truly begin to speculate that particles and then atoms could be manipulated with this radiation force [14–16]. It is this, paired with an understanding of the nature of spontaneous emission [96], which has formed the keystone of the laser cooling of atoms and in turn subsequent work on the cooling *and* eventually trapping of atomic species [101]. We will first consider the basic forces of an atom within a radiation field, naturally leading on to a brief discussion of the Optical Bloch Equations (OBEs) which will be required to then discuss how spontaneous emission can be understood within the OBEs formalism through the introduction of a damping term. The solutions of these then go on to inform our understanding of the production of a magneto-optical trap and sub-Doppler cooling processes.

Atom in a radiation field

We begin our consideration with the semi-classical model of a quantized two-level atom within a classically considered radiation field, which adequately describes most of the physics used in this work [99]. The oscillating electric field acts as a perturbation on our atomic system, coupling to the electric dipole, **d**, of the atoms single electron, and can be written as a plane wave with (angular) frequency ω_L and polarization vector $\vec{\varepsilon}_0$ in the form $\vec{\mathscr{E}}(t) = \mathscr{E}_0\vec{\varepsilon}_0\cos(\omega_L t)$. Our atomic system is described as two energy states, using Dirac notation, a lower ground state denoted $|g\rangle$ and an upper excited state $|e\rangle$; these are seperated in energy by $\hbar\omega_0$, where ω_0 is the atomic transition frequency between the two levels. The interaction energy between the induced dipole and electric field can then be shown to be [96, Sec. 1.2] as $H_{int}(t) = -e\vec{\mathscr{E}}(t)\cdot\vec{r}$, where $\vec{r}$ is the position of the electron relative to the atoms center of mass, and e the charge on the electron. This system can be solved with the time-dependent Schrödinger equation, with a number of approximations. We first take the dipole approximation: the amplitude of the electric field is assumed not to vary across the size of the atom a_0, i.e. $\lambda_L \gg a_0$, which for our situation is reasonable when light of 780 nm is used. The second assumption is the rotating-wave approximation [99, Sec. 7.1.2], which allows for terms of the type $\omega_L + \omega_0$ in the derived Hamiltonian to be omitted. The solutions, not given here, demonstrate so-called Rabi oscillations between the population of the excited and ground states, which is determined both by the detuning of the laser from resonance and the Rabi frequency, $\Omega = -\frac{d\cdot E}{\hbar}$, which characterizes the strength of the coupling between the atom and field[3]. This Rabi

[3] $\Omega = -e\frac{\vec{\mathscr{E}}_0}{\hbar}\langle e|r|g\rangle$ where the dipole momentum $d = e\vec{r}$ is along the same polarization direction as the field, and has been substituted into the expression. Outside the bra-ket, e is the usual charge on the electron. $\langle e|$ is the excited state bra vector, and $|g\rangle$ the ground state ket vector.

behavior is not predicted by the classically derived rate equations, and can allow for almost perfect population inversion between the ground and excited state of a two-level system.

So far we have not dealt the incoherent process of spontaneous emission, however this process is essential to the understanding of laser cooling. These incoherent effects do not fall out of the simplified semi-classical mode, but require a full quantum picture of both the atomic system and the incident radiation field, i.e. a Quantum-Electro-Dynamic model, however this is too heavy handed for our needs. In order to integrate spontaneous behavior into our atom-light system, we first must introduce the density matrix, ρ, which for a simple two-level system in an initial pure state $|\Psi_i\rangle$ can be written as,

$$\rho = |\Psi\rangle\langle\Psi| = \begin{pmatrix} \rho_{gg} & \rho_{ge} \\ \rho_{eg} & \rho_{ee} \end{pmatrix}, \tag{2.3}$$

where the main diagonal elements are the populations of the ground and exited states respectively, and the off-diagonal elements are generally called the coherences, providing phase information about the superposition of different components [102]. The power of such a description is that we can readily describe an initially defined pure state transforming into to a statistical mixture of final states. Such a model is required for spontaneous emission as, by its nature, the light is isotopically emitted with arbitrary polarization, effectively being infinite in modes. Although to be precise, we have not yet introduced spontaneous emission mathematically into our formalism. Thus only a statistical representation is practical. The statistically defined density matrix is then written as $\rho = \sum_i p_i |\Psi_i\rangle\langle\Psi_i|$, where p_i is the probability to be in some state $|\Psi_i\rangle$. Now considering the detection of a two-level atom, which is in an initial pure state $|\Psi_i\rangle$ which has undergone spontaneous emission, we can write its new statistical mixture of states in the form $\rho_{atom} = \mathrm{Tr}_{photon}|\Psi\rangle\langle\Psi|$, having taken the partial trace over system with respect to the photon. While we have lost information through the trace about the photon, this method allows us to describe the behavior of the atom in this statistical model. Without going into the gritty details [96, 99] one can then introduce spontaneous emission into the density matrix formalism through the addition of a damping term Γ, and in turn derive a steady-state ($t \gg \Gamma^{-1}$) equation for the excited state population as follows:

$$\rho_{ee} = \frac{\Omega^2/4}{\delta^2 + \Omega^2/2 + \Gamma^2/4}, \tag{2.4}$$

having now introduced the detuning, $\delta = \omega_L - \omega_0$. We can finally relate Eq. 2.4 to the rate of spontaneous emission, or the *scattering rate*, Γ_{scatt} by realizing that the decay rate from the excitation population is the natural linewidth of the transition in question, Γ. The total scattering rate in the steady state limit where the photon excitation rate is equal to the decay rate is then,

$$\Gamma_{scatt} = \Gamma\rho_{ee} = \frac{\Gamma}{2}\frac{\Omega^2/2}{\delta^2 + \Omega^2/2 + \Gamma^2/4}. \tag{2.5}$$

Scattering force

In order to relate the total scattering rate in Eq. 2.5 to an expression for the scattering force, we slightly re-construct our expressions to relate the Rabi frequency Ω to the more experimentally understandable relative saturation intensity I/I_{sat} [98]. Considering circularly polarized light, one

then can write $I_{sat} = (\pi/3)(hc/\lambda^3)\Gamma$[99, 103] which is purely determined by the atomic species and transition being addressed, and the ratio $I/I_{sat} = 2\Omega^2/\Gamma^2$. While we have made the assumption that our light field is strictly non-quantum, we *can* assume a photon based description such that each absorbed photon has a momentum $\hbar\vec{k}$ [99, Sec. 9.1] [4]. Once the atom undergoes spontaneous emission the photon is isotropic in direction and polarization and imparts a recoil on the atom as per Newton's laws. Over many emission cycles the average momentum given to the atom by this recoil is a net zero, and so the only change in the final momentum is given by the initially absorbed photon interaction. The resultant force on the atom is then the product of the photon momentum and the scattering rate (in steady-state), such that,

$$\vec{F}_{scatt} = \hbar\vec{k}\frac{\Gamma}{2}\frac{I/I_{sat}}{1+4\delta^2/\Gamma^2+I/I_{sat}}\,. \tag{2.6}$$

Note that we now consider the detuning $\delta = \omega_L - \omega_0 + \omega_D$, where $\omega_D = -\vec{k}\cdot\vec{v}$ is the Doppler shifted frequency seen by the moving atoms. From Eq. 2.6, we can quickly see that in the case of large saturation intensities, $I \to \infty$, the force tends to $F_{max} = \hbar k\Gamma/2$.

The expression in Eq. 2.6 above is for the general case of an atom passing through a beam of any direction. Lets now consider atoms leaving some thermal bath at some temperature T moving along a single axis counterpropagating to a laser. We can then find a maximum linear deacceleration for an atom of mass m, i.e. $a_{max} = F_{max}/m = v_r/2\tau$. Here we have defined the recoil velocity as $v_r = \hbar k/m$, which is the photon momentum over the atomic mass, and $\tau = 1/\Gamma$ is the excited state lifetime. We have also dropped our vector notation for this one dimensional situation. In the ideal case where atoms experience a constant deaccelerating force, one can then calculate a minimum stopping length [96, Sec. 6.2] assuming an initial velocity of the rms value for atoms, such that

$$L_{min} = v_{rms}^2/2a_{max}\,, \tag{2.7}$$

where $v_{rms} = \sqrt{3k_BT/m}$, in which k_B is the Boltzman constant, T the average temperature and m the mass of the atoms. This minimum stopping distance is not at all appropriate for our needs in the case of a mostly monochromatic beam, as in the case where the light used is narrow in regards to a transition linewidth. Atoms in such a light field quickly leave resonance as they slow down due to the change in their Doppler shifted frequency. The expression for L_{min} however will provide an estimate for calculations later. To achieve significant continuous cooling the varying Doppler affect must be accounted for, either by varying the laser frequency or by changing the atomic resonance frequency through a inhomogeneous magnetic field, as per the Zeeman effect in Sec. 2.1.1, experimentally known as a Zeeman Slower [12, 18, 19]. Zeeman slowed atoms may at first appear to be an appropriate source of cold atomic species; however, if one calculates the required stopping distance L_{min} for a diffusive source of ^{87}Rb atoms from an oven ($T \approx 600\,\mathrm{K}$) in its D_2 transition and irradiated with a counter propagating laser of frequency of 780 nm, $L_{min} \sim 0.8\,\mathrm{m}$. Such a length is completely inadequate for compact and/or portable systems.

[4] Strictly speaking, we have not broken our assumption but rather chosen to describe the absorption of energy using the physically imprecise, but convenient, terminology of photons whilst keeping in mind it is the atom itself which is quantized.

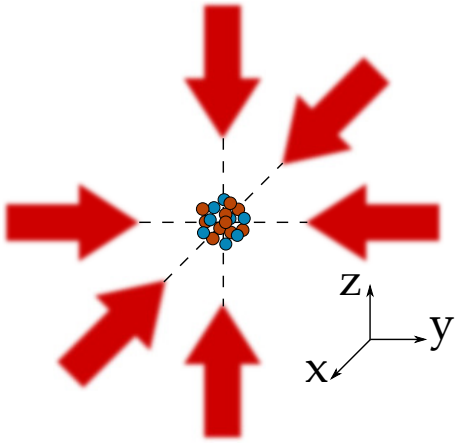

Fig. 2.2 Three cartesian pairs of counterpropagating beams form a volume within which atoms experience a frictional force as they pass through. Atoms are not trapped but appear to coalesce in the overlapping region as they are cooled, and so pass slowly.

2.2.2 Optical molasses

Extending the idea of a single laser scattering off a diffusive atomic source, consider now the effect on our atoms of two counter-propagating beams with identical characteristics. Each beam will act on the atoms with a force described by Eq. 2.6, such that atoms at rest will have a net zero force due to the equal and opposite force of each laser. However, for any velocity greater than zero, the atoms will see a different Doppler-shifted frequency relative to the propagation direction of the atoms against the beam axis. If the laser light is specifically chosen to have a detuning below the atomic resonance, atoms moving with a velocity vector direction opposite to the beams k vector see blue-shifted light, which is closer to resonance, whilst the other beam is further red-detuned. The result is, for atoms which small velocities, an imbalanced force that is velocity dependent and, in effect, induces a damping force. When three sets of counter-propagating beams are used the technique generates a volume of slow moving atoms, usually referred to as Optical Molasses (OM,), see Fig. 2.2. This technique was a step change in the manipulation of atoms and earned the Nobel Prize in 1997 [18, 20, 21, 104]. The theory presented here below is well documented within many standard textbooks [96, 99], and quite neatly outlined by Phillips and others in reference [25].

Sticking to our one dimensional case, we take Eq. 2.6 where each has a Doppler shifted frequency $\delta \pm kv$ where the positive (negative) case is closer (farther) to resonance as it is against (co-propagating along) the velocity direction. One can write a net force as follows, in the regime of small velocities,

$$F_{molasses} = -\alpha v = 4\hbar k^2 \frac{I}{I_{sat}} \frac{-2\delta/\Gamma}{[1+(2\delta/\Gamma)^2]^2} v, \tag{2.8}$$

where we assume $kv \ll \Gamma$, and so higher order terms are ignored [25]. We see directly from Eq. 2.8, that the damping term α is only positive for the red detuned case when $\delta = \omega - \omega_0$, confirming the above. The result of Eq. 2.8, is that any atoms which enter along the axial direction will be slowed and cooled, within some timescale to be discussed, without the need for a spatial variation to induce a Zeeman or Stark shift in the energy levels, nor without a similar frequency shift in the

laser light. However, the expression in Eq. 2.8 does not describe a restoring force; atoms will be cooled but will *not be trapped* within the beam volumes.

This 1D description can be readily scaled up to a three dimensional case, taking the more physically realistic model of atoms moving within a volume defined by three counterpropagating beams, each pair along the three cartesian axis. Each cartesian pair of beams, as in Fig. 2.2, can be considered to have a similar force profile as described in Eq. 2.8. Calculating the removal of kinetic energy along each cartesian coordinate, one can then find an estimate of the total energy removed. From this one can calculate the damping time $\tau_{damp} = m/2\alpha$ [99, Sec. 9.3], which is the time to approach zero velocity within the volume of the beams. Paired with our expression for L_{min} in Eq. 2.7, this defines an upper limit which we call the capture velocity, v_c, below this atoms will be cooled within the effective length the atom sees. Atoms at or below v_c will be, by the description of the dynamics given by Eq. 2.8, slowed to exactly zero velocity, or temperature[5], which is of course non-physical, or impossible more accurately.

There are a number of hidden dynamics to the system of atoms trapped by optical beams which have not so far been discussed that avoid this unphysical result. The first of which is the so-called Doppler limit, which naturally is most conveniently defined by a Doppler limited temperature T_D. Without going into the derivation, a physical intuition for this limit can be given as it results for both the random Brownian motion induced by spontaneous emission, as well as the variation in times atoms actually remain in the excited state [25, 99]. The result is a description of the minimum temperature achievable via Molasses cooling to be described as $k_B T_D = \hbar\Gamma/2$, which for ^{87}Rb is $T_D = 146\,\mu$K. It is worth clarifying that Eq. 2.8 is truly a description of the effects of an average force, and so in turn describe the effects of an average velocity. The Doppler limiting temperature then provides a way to describe the rms velocity of our atoms which, even when their average velocity is zero, undergo Brownian motion which allows a slow diffusion out of the molasses region. In order to trap atoms, we require a position-dependent trapping force.

2.2.3 The magneto-optical trap

The optical molasses technique can generate an accumulation of slow moving atoms within the volume of the overlapped beams, where cooled atoms have a transit time that can be on the order of several to tens of seconds for beams of radius of around a centimeter. What it does not provide is a trapping force with which to contain the atoms, or in other words the system so far lacks a positional dependent restoring force. However, we can achieve this with the proper choice of polarization and the addition of a linear magnetic field gradient, where the basic principle is shown in Fig. 2.3, and we commonly refer to as the magneto-optical trap (MOT). Critically, as we will see later, the applied magnetic field itself is not alone sufficient to trap alkali species as it does not provide enough force against gravity, however it is enough to lift the degeneracies of some of the magnetic sublevels as discussed in Sec. 2.1.1.

To begin the discussion of a MOT, consider a simple system in 1D where we have the atomic transition scheme $J_F = 0 \rightarrow J_e = 1$ being addressed by a red-detuned beam. In the presence of the linear magnetic field with a direction aligned to the beams as in Fig. 2.3, as one moves away from

[5]This fast and loose switching between velocity and temperature, especially for a system which does not have a strictly defined thermodynamic temperature should be worrisome. A good discussion of how we get around (or ignore) this issue can be found in [96, Chp. 5] and [25]

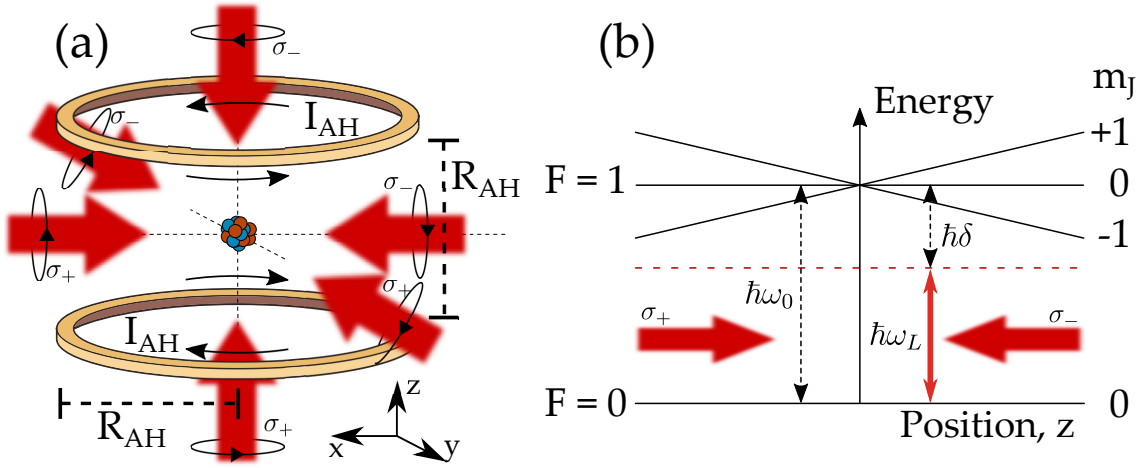

Fig. 2.3 The Magneto-Optical Trap (MOT) schematic, which makes use of six counterpropagating beams paired with a quadrupole field to both cool and trap atoms. (a) The basic layout of the trap, where the beam polarization on each axis depends on the relative field direction. Atoms coalesce in the center of the trap in a tight cloud several millimeters in diameter.(b) A combination of the Doppler shift and Zeeman-shifted energy levels cause atoms to preferentially scatter from either polarization of the light, experiencing both a dispersive cooling force and a restoring force pushing atoms to the trap center.

the geometric center the three sublevels ($m_J = 0, \pm 1$) of the excited state $J_e = 1$ split linearly and proportionally to the local field magnitude, in the limit of low fields. Taking specifically the case along the z-axis, for positive distances the Zeeman splitting puts the $\Delta m = -1$ transition closer to resonance, and the $\Delta M = +1$ further from resonance with the laser. By proper choice of laser polarization, $\Delta M_J = \pm 1$ transitions can be driven. Some care much be taken in the convention used here, as atoms follow the local direction of the magnetic field, the relative orientation of the atoms quantization axis against the electric field vector of the incoming light will change. In Fig. 2.3 we adopt the convention that light which drives the $\Delta M_J = +1$ ($\Delta M_J = -1$) transition will be denoted σ^+ (σ^-). Atoms will see both polarizations of light, however they will favor absorption from light which drives transitions closer to resonance, in the positive displacement regime this means light of circular σ^- polarization, and the reverse is true for negative distances. In either case the atoms experience an imbalanced scattering force which pushes them back towards the center of the trap.

We can formulate this model mathematically beginning with Eq. 2.8. We write the total force $\vec{F} = \vec{F}_+ + \vec{F}_-$ experienced by atoms in the MOT as follows,

$$\vec{F}_{MOT} = \frac{\hbar\vec{k}\Gamma}{2}\left[\frac{I/I_{sat}}{1+4\delta_+^2/\Gamma^2+I/I_{sat}} - \frac{I/I_{sat}}{1+4\delta_-^2/\Gamma^2+I/I_{sat}}\right], \tag{2.9}$$

where we have now defined $\delta_\pm = \omega \mp \vec{k}\cdot\vec{v} - (\omega_0 \pm \mu' B/\hbar)$, which now includes the Zeeman shifted frequency term and we strictly define the magnetic sublevel separation $\mu' = (g_e M_e - g_g M_g)\mu_B$ but in general for our situation this difference between the hyperfine structures is unity, so $\mu' \simeq \mu_B$. When we have the case where both the Doppler and the Zeeman shifted frequencies are small compared to the detuning $\omega - \omega_0$, the above equation can be expanded and then written as, dropping the vector notation for simplification,

$$F_{MOT} \simeq \frac{8\hbar k}{\Gamma} \frac{I/I_{sat}}{(1+4\delta^2/\Gamma^2+I/I_{sat})^2} \delta(kv+\mu_B B'z/\hbar) \tag{2.10}$$

Using the α as defined in Eq. 2.8 and $\beta = \alpha(\mu_B B'/\hbar k)$, when we consider only the linear region of the Zeeman shifted effect such that $B(z) \simeq B'z$, we can write this in the much more intuitive form of $F_{MOT} = -\alpha v - \beta z$. We quickly see that this new force has an effective damping term, with a damping rate given by $\Gamma_{MOT} = \alpha/m_{atom}$ and an effective 'spring constant' β where the trap oscillation frequency is given by $\omega_{MOT} = \sqrt{\beta/m_{atom}}$, which provides the restoring force.[6] Typical operating procedures in laser cooling are in the regime of an over-damped system, such that atoms are quickly slowed and then pushed towards the center by the trap without oscillation, where the time to approach the trap center can be shown to be [96, Sec. 11.4.2] on the order of $2\Gamma_{MOT}/\omega_{MOT}^2 \sim$ ms.

Experimentally, the MOT is incredibly robust and forgiving. The first experimental realizations used sodium [22], and have now been demonstrated for many alkali species and molecular combinations, albeit in more exotic MOT regimes [105, 106]. Traps can be created without precisely balancing optical powers in counterpropagating beams, nor are perfect polarizations required. Typical field gradients are on the order of $10-20\,\mathrm{Gcm}^{-1}$, which is readily achievable with externally mounted coils which can be air cooled, i.e. no cryogenics nor very high power sources are needed. The D_2 transition for alkalis is very convenient for the now prolific and reliable commercial laser diode systems, providing the cooling cycle for the Doppler cooling process.

There are some distinctions and insightful calculations that can be made to gain some clearer context and intuition as to typical MOT regimes. We can get a rough estimate of the size of a cloud by $k_B T = m v_{rms}^2 = \beta z_{rms}^2$, using the equipartition function [96], which for $T = T_D$ gives sizes on the order of several millimeters. The shifting of the atomic resonance by the MOT magnetic fields is equitable to the case of a Zeeman-slower, which we only briefly touched on in Sec. 2.2.1; however the field profile for Zeeman-slowers spatially vary as $(1-z)^{1/2}$ such that the shift exactly matches the Doppler shift as the atoms slow, which is clearly different from the linear gradients of the MOT. Nevertheless we can use $L_{min} = v_{rms}^2/2a_{max}$ from Sec. 2.2.1: for the case of ^{87}Rb in the path of a laser of $\lambda = 780\,\mathrm{nm}$, such that it addresses the D_2 line, where the beam diameter is on the order of $L_{min} = 50\,\mathrm{mm}$, giving an approximation to the maximum capturable velocity as $v_c \approx 100\,\mathrm{ms}^{-1}$. Even as an estimate, it is still significantly higher than the capture velocity for the molasses method, which for ^{87}Rb is $v_{Molasses} \simeq 4.7\,\mathrm{ms}^{-1}$ [99, Sec. 9.3]. This v_c for rubidium-87 is significantly lower than the most probably velocity of a typical oven-source atomic vapor of around 700 K, which is roughly $500\,\mathrm{ms}^{-1}$; however, we are still left with more than enough atoms from this tail end of the Boltzmann distribution describing the temperature to capture and cool atoms, when we are loading from a heated vapor source. The expected Doppler temperature for our specific optical transition is $T_D = 146\,\mu\mathrm{K}$, which we will show in the next section is often surpassed. A final speculative note is made for the MOT; real atoms are unlikely to have the pure closed transition required for the molasses cooling technique, meaning atoms quickly escape into so-called dark states which are not addressed. Generally convenient transitions are selected which have repumping transitions

[6] Any simple damped harmonic system can be written in the form $F = -av - kx$, where k is the spring constant and a is from the damping force.

where atoms are redistributed, via additional lasers, back to the main D_2 cycling transition. We will discuss this more in the next chapter.

2.2.4 Sub-Doppler Sisyphus

One of the most surprising findings of the very first MOTs and optical molasses came from measurements of the temperature of the atom clouds, which was found to be significantly lower than the Doppler-limited temperature predicted [23, 24, 107]. This of course required further investigation and over the several decades since many so-called sub-Doppler cooling mechanism have been discussed for various experimental configurations. Experimenters typically discuss mechanisms in which atoms experience a spatially varying potential which induces a state-specific shift, including effects such as *Sisyphus cooling*. The thermodynamic 'rule of thumb' is that any such mechanism which is both dissipative and irreversible can be arranged to overall cool the atomic ensemble.

In our optical system atoms experience a $\sigma^+ - \sigma^-$ polarization gradient as they move along the main axis of two counterpropagating beams. In this configuration the magnitude of the electric field is constant however its direction rotates exactly 2π every λ wavelengths radially about the axis, and is precisely linear in polarization everywhere along this axis. Unlike in linear polarization gradients (i.e. two counterpropagating linear opposite polarization beams), we *do not* have the traditionally defined valleys and hills of electric field shift used to describe moving atoms [96, 108]. What instead occurs is a preferential redistribution among the magnetic sublevels of the *ground state* as a result of the differing scattering strengths of moving atoms as per the sublevel Clebsch-Gordon coefficients. That is to say, atoms moving against the σ^+ (σ^-) beam are loaded into the $M_g = +1$ ($M_g = -1$) sublevel, and due to the increased scattering strength in this level for σ^+ (σ^-) beams, atoms experience a significant scattering force against their motion direction. This is distinct from the Doppler effect as it is described by motion-induced sublevel population difference, which results in an imbalanced scattering, or radiation, force and is not due to an imbalance of Doppler shifts between the two beams [96, 108]. While this regime is quite different from the linear-linear polarization descriptions found elsewhere [96, 99], the final equilibrium temperatures falls into the same order of magnitude for both types. For our needs it is worth noting that the scaling of this temperature goes as $T_{eq} \propto 1/\delta$, for large detuning magnitudes $\delta \geq 3\Gamma$ [108].

Grey molasses cooling As an enhancement to the cooling of atoms apart from sub-Doppler effects, grey molasses (GM) cooling makes use of a combination of Sisyphus-like cooling effects paired with velocity-selective coherent population trapping (VSCPT) [109–111]. The GM configuration makes use of light which is blue-detuned away from the $F \rightarrow F' = F$ or ($F \rightarrow F' = F - 1$) transition, and so results in atoms being coupled into *almost* dark states of the ground level manifold in which interactions with the light tend to a minimum depending, critically, on the atomic velocity class. The spatial modulation of states [110, 112] is particularly sensitive to the motion of atoms. Slow atoms remain within the dark state with their polarization adiabatically following the polarization of light, while faster atoms are shuttled back into bright states by diabatic transitions, which are more likely to occur for blue-detuned light, only to then spontaneously emit [113]. On average atoms lose kinetic energy and gradually accumulate into the dark states [112]. Rigorously

speaking, this states are not truly dark as there is some probability for slow atoms to undergo a transition back to the bright state and so the gray molasses name-sake was gradually accepted.

The experimental landscape involving so-called gray molasses, or gray MOT, cooling needs some clarification before we go on to discuss our own realization. For many alkali species it is less experimentally troublesome to use the D_1 line for GM cooling, as the corresponding D_2 transition is difficult to isolate closed transitions from open ones [112, 113]. Nevertheless, it has been shown in Ref [114] that not only can GM cooling be used on the D_2 line of potassium, but also in the regime of red-detuning from the $F \rightarrow F' = F + 1$ transition, however this specifically required a Raman transition to generate sufficient dark states for the otherwise blurry hyperfine levels of K's D_2 transitions. In our case, as we will see in Chapter 3, we induce rough gray-molasses cooling by far red-detuning from the $F' = F + 1$ state such that it is considered far blue-detuned from the lower $F' = F$ state, thus somewhat meeting the conditions of similar work in rubidium [113].

Temperature limit As a final point of note for the sub-Doppler cooling effects, and before moving on to magnetic trapping, it is worth reflecting on the various temperature scales and limits we are considering when we are cooling out atomic system. Alluded to several times, first we consider the kinetic energy of atoms of mass m within a gas of average temperature T which directly from the equipartition function we know then can be equitable to an root mean square (rms) velocity such that, $v_{rms} = \sqrt{3k_BT/m}$. For ^{87}Rb this gives $v_{rms,Rb} \approx 17\,\mathrm{ms}^{-1}\mathrm{K}^{-1/2}$, which for the case of a hot ($\sim 450\,^\circ$C) alkali dispenser gives $v \approx 460\,\mathrm{ms}^{-1}$. The significant range of Eq. 2.6 allows for an estimate of the capturable velocity of in the molasses technique, $v_c \approx \Gamma/k$, or in terms of temperature $k_BT_c = m\Gamma^2/k^2$. The Doppler limited temperature, $k_BT_D = \hbar\Gamma/2$, which for ^{87}Rb is 146 µK, is naturally next. This is then allows a calculation for the most probable velocity at such a temperature, $v_D \approx \sqrt{\hbar\Gamma/m}$. Finally, we come to the limit of the sub-Doppler techniques as considered above, the so called recoil limit or equivalently the one-photon recoil energy. As the name suggests, it is the energy associated with the recoil of the atom when emitting a resonant photon, or in other words the kinetic energy of the atom in the emission process which has an exact recoil velocity of $v_r = \hbar k/m$. This can then be considered as a recoil-temperature limit, such that $k_BT_r = \hbar^2k^2/m$; for ^{87}Rb irradiated with $\lambda = 780\,\mathrm{nm}$, T_r is 0.36 µK. The above temperatures can be then related, such that $T_r = 4\varepsilon T_D = 4\varepsilon^2 T_c$ where $\varepsilon = \hbar k^2/2\Gamma m$, which for our case $\varepsilon \approx 6^{-4}$ [96, 99].

2.3 Magnetic trapping

The origins of manipulating atoms with magnetic fields can be traced back to the famous Stern-Gerlach experiment [3, 115]. While we have already dealt with the manipulation of atoms with magnetic fields in the discussion of the MOT, the *trapping* of atoms with just magnetic fields was simply not possible as the fields used were simply not strong enough. We begin by considering an atom with a magnetic moment $\vec{\mu}$ interacting with a magnetic field of strength $\mathbf{B}$, with a force described by $\mathbf{F} = \vec{\nabla}(\vec{\mu} \cdot \mathbf{B})$. This of course then can be described by a potential of the form $V = -\vec{\mu} \cdot \mathbf{B}$, as we have already encountered in Sec. 2.1.1.

In order to generate a magnetic potential which traps atoms for long periods of time, limited by other experimental effects, there are a few subtilties to consider. For an atom in a particular state, say where $g_FM_F > 0$ for example, the energy above becomes $V = g_FM_F\mu_B|\mathbf{B}|$ and critically

the energy depends only on the local magnetic field magnitude. The force experienced for this specific state pushes atoms towards low-field regions, and as such we denote $g_F M_F > 0$ states as low-field-seeking, and similarly the reverse is true for states where $g_F M_F < 0$, which are pushed towards high-field regions. Overarching in all of this is the implicit assumption that the magnetic dipole of the atoms follows the local field direction adiabatically. Specifically the Larmor frequency $\omega_L = g_F M_F \mu_B B/\hbar$ must be much greater than the timescales ($tvs1/\omega_L$) under which atoms move around the trap; in a case where stable atoms are trapped in orbits around the trap center, the latter timescale can be roughly considered as $\omega_T = v/\rho$ where ρ is the radius and v the linear orbital velocity. This leads to a potential loss mechanics for atoms which are trapped within a magnetic landscape, as at low fields where the effective orbits are very small, the adiabatic condition is no longer met. These Majorana losses see the M_F states mix as fluctuations, or even just degeneracy at the exact center of the trap occur, shuffling atoms into and out of high-field-seeking states. The loss effect is often described as a hole within a funnel which atoms pass through. The calculation of magnetic potentials generated by the flow of current, followed by common magnetic trap designs and the 'plugging' of the magnetic hole will make up the majority of the remainder of this chapter.

2.4 Magnetic Field Calculations

The general form for the induced magnetic field $\mathbf{B}(\mathbf{r})$ at a point $P(\mathbf{r})$, see Fig. 2.4a, generated by a steady infinitesimal current density $\mathbf{j}(\mathbf{r}')$ flowing through a conductor is given by the Biot-Savart law [116],

$$\mathbf{B}(\mathbf{r}) = \frac{\mu_0}{4\pi}\int_V \mathbf{j}(\mathbf{r}')\times\frac{\mathbf{r}-\mathbf{r}'}{|\mathbf{r}-\mathbf{r}'|^3}\mathrm{d}V'. \tag{2.11}$$

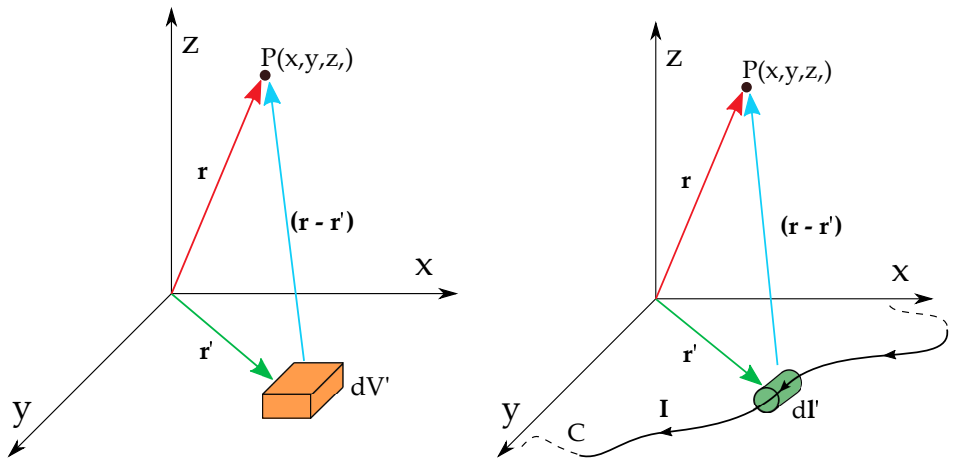

(a) Biot-Savart construction for the induced field at a point P(x,y,z) from a current density element $\mathrm{d}V'$.

(b) Biot-Savart construction for the induced current from a current element, $\mathbf{dl}'$, as part of a strictly continuous circuit, C, carrying a current I.

Fig. 2.4 Simple coordinate defintions for elementary components for use in Biot-Savart calculations.

For our purposes we will generally be concerned with line elements of current integrated over a current loop or circuit, such that $\mathbf{j}(\mathbf{r}')$ becomes $Id\mathbf{l}'$, where $d\mathbf{l}'$ is pointing in the direction of current flow, and I the current, see Fig. 2.4b. The result is an integral now defined over the circuit C,

$$\mathbf{B}(\mathbf{r}) = \frac{I\mu_0}{4\pi}\int_C \mathrm{d}\mathbf{l}' \times \frac{\mathbf{r}-\mathbf{r}'}{|\mathbf{r}-\mathbf{r}'|^3}\,. \tag{2.12}$$

Before moving on, we note that we strictly consider Eq. 2.12 as only defined along a continuous circuit. You will find yourself in a violation of Maxwells equations if there were regions where current suddenly appeared and disappeared. Further caution must also be taken when one attempts to derive the expressions above using a superposition of individual moving charges, as you would naturally then leave the bounds of magnetostatics. In the former case one considers, as we will below, finite segments of current as simply segments of some other circuit [117, Chapter 2], and in the latter case a full relativistic [116, Chapter 5] consideration is required to derive the same results.

In the following sections we demonstrate several known calculations of the magnetic field generated by simple structures. Three examples are shown, all in the infinitesimally thin conductor regime: a finite wire, an infinitely long wire, which is just a limit of the finite case, and finally a circular loop. In later sections we will use these to calculate common trapping structures, going on to show how we can then calculate trapping frequencies and depths.

2.4.1 Finite and Infinite Wires

We first consider the case of a wire of length, L, carrying a steady current, I, which induces a magnetic field $\mathbf{B}(\mathbf{r})$ at some point $P(x,y,z)$, as shown in Fig. 2.5a. Defining the vector from the current element to the point P as $\mathbf{r_l} = \mathbf{r} - \mathbf{r}'$, we rewrite Eq. 2.12 as,

$$\mathbf{B}(\mathbf{r}) = \frac{I\mu_0}{4\pi}\int_C \frac{\mathrm{d}\mathbf{l}' \times \hat{\mathbf{r}}_\mathbf{l}}{|\mathbf{r_l}|^2}\,. \tag{2.13}$$

We then solve this system between the limits of θ_1 and θ_2, where R is the magnitude of the distance between the center of the wire and the point being evaluated, giving,

$$\mathbf{B}(\mathbf{r}) = \frac{I\mu_0}{4\pi R}(\sin\theta_2 + \sin\theta_1)\hat{\mathbf{n}}\,, \tag{2.14}$$

where the direction of the unit vector $\hat{\mathbf{n}}$ is found from the right-hand rule, i.e. from the cross product $\mathrm{d}\mathbf{l}' \times \hat{\mathbf{r}}_\mathbf{l}$. We can quickly derive the case of an infinite wire from Eq. 2.14 as the limiting case where $\theta_1, \theta_2 \to \pi/2$, resulting in

$$\mathbf{B}(\mathbf{r}) = \frac{I\mu_0}{2\pi R}\hat{\mathbf{n}}\,. \tag{2.15}$$

Here we have not made any assumptions regarding the direction of the current carrying wire, but assume a cylindrical coordinate system defined along the axial direction of the wire and whose directions are determined by the standard right hand rule. In principle any arbitrary wire can be converted to a more convenient basis through a standard coordinate transform, from cylindrical to cartesian, and then coordinate rotation and translation to the desired cartesian unit basis.

2.4.2 Circular Loops

The magnetic field induced from a infinitesimally thin circular loop has a known analytical solution, whose exact general form can be readily found from textbook sources [116, section 5.5]. In brief,

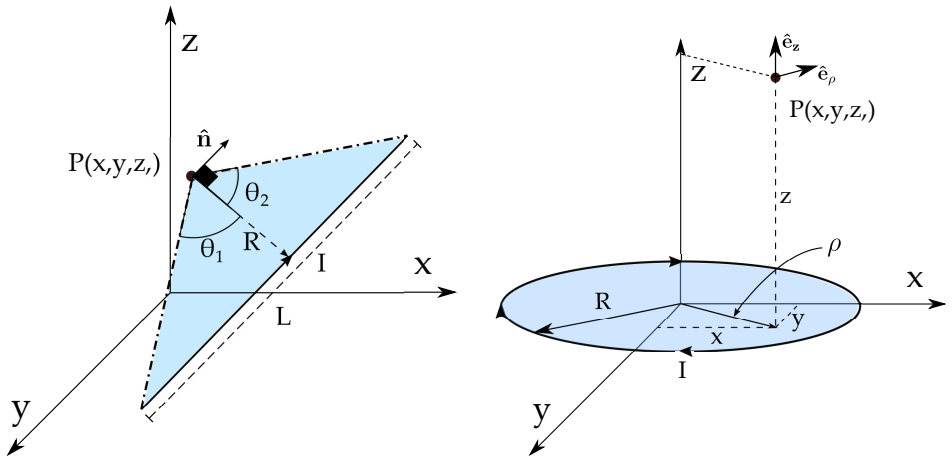

(a) Biot-Savart construction for the induced field at a point P(x,y,z) from a current density element dV'.

(b) Biot-Savart construction for the induced current from a current element, $d\mathbf{l}'$, as part of a strictly continuous circuit, C, carrying a current I.

Fig. 2.5 Simple coordinate defintions for elementary wire and loop components for use in Biot-Savart calculations.

the result is calculated from the integration of the vector potential, **A** across the current elements. The magnetic field found by applying $\nabla \times \mathbf{A} = \mathbf{B}$ [118, 119] using whichever geometric choice of coordinate system is convenient. Below, for reference, I give the magnetic field solutions for a single loop of radius R perpendicular to the z axis, centered at $z = 0$,

$$\mathbf{B_z} = \frac{\mu_0 I}{2\pi} \frac{1}{[(R+\rho)^2+z^2]^{1/2}} \left\{ K(k^2) + E(k^2) \frac{R^2-\rho^2-z^2}{(R-\rho)^2+z^2} \right\} \hat{\mathbf{e}}_\mathbf{z}\,, \tag{2.16}$$

$$\mathbf{B}_\rho = \frac{\mu_0 I}{2\pi\rho} \frac{z}{[(R+\rho)^2+z^2]^{1/2}} \left\{ -K(k^2) + E(k^2) \frac{R^2+\rho^2+z^2}{(R-\rho)^2+z^2} \right\} \hat{\mathbf{e}}_\rho\,, \tag{2.17}$$

where K and E are the complete elliptical integrals of the first and second kind, respectively, whose argument is determined by,

$$k^2 = \frac{4R\rho}{(R+\rho)^2+z^2}\,. \tag{2.18}$$

For further reference on elliptic integrals please see [120, 121], otherwise the reader may taken these as known mathematical outputs which are readily calculable by common numerical software.

2.4.3 Simple Systems

As a cloud of atoms is trapped and cooled from a thermal gas of many hundreds of kelvin to a Bose-Einstein condensate of nanokelvin, its average temperature spans roughly ten orders of magnitude; whilst its spatial extent can range from several millimeters to tens of micrometers. To account for this range, typical experiments implement several stages of trapping starting with the magneto optical trap[7] then often moving into purely magnetic traps. These regimes are realized by different structures whose inputs, electrical current being the most relevant for the generation of

[7] I am, of course, ignoring optical-trapping experiments.

static fields, are chosen to be tunable enough such that the generated trap magnetic potentials can be mode-matched to ensure the efficient transfer of atoms between regimes.

In this section I will explore some of these trapping architectures and compare them for various common experimental properties. First, however, I will consider how we can calculate such properties in the case of an ideal two-dimensional quadrupole magnetic trap with a non-zero offset, to provide a zero-order benchmark for comparison.

Our two-dimensional quadrupole only generates magnetic field gradients in its plane, whilst the non-zero offset provides an effective plug to avoid zero-field losses in the trap center. Defining the quadrupole in the x-y plane we can infer [99], from Maxwell's relation $\nabla \cdot \mathbf{B} = 0$, the gradients along each axial direction are $\partial_x \mathbf{B}_x = -\partial_y \mathbf{B}_y = b'$, where we have defined b' as the magnitude of the gradient along the x and y axis. The total form of the magnetic field, including the constant field along the z-direction, $\mathbf{B}_z = B_0 \hat{\mathbf{e}}_\mathbf{z}$, is,

$$\mathbf{B} = b'(x\hat{\mathbf{e}}_\mathbf{x} - y\hat{\mathbf{e}}_\mathbf{y}) + B_0\hat{\mathbf{e}}_\mathbf{z}\,. \tag{2.19}$$

The most commonly quoted property of a magnetic trap is its trapping frequency, $\omega_{x,y,z} = 2\pi f_{x,y,z}$. A high frequency typically implies a high collision rate[8] between atoms, as it has a direct correspondence to the spatial extend of the atomic cloud. For traps considered in this work, we can make a harmonic approximation within the trapping region and so equate the energy potential experienced by the atom to that of a harmonic oscillator,

$$V = \mu \cdot \mathbf{B} = g_F \mu_B m_F \,|\mathbf{B}| \approx \frac{1}{2} M\omega^2 r^2\,, \tag{2.20}$$

where M is the mass of the atomic species, ω the angular frequency, and $r = \sqrt{x^2+y^2}$. We have also implicitly chosen an atom in the Zeeman sub-level $|IJFM_F\rangle$. Note that we define the frequency at the center of the quadrupole field, where $(x,y,z) = 0$. In order to marry the energy description of the field from Eq. 2.20 and Eq. 2.19, we take the second spatial derivatives of both evaluated at the center, i.e. $\partial^2|\mathbf{B}|(r, z=0)$, and then rearrange for ω giving,

$$\omega = \sqrt{\frac{\mu_B M_F g_F}{M}}\frac{b'}{\sqrt{|B_0|}}\,. \tag{2.21}$$

For the case of ^{87}Rb in a state such that $m_F g_F = 1$ ($m_F = 2$,$g_F = 1/2$), and in units of Gauss and mm, we can collapse Eq. 2.21 to give,

$$\frac{\omega_i}{2\pi} = f_i = 12.7\frac{b'}{\sqrt{|B_0|}}\ \text{Hz}. \tag{2.22}$$

The above equation gives us an intuitive picture of how the trap frequency scales with respect to the two-dimensional gradient, b' and the field offset B_0. Note that as we consider the z-field as a constant offset, its frequency and gradient are naturally zero in this model. Physically this would mean atoms would eventually escape from the trap along this axis and so our model is only practical as a qualitative benchmark.

[8] See [Section Ref] for the discussion of this

In systems where the simple pure quadrupole approximation is no longer appropriate, we instead consider the full magnetic field potential and, in the cases where there is a minimum in the origin of the trap geometry, calculate the field curvature $\partial^2\mathbf{B}(r(x,y,z)=0)$. From Eq. 2.20 one can then show the following,

$$\frac{\omega_i}{2\pi} = f_i = \frac{1}{2\pi}\sqrt{\frac{\mu_B M_F g_F}{M}}\sqrt{\partial^2_{ii}\left|\mathbf{B}_i(x,y,z=0)\right|}. \tag{2.23}$$

In much the same way as we have compared the magnetic energy to the harmonic potential energy, we can do the same with the average kinetic energy, i.e. temperature, T, of the cloud. Letting the spatial extent of the cloud, r in Eq. 2.20 tend to the FWHM σ, we can then write,

$$\frac{\omega_i}{2\pi} = f_i = \sqrt{\frac{k_B T}{M\sigma^2}}, \tag{2.24}$$

where k_B is the standard Boltzman constant.

In general, the frequencies described above in Eq. 2.23 can be directly calculated and read off from a diagonalized Hessian matrix whose elements are the mixed partial derivatives of the (scalar) magnetic field magnitude whose general form is given by,

$$\mathbf{H} = \begin{pmatrix} \partial^2_{xx}|\mathbf{B}| & \partial^2_{xy}|\mathbf{B}| & \partial^2_{xz}|\mathbf{B}| \\ \partial^2_{yx}|\mathbf{B}| & \partial^2_{yy}|\mathbf{B}| & \partial^2_{yz}|\mathbf{B}| \\ \partial^2_{zx}|\mathbf{B}| & \partial^2_{zy}|\mathbf{B}| & \partial^2_{zz}|\mathbf{B}| \end{pmatrix} \tag{2.25}$$

For cases where the cartesian axis of the lab are equal to the eigenaxis of the Hessian, $\mathbf{H}$, the off-diagonal elements are exactly zero and the three spatial field curvatures at the trap minimum are found from the main diagonal elements. Then, as per Eq. 2.23 the *eigenfrequencies* of the trap can be found. The power of such a formalism is allowing for complex field profiles, which may not align to the lab frame, but still generate a sufficient trapping profile for our atoms.

2.5 Towards Bose-Einstein condensation

Evaporative cooling Laser cooling is powerful tool for experimenters, cooling atoms captured by the MOT by six orders of magnitude from hundreds of kelvin to just microkelvin temperatures. However, as we have seen, the recoil limit sets a fundamental floor to this temperature. Atoms which are trapped in harmonic magnetic-only potentials, that is traps without any optical confinement, can benefit from evaporative cooling.

In the common analogy evaporative cooling is compared to blowing steam away from a hot liquid; by removing only the hottest fraction of the particles, the average ensemble temperature is lowered. Losing the analogy, atomic ensembles are cooled through a combination of two processes: the selective removal of the hottest end of the thermal distribution 'tail'; and the elastic collisions of atoms which redistributes energy, lowering the average ensemble temperature in a process known as rethermalization [27]. In the right conditions *runaway evaporation* can occur, where the loss of atoms is overcompensated by a reducing in the volume, increasing the phase space density. This can only occur for harmonic traps, where cooler atoms sink down the potential.

The practical implementation is through the application of RF radiation, often called an RF-knife, which drives transitions between the $\Delta M_F = \pm 1$ states. The RF field is spatially selective, only occurring where the condition $g_F \mu_B b' r = \hbar \omega_{RF}$ is met, where b' is the field gradient at the radius r away from the trap center [99, Sec. 10.3]. As the trap is harmonic only hot atoms which can oscillate up to and past this radius will escape, and then by sweeping the RF frequency down the average ensemble temperature is lowered. There are complications to the process. One may assume that a narrow high RF frequency would be preferable as only the very hottest atoms would be removed, albeit slowly, however collisional losses from background atoms *and* the production of alkali-molecules through three-body collisions set a time scale to the how slow one can carry out the process. Calculating the threshold to achieve optimal cooling is well presented in Ref. [122, Sec. 4.6] and Ref. [27], however one key result is that *linear* potentials are significantly better than harmonic ones. We will see later when the Ioffe-Pritchard trap is introduced that atoms can experience such a linear quadrupole field along its radial direction, which is important for the first stages of evaporative cooling [99, Sec. 10.3].

Bose-Einstein condensation Bosons, as integer spin particles, may occupy the same state. For the case of dilute vapors of alkali metals in a magnetic trap, the correct application evaporative cooling allows the ensemble to reach a critical phase-space density. At this point a phase-space transition occurs and atoms cascade into the ground state [99, Sec. 10.4], and the deBroglie wavelengths of the individual atoms become equitable to the interparticle spacing. One can calculate the transition temperature, T_C at which this transition occurs for the case of a harmonic trap of frequency $\bar{\omega}$ to be $k_B T_C = C_1 \hbar \omega N^{1/3}$, where N is the number of particles, $\bar{\omega} = (\omega_x \omega_y \omega_z)^{1/3}$ is the geometrical mean of the trap frequency and C_1 is a numerical factor which is approximately $C_1 \approx 0.94$ [122, Sec. 1.1]. For our purposes, we note that by increasing the average trap frequency and the number of atoms increases the critical temperature, and so in rough terms makes the transition more accessible.

2.6 Magnetic Trapping Structures

So far we have discussed the fundamentals of how atoms interact with fields, and how we can calculate the characteristics of trapped atom ensembles from the magnetic potential landscapes. Here we will now discuss the realization of such magnetic potentials. Broadly speaking, the various magnetic fields used in our experiments are generated by passing electrical currents through different architectures, as mathematically formulated by the Biot-Savart equation. Many idealized systems, some of which will be considered below, neglect to take into account the final applications and experimental constraints; nevertheless, they provide useful benchmarks to compared against experimental realizations. We will first consider these, and then eventually consider more experimentally oriented designs.

In a simplified description we can somewhat crudely separate the choices of current carrying geometries into, often complementary, camps: three dimensional (3D) geometries, such as Helmholtz coils or Ioffe-Pritchard traps; and two dimensional (2D) geometries, e.g. printed circuit boards (PCBs), atom chips, and atom chip understructures. Of course 2D structures must have three dimensions in practice, but until the case where the atoms size and distance from the structure

approaches the dimensions of the structures themselves, we can generally consider them as truely two-dimensional. The magnetic fields generated by each architecture vary significantly enough that they are often chosen and form a sequence of overlapping trapping potentials which manipulate atoms in each bespoke stage of the experimental method.

2.6.1 2D vs 3D Structures

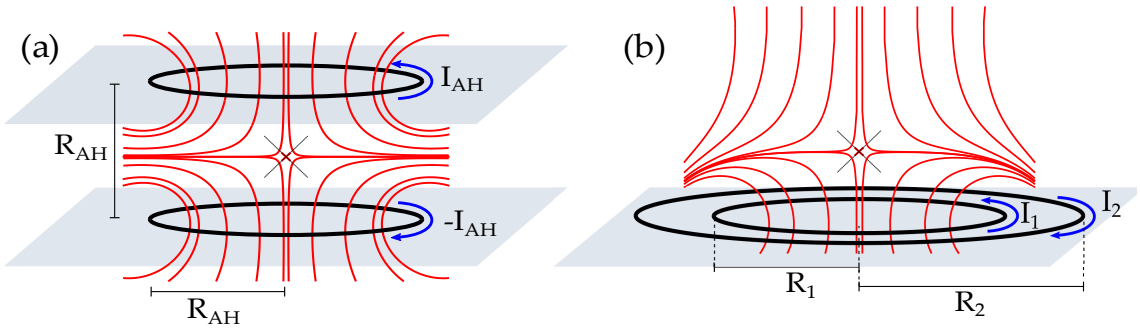

Fig. 2.6 Comparison of two quadrupole field generating structures whereby two current loops are placed in two parallel planes (3D) or a single plane (2D). Streamline plots show the field produced from the 3D system (a) and 2D system (b).

The power consumed in generating magnetic fields is often a low-priority when laboratory-based experiments are designed. In contrast the reduction of the overall power is a primary driving force for any system which hopes to be portable, and so also a major consideration of this work. To this aim, we begin our discussion of magnetic field generating structures below by demonstrating a toybox calculation comparing the 3D and 2D architectures, specifically investigating the potential for power reduction when compared like-for-like. Even in this toybox model we do not strictly have true three-dimensional shapes, but more accurately infinitesimally thin structures either sharing the same plane or distributed across two parallel planes.

In the 3D scenario we choose two infinitesimally thin current loops in the anti-Helmholtz configuration; where two parallel loops with equal radius R_{AH} carrying equal currents I_{AH} are placed at a distance $d = R_{AH}$ from each other, Fig. 2.6(a). This is compared to two in-plane concentric current loops, defining the 2D scenario, as shown in Fig. 2.6(b). The in-plane loops have radii R_1 and R_2 and carry currents I_1 and I_2, respectively.

The anti-Helmholtz configuration has a field zero as a consequence of the equal and opposite currents, which from the system symmetry we see naturally occurs at the geometric center along the axial line connecting the two loops. Explicitly, at a distance $R/2$ from either loop. To generate a reasonable comparison with the 2D case, we fix the 3D system geometric parameters and current, and define a set of boundary conditions to allow us to determine the currents and radii required to generate a similar, with respect to its geometric characteristics, quadrupole field in the 2D planar scenario.

Consequently, we impose the following conditions: A) that the position of the field zero forms at $R_{AH}/2$ along the center line perpendicular to the plane; B) that each system has equal power consumption, i.e. $R_1 I_1^2 + R_2 I_2^2 = 2 R_{AH} I_{AH}^2$; C) we require the field curvature to vanish at the field zero, so that in approximation of the ideal quadrupole field the field varies only linearly at the

center; D) finally we calculate for a maximal field gradient magnitude at the field minimum. Note that without loss of generality it is sufficient to only consider the field along the loops' symmetry axis z, where the field is always oriented along z. We demonstrate the conditions mathematically below.

$$\text{Condition A)} \quad \mathbf{B_{z,2D}}(z=1/2) = \mathbf{B_{z,3D}}(z=1/2) = 0, \tag{2.26}$$

$$\text{Condition B)} \quad R_1 I_1^2 + R_2 I_2^2 = 2RI^2, \tag{2.27}$$

$$\text{Condition C)} \quad \partial_z^2 \mathbf{B_{z,2D}}(z=1/2) = 0, \tag{2.28}$$

$$\text{Condition D)} \quad \partial_{R_1} |\partial_z \mathbf{B_{z,2D}}(z=1/2)| = 0, \tag{2.29}$$

where we enforce the maximum gradient magnitude condition, D), by finding the zero-crossing of the function when differentiated with respect to the remaining free variable over a natural variable range. In this case we have chosen this to be the radii R_1, which is only real for values greater than $R_1/R > 1$.

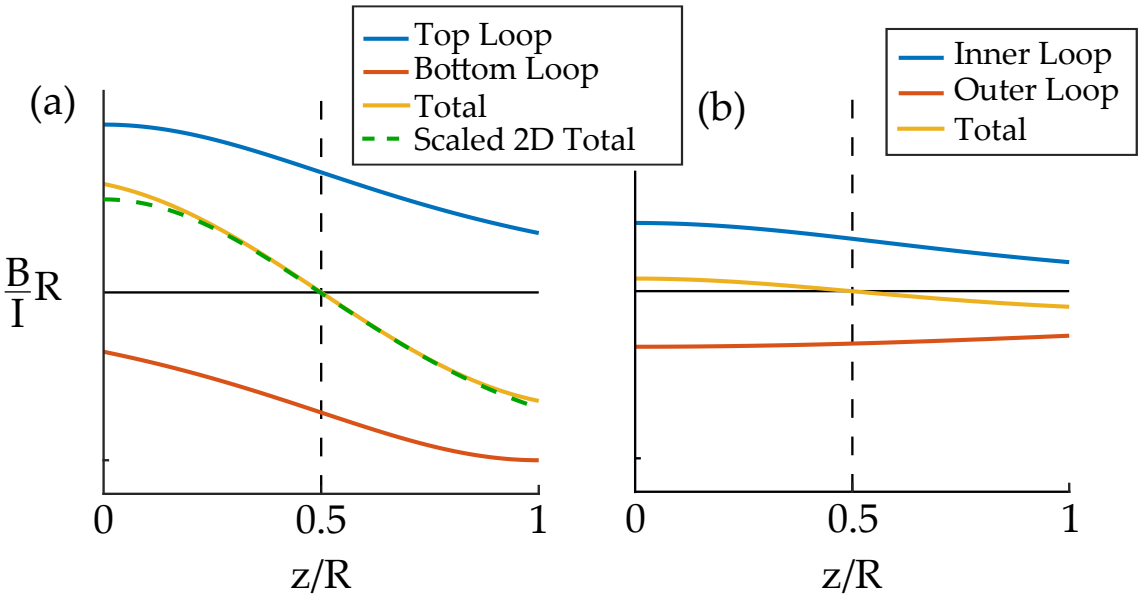

Fig. 2.7 (a) Magnetic field strength along the symmetry axis z of the 3D current loops (due to symmetry radial fields vanish). The magnetic field of one loop (blue) is compensated exactly by the other (red) in both configurations at the same zero-field position, $R_{AH}/2$. At equal power consumption, the magnitude of the total field gradient (yellow) for the 3D system is stronger than that in the 2D case by a factor of 7.37. To reach the same gradient with the planar 2D assembly, the current needs to be scaled up by the same factor (dashed green line). This corresponds to an increased power dissipation by a factor of 54.3. (b) as in (a), the field strength along the symmetry axis for the 2D planar current loops, without the scaling.

We find that under the above constraints the maximal gradient is achieved in the planar configuration when $R_1 = 1.14\,R_{AH}$ and $R_2 = 2.51\,R_{AH}$ with the currents $I_1 = 0.46\,I_{AH}$ and $I_2 = -0.84\,I_{AH}$. Even in this optimal configuration, the resultant 2D-case gradient is reduced by a factor greater than 7 when compared to the 3D anti-Helmholtz configuration. Calculated field configurations are shown in Fig. 2.7(a) for a 3D structure and Fig. 2.7(b) for a planar structure.

2.6.2 The Ioffe-Pritchard trap

Beginning with this section, we will now discuss several common three dimensional realizations of magnetic traps, generally only considering designs which have a non-zero field minimum in their trapping volume. We will calculate the magnetic field, where possible, in the most general terms allowing for expressions of the trap frequencies as per Eq. 2.23 to be found. At the end of this section we will compare the considered structures in a test-best case, to simplify any remaining degrees of freedom. In particular considering relative power consumption, trapping frequencies and trap depth.

The Ioffe-Pritchard, or IP, trap is the most experimentally realizable architecture directly relatable to the field profile described in Eq. 2.19. Here we calculate a toybox IP trap consisting of four infinite parallel wires, separated in the x-y plane by a closest distance of s_0 on a regular quadrilateral square[9], each carrying a current of magnitude I_W, who's direction is given in Fig. 2.8. To cap the field along the z-axis, we use two loops whose symmetric axis lies along z and provides total field magnitude at the center $(x, y, z = 0)$ of the trap of B_0.

In this simple case, the field generated by one wire at position (x_0, y_0) can be readily derived from Eq. 2.14 in cartesian coordinates where $\phi = \arctan[(y-y_0)/(x-x_0)]$ giving,

$$\mathbf{B}_{x,y}(x,y) = \frac{\mu_0 I_w}{2\pi}\left\{\frac{-\sin\phi(x,y)\hat{\mathbf{e}}_\mathbf{x} + \cos\phi(x,y)\hat{\mathbf{e}}_\mathbf{y}}{[(x-x_0)^2+(y-y_0)^2]^{1/2}}\right\}. \tag{2.30}$$

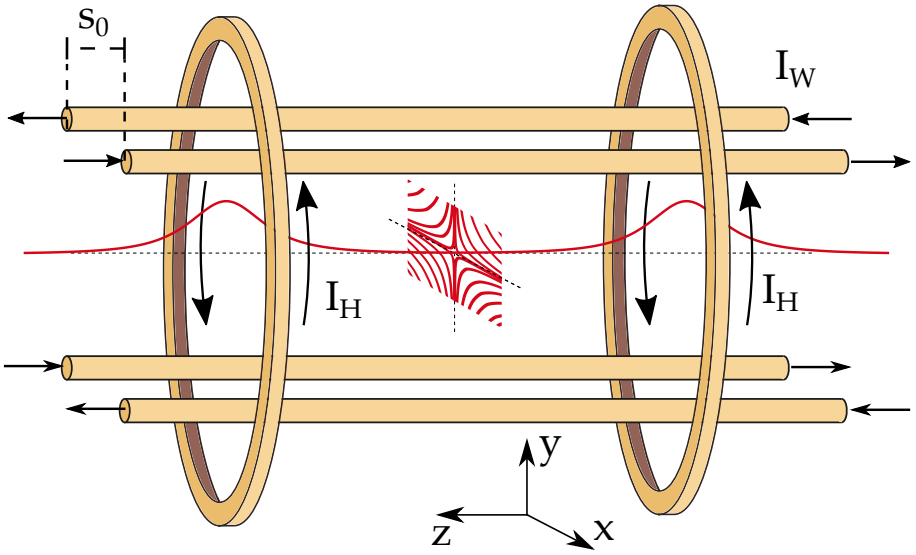

Fig. 2.8 Schematic of a typical symmetric Ioffee Pritchard magnetic trap. The axial line of the Ioffee bars sit on a square in the x-y plane with a separation of s_0, while the distance between the Helmholtz field-capping loops is determined by the desired trapping regime, as shown in Section 4.5.1. Red field profiles show the shape of the individual magnetic field magnitudes; the main axial line shows $|\mathbf{B}_z(x, y = 0, z)|$; the planar profile shows $\left|\mathbf{B}_r(r = \sqrt{x^2+y^2}, z = 0)\right|$.

The total x-y plane component of the field from all four wires can then be readily calculated from Eq. 2.30, it is not given here as it is somewhat bulky. Since the trap minimum will appear on the axial symmetry line, we need only consider the axial components generated by the capping

[9] Each wire sits on the corner of a square such that $s_0 = 2x_0 = 2y_0$.

Helmholtz coils. Thus we can write Eq. 2.17 for a single loop carrying a current of I_{AH} at an axial distance of z_0 from the trap center as,

$$\mathbf{B}_z(z) = \frac{\mu_0}{2}\frac{I_H R^2}{[(z-z_0)^2+R^2]^{3/2}}\hat{\mathbf{e}}_\mathbf{z}\,. \tag{2.31}$$

Calculation of the three cartesian trapping frequencies is somewhat straight forward using Eq. 2.23. We will also take the experimentally convenient convention where SI fields and lengths are converted as follows $[\mathrm{T},\mathrm{m}] \to [\mathrm{G},\mathrm{mm}]$. In the center of the trap we quickly see that $B_0 = 4\pi I_H R^2/(z_0^2+R^2)^{3/2}$, where z_0 is the center-to-center separation of the two Helmholtz loops. Using this form of B_0, we can then find the following,

$$f_z = 12.7\sqrt{-3K(R,z_0)B_0}\,, \tag{2.32}$$

$$f_{x,y} = 12.7\sqrt{\frac{3}{2}B_0 Q(R,z_0) + \frac{16I_W^2}{B_0 s_0^4}}\,. \tag{2.33}$$

Here we have defined the parameter $Q(R,z_0) = (R^2-4z_0^2)/(R^2+z_0^2)^2$. Real solutions of Eq. 2.32 require that $z_0 > R/2$, where $z_0 = R/2$ is the recognizable Helmholtz condition. In this regime, and in the case where we generally want at least $B_0 = 1\,\mathrm{G}$[10] to avoid losses at the trap center, the first term in Eq. 2.33 is much smaller than the second, such that we finally have,

$$f_{x,y} \simeq 12.7\frac{4I_W}{s_0^2\sqrt{B_0}}\,. \tag{2.34}$$

It is somewhat straight forward in this system to then calculate the resultant trap depths, which are as follows in terms of temperature,

$$\mathrm{Depth}_{x,y}[\mu\mathrm{K}] = \sqrt{(}2)3^{3/4}\frac{I_W}{s_0} \times (67\,\mu\mathrm{K\,G^{-1}})\,, \tag{2.35}$$

$$\mathrm{Depth}_z[\mu\mathrm{K}] = 2\pi I_H\left[\frac{R^2}{(R^2+4z_0^2)^{3/2}} - \frac{2R^2}{(R^2+z_0^2)^{3/2}} + 1/R\right] \times (67\,\mu\mathrm{K\,G^{-1}})\,. \tag{2.36}$$

In later sections we will bound some of the degrees of freedom for the expressions above, allowing for a comparison of like-for-like traps to be carried on.

2.6.3 The QUIC Trap

The *QU*adrupole *I*offee *C*onfiguration (QUIC) Trap, unlike the IP trap, has the key advantage that atoms can first be trapped in the traditional MOT configuration using anti-Helmholtz (AH) coils, as in Fig. 2.9, but then smoothly transferred to a non-zero magnetic trap by superposition with an additional third, QUIC, coil. Other than this QUIC coil, no additional trapping structures are requires, whereas the IP trap would in principle need an initial overlapping MOT coil for the initial cooling and confinement. As the current in the QUIC loop can be ramped gradually and smoothly,

[10] More rigorously, this condition is that $0 < \sqrt{(32/3)I_W^2/(s_0^4 K'(R,z_0))} \ll B_0$, where $K'(R,z_0) = -K(R,z_0)$.

there will in principle be less thermal shock on the atoms as would be the case when trapping potentials are rapidly changed. This would allow atoms to be transferred with a higher efficiency, and experimentally the arrangement overall requires fewer control parameters.

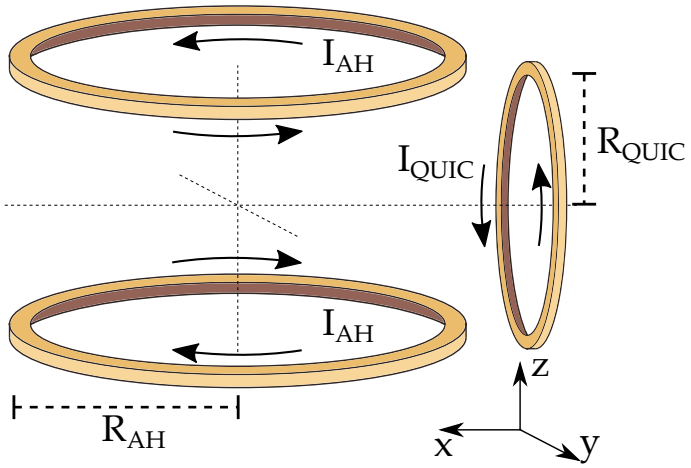

Fig. 2.9 Schematic of a typical QUIC trap. Atoms are initially confined with magnetic gradient, provided by I_{AH}, and optical fields as in the traditional MOT. By ramping I_{QUIC} from zero, a non-zero field minimum is generated whose position and offset are determined by the ratio of I_{AH}/I_{QUIC}.

Numerical calculations of the traps basic parameters are quite straightforward using Equations 2.16 and 2.17, following the same procedure as in Sec. 2.6.2. However simple analytical formulae are more difficult to derive as the QUIC trap system has a, by design, broken symmetry along the x-axis. For the IP trap the cylindrical symmetry of the system results in the trap center being exactly along the cylindrical axis, i.e the case $\rho = 0$, meaning the elliptic integrals $E(k^2)$ and $K(k^2)$ reduce to $\pi/2$ in both cases [123]. While for the QUIC trap the position of the trap center as the current, I_{QUIC}, is increased will drift away from the center of the AH loops towards the QUIC loop.

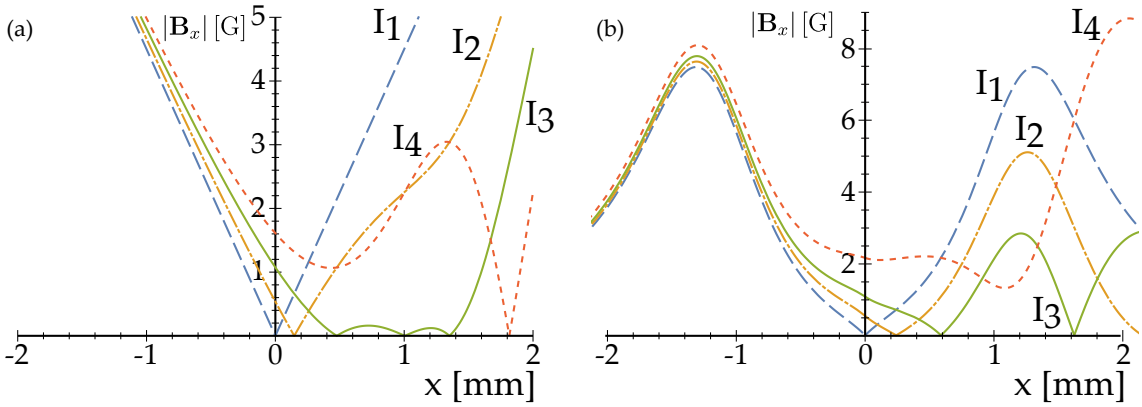

Fig. 2.10 The QUIC trap: the x components of the magnitude of the magnetic field strength along the x-axis in (a) the case of a linear field gradient as in Eq. 2.37 and (b) the full elliptical calculation as in Eq. 2.38. $I_{1,2,3,4}$ denotes the ratio I_{QUIC}/I_{AH}, where $I_i = (0, 0.5, 1, 1.5)\, I_{AH}$ respectively. In (b), $I_{AH} = 1\,\mathrm{A}$, $I_i = (0, 0.5, 1, 2)\, I_{AH}$, $R_{AH} = 1\,\mathrm{mm}$, $R_{QUIC} = R_{AH}$ and $d_{QUIC} = 1.5\, R_{QUIC}$. For (a), the term g_x is found from a calculation of the gradient at $x = 0$ in the elliptic case, (b).

In order to get an understanding of the trap formation we will instead approximate the QUIC trap system along the x-axis as defined in Fig. 2.9. Along this axis the QUIC coil generates a magnetic field in x only, and we will simplify the 3D-quadrupole generated by the AH coils as an ideal 1D-quadrupole centered at the origin. The magnetic field along this axis will be,

$$\mathbf{B}_x(x) = g_x x\hat{\mathbf{e}}_\mathbf{x} + \frac{\mu_0}{2}\frac{I_{QUIC}R_{QUIC}^2}{[(x-x_0)^2+R_{QUIC}^2]^{3/2}}\hat{\mathbf{e}}_\mathbf{x}\,, \tag{2.37}$$

where g_x is the field gradient of the ideal quadrupole and x_0 is the position of the QUIC loop along the x-axis. Compare this to the elliptical expression for the x-component of the magnetic field along the x-axis,

$$\mathbf{B}_\mathbf{x}(x) = \frac{2I_{QUIC}R_{QUIC}^2}{[R_{QUIC}^2+(x-x_0)^2]^{3/2}}\hat{\mathbf{e}}_\mathbf{x} - \frac{2I_{AH}R_{AH}[(5R_{AH}^2+x^2)E(k^2)-K(k^2)]}{\sqrt{\frac{R_{AH}^2}{4}+(R_{AH}+x)^2}}\hat{\mathbf{e}}_\mathbf{x}\,. \tag{2.38}$$

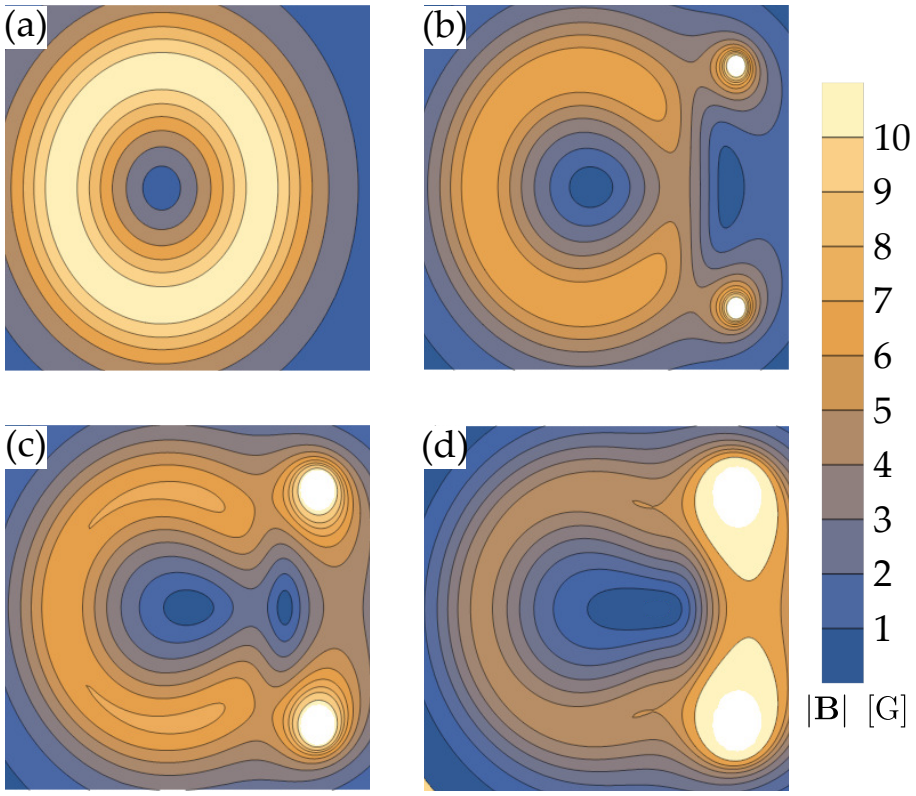

Fig. 2.11 Contours of the field magnitude in the XY plane of the QUIC trap, as the current in the QUIC coil is increased. Here $R_{QUIC} = R_{AH}$ and $d_{QUIC} = 1.5R_{QUIC}$, and $I_{QUIC}/I_{AH} = (0, 0.5, 1, 2)$ from (a-d). The ramping of the QUIC current morphs the field geometry, pulling the zero-field minimum at the origin towards a second zero-field point, seen aligned with the QUIC coil itself in (b). These merge and the minimum is raised from zero, until case (d), where the value of the field minimum is 1 G. Fields are calculated using the full elliptical form, as in Eq. 2.38.

Whilst the field in Eq. 2.37 is simpler than the elliptical expression, it is not alone suitable to calculate trap properties as there still remains a position dependence. The choice of trap position was implicit in previous calculations as the trap was always found at the origin of the system.

Further complicating the calculation is the expression in Eq. 2.37 is not uniquely solvable. Multiple minima can be found whose position and appearance are dependent on the geometric and current choices made, which for the QUIC coil architecture leaves three degrees of freedom, if we assume the anti-Helmholtz coils are fixed.

Fig. 2.10 shows how the two systems evolve for a generic choice of variable when I_{QUIC} is varied. In both cases one sees the movement of the trap position, initially at the origin, towards the QUIC loop as the current I_{QUIC} increases. Further zero-field minima occur as the current rises until a critical point where the original trap position minima merges with another,, causing the field offset to rise. In the linear potential case of Fig. 2.10(a), an offset $B_0 = 1\,\mathrm{G}$ is achieved for $I_{QUIC}/I_{AH} = 1.5$, whilst the more realistic ellpitical case requires $I_{QUIC}/I_{AH} = 2$ showing the importance of the simplification used when accurate power consumption models are desired. Fig. 2.11 shows the two-dimensional(magnitude) magnetic field strength contours of the QUIC trap in the full elliptical case, clearing showing the appearance of two minima. As I_{QUIC} is increased, the field profile is warped until the minima merge.

In Section 4.5.1 we will discuss different trapping regimes for the various architectures, in such regimes it is possible to restrict the spatial degree of freedom and so derive some analytical equations for useful trap properties.

2.6.4 The Baseball Trap

The final trap we will consider here is the so-called Baseball trap, whose name origin is perhaps evident from Fig. 2.12 where the current path follows the route of a baseball (or tennis ball) seam. This trap is a reconstruction of the IP trap configuration however with the potential benefit of being one monolithic structure, and so requiring less control parameters. When originally discussed as a trap for neutral atomic species [118] there was some doubt as to the feasibility of actually producing an accurate realization of the current path, however we consider it here in the context of the development of additive manufacturing as a feasible production method.

The construction of the trap has the fewest variables, but bares some care in its definition; the current path is defined to exactly follow along the surface of a sphere of radius R_{sph} and is subdivided into four arcs, each of which exists in a plane which segments the sphere. The start and end points of each arc are pinned to the x-y plane, defined as per the axis in Fig. 2.12, such that the closest edge distance of each pair is solely determined by the variables R_{sph} and either the angle θ or ψ. The result is a continuous path in which each knitted to the next without overlap along the paths. For the regime where $\theta = \psi$ the trap symmetry means the relevant field minimum will be always at the trap center. We then can define the four arcs as follows,

$$r_{arc} = \frac{R_{sph}}{\sqrt{2}\cos\alpha}, \tag{2.39}$$

$$d_{arc} = \frac{R_{sph}\cos\alpha}{\sqrt{2}}, \tag{2.40}$$

$$\chi_{arc} = \pi + 2\arcsin\left[\frac{\sin\alpha}{(2-\cos^2\alpha)^{1/2}}\right]. \tag{2.41}$$

Here r_{arc} gives the radius of each arc, defined on the plane on which the arc is draw which intersects the main sphere; χ_{arc} is the total arc length; and d_{arc} gives the displacement projection onto the x-y plane of the arc defined from the arc origin to the center of the main sphere.

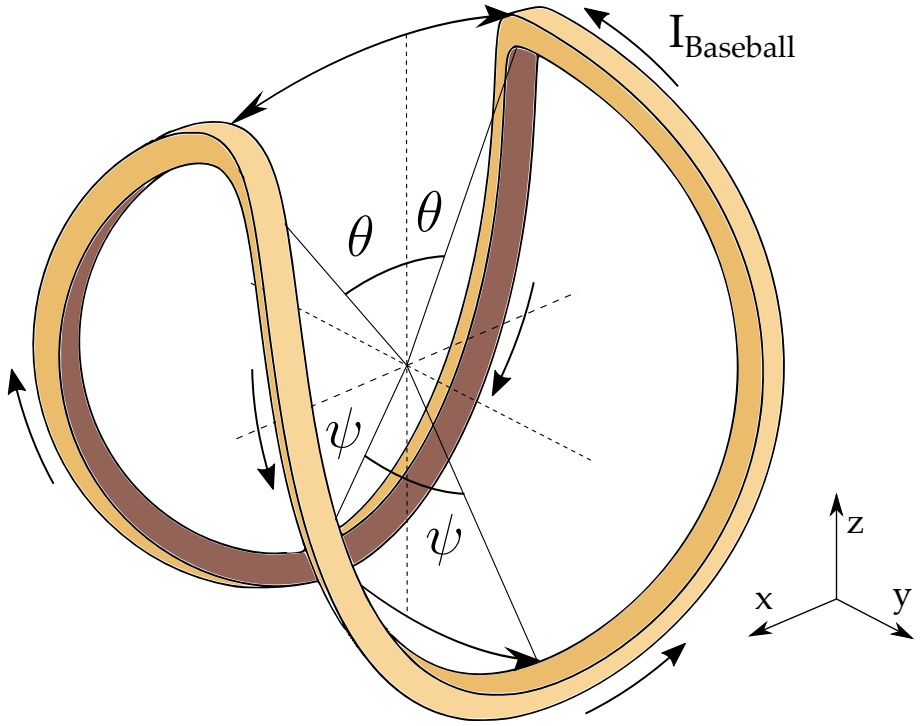

Fig. 2.12 Schematic of the Baseball trap as for magnetically trapping atomic specie. The current flows continuously between four arcs, which reside on a sphere of radius R_{sph}.

The fields calculations for the individual arcs are a more general classification of what we have discussed in Sec. 2.4.2, where the complete elliptic integrals are instead a limit of the incomplete elliptical integral formalism [119, 124]. As may be expected this complicates the calculation of analytical formula for all but the most simplified regimes, or in specific locations. Nevertheless, we define the field measured at a point $P(x,y,z)$ in cartesian coordinates as, [124]

$$\mathbf{B}_x = \frac{2r_{arc}(z-d_{arc})}{R^3}\left(\mathfrak{A}\sin\arctan\frac{y}{x}+\mathfrak{B}\cos\arctan\frac{y}{x}\right)\hat{\mathbf{e}}_\mathbf{x}\,, \tag{2.42}$$

$$\mathbf{B}_y = \frac{2r_{arc}(z-d_{arc})}{R^3}\left(\mathfrak{A}\cos\arctan\frac{y}{x}+\mathfrak{B}\sin\arctan\frac{y}{x}\right)\hat{\mathbf{e}}_\mathbf{y}\,, \tag{2.43}$$

$$\mathbf{B}_z = \left[\mathfrak{C}\frac{2k^2(r_arc^2+r_{arc}\rho)-2r_{arc}\rho}{R^3k^2}-\frac{4r_{arc}\rho}{R^3k^2}F(k^2,\phi_1,\phi_2)\right]\hat{\mathbf{e}}_\mathbf{z}\,. \tag{2.44}$$

In the above equations, we have defined, $\rho=\sqrt{x^2+y^2}$, the elliptical integral factor $k^2=4r_{arc}\rho/R^2$ and the distance $R=\sqrt{(\rho+r_{arc})^2+(z-d_{arc})^2}$, and the following terms,

$$\mathfrak{A} = \frac{2}{k^2}\int_{\phi 1}^{\phi_2} \frac{1}{\sqrt{1-k^2\sin^2\phi}}, \tag{2.45}$$

$$\mathfrak{C} = \frac{k^2}{k^2-1}\left[\frac{\sin\phi\cos\phi}{\sqrt{1-k^2\sin^2\phi}}\right]_{\phi_1}^{\phi_2} - \frac{1}{k^2-1}E(k^2,\phi_1,\phi_2), \tag{2.46}$$

$$\mathfrak{B} = \frac{1}{k^2}\left[\mathfrak{C}(k^2-2)+2F(k^2,\phi_1,\phi_2)\right]. \tag{2.47}$$

In which $F(k^2,\phi)$ and $E(k^2,\phi)$ are the incomplete integrals of the first and second kind [124], respectively. Finally, we define $\phi = (\arctan(y/x) - \chi + \pi)/2$. In the limit where $\theta = \psi = 0$, the arc planes become exactly parallel to the z-y or z-x plane, with respect to each pair, and the arcs themselves become half circles of $\chi = \pi$. The field magnitude in the center of the trap collapses to a surprisingly simple expression,

$$\mathbf{B}(x,y,z=0) = \frac{4I}{R_{sph}}\hat{\mathbf{e}}_\mathbf{z}. \tag{2.48}$$

Along each Cartesian axis one can then calculate the effective trap depths. Unlike for the IP trap, we will not be able to write exact analytical expressions for these values and will need to instead define some geometric common ground to compare the trap types. We can however find the location of the peak of the field magnitude along each cartesian line as $\pm x_{max} = \pm z_{max} = (2/3)R_{sph}$ and $\pm y_{max} = R_{sph}/\sqrt{3}$. Using these, the depths can be roughly found to be,

$$\mathrm{D}_y \simeq \frac{3I}{5R_{sph}} \times (67\mu\mathrm{K\,G^{-1}}), \tag{2.49}$$

$$\mathrm{D}_{x,z} \simeq \frac{2I}{R_{sph}} \times (67\mu\mathrm{K\,G^{-1}}). \tag{2.50}$$

2.6.5 Trap characteristics comparison

In this section we will look at a rough comparison of the magnetic traps discussed, which requires a somewhat similar geometry to be established. As the system with the fewest number of variables, we will use the Baseball trap definitions to then correspondingly define the fix other trap parameters. In the $\theta = \psi = 0$, we set $R_{sph} = 1\,\mathrm{mm}$ which we will take as just unity for now, since we are already working in the Gauss and millimeter assumption. This is experimentally challenging, but will provide an initial understanding of the problem. For the QUIC and IP traps, we then assume that the primary feature should match the size of R_{sph}, that is to say we set $R_{QUIC} = R_{AH} = 1$, for the QUIC trap, and similarly for the IP trap set $s_0 = 2/\sqrt{2}$ and $R_H = 1.5$. Moving to then define the final desired trap properties, a field minimum of at least 1 G is generally necessary to avoid Majorana losses. In regards to the trapping frequencies we look to contemporary work in high-rate portable systems [75], in which a tunable range up to 1 kHz is useful for fast evaporative cooling.

Implementing the geometric and desired trap characteristics into the systems described above, we find the following for the Ioffe-Pritchard trap: For a field minimum of 1 G, the axial frequency f_z has a maximum value of $f_z = (20/R)[\mathrm{Hz}]$, which occurs when $z_0 = 1.23R$ and $I_H = 0.317R$,

and gives a final depth of $D_z = 67\,\mu$K, independent of R itself. Thus for the case of $R_H = 3/2$, one finds $f_z = 13$ Hz, $z_0 = 1.8$ and $I_H \simeq 0.5$ A. The radial components are bound only by the provided current, with $f_{x,y} \simeq 36 I_W\, textHz/A$ and $D_{x,y} \simeq 220 I_W\,\mu$K. Typically the trap depth is given as the smallest cartesian depth calculated, and so the quoted depth for the IP trap is $D_{IP} = 67\,\mu$K.

For the Baseball trap, to ensure a trap bottom of 1 G, the current must be fixed at $I_{BB} = 0.25 R_{sph}$ directly from Eq. 2.48. The frequency dependencies can then be found numerical approximations of the field to scale as, $f_{z,x} = 12.7\sqrt{21I/R_{sph}^3}$ and $f_y = 12.7\sqrt{8I/R_{sph}^3}$. Fixing the field minimum fixes the dependent I and so in turn for our case where $R_{sph} = 1$, we find the smallest depth, which occurs along the y axis, $D_{BB} = 10\,\mu$K. Trapping frequencies are then $f_{x,y,z} = (30, 18, 30)$ Hz.

Finally we consider the QUIC trap, which is somewhat unsatisfying to calculate as no simple formulae become apparent. The simplifying approximation in the other cases in which we can assume, for all presented variables, the field minimum is at the geometric origin is no longer possible. Using the rough geometric equivalent variables as above, we can find numerically the following trap properties for a field minimum of 1 G, which occurs along the x axis at $x_{min} = 0.73$: the trap frequencies are $f_{x,y,z} = (38, 95, 98)$ Hz with the smallest trap depth calculated to be $D_{QUIC} \sim 430\,\mu$K.

A quick comparison of the three traps shows that none of them are truly ideal. Enforcing a field minimum of exactly 1 G, as well as maximizing the field curvature (and directly then the trap frequencies), severely limits the traps experimentally. A clear case in point are the achieved trap depths. An atomic ensemble's average temperature after sub-Doppler cooling processes is likely to be on the order of $5 - 20\,\mu$K, depending on the alignment and balancing of laser beams. As the distribution of atoms is of a Maxwell-Boltzmann type, there will be a significant fraction of hot atoms greater than this average. To ensure these hotter atoms are captured, it is typical to have the trap depth to $10T_{avg}$, where T_{avg} is the average temperature of the Boltzmann distribution of the atomic ensemble. From our calculations, we see only the QUIC trap has a comfortable minimum trap depth. This trap however suffers in its flexibility, and high trap frequencies are not possible with the same geometry, limiting its application for high-rate evaporative cooling, which will be discussed more in Chapter 4.

Chapter 3

The Cylinder Trap

3.1 Cylinder trap motivations

The field of quantum technologies has undergone a rapid expansion in the last decade. Quantum sensors in particular, as a sub-field apart from quantum computing and quantum simulation, has seen notable strides forward in device sensitivity and resolution [33, 73]. However much of the state of the art is restricted to laboratory based experiments consisting of meter-scale laser-preparation tables (optical tables), bulky vacuum chambers and associated pumps, and numerous supporting electronics and computer systems. This is a significant technological bottle-neck to the ever increasing number of potential applications for a device which makes use of the high sensitives and resolutions achievable, whilst being robust, low-footprint and low-power.

There is no obvious singular direct technological or scientific leap to such a device. That being said, it is possible to isolate sub-components which are common among these sensors and investigate novel techniques to build on the progress so far. This chapter presents work done to this aim: an additively manufactured device providing a quantum resource through the production of trapped cold atomic gases. Such a device would provide an initial source of cold atoms which would then be transported or integrated into a secondary region, depending on the desired experimental/sensing regime.

The passive capabilities of the specific material and production method used are arguably secondary to the main active performance benchmark of a quantum resource: the production of a significant magnetic trapping field for the capture and cooling of atomic species. Nevertheless, one of the key goals of this work was to investigate the viability of additive manufacturing, in general, as a method for producing whole, or parts of, quantum devices. Specifically, we first considered whether components produced would survive in an ultra-high vacuum environment at all. Leading from that, it was logical to consider then if a structure made via 3D-printing would be able to *contain* a UHV environment for an appropriate amount of time.

Here we will first discuss the design choices and methods used in creating the so-called cylinder trap, followed by a brief overview of the additive manufacturing considerations required and processes used in creating the device. Finally, results for the trap will be presented in comparison to what is achieved by standard techniques. The main results of this chapter form the publication in Reference [94].

3.2 Cylinder trap design aims

With the overall goal being the production of a quantum resource which makes use of additive manufacturing as a production method, more technical design aims had to be outlined for a quantifiable metric of the final device performance to be established. Below lists a selection of criteria for the device, which are roughly ordered in terms of relative importance.

- Production of $\sim 10^8$ cold atoms
- Minimal electrical power consumption.
- Produces a close approximation to a quadrupole field.
- Design achievable with standard 3D-printing capabilities.
- Connection to electrical feedthroughs.
- Adequate thermal mass to minimize deformity from joule heating.

Atom number The quantum resource would sit as a first-step as part of larger experimental or sensing apparatus, and so the target atom number it should produce depends on the specific end-goals. However, across nearly all regimes there are inevitable losses for numerous experimental reasons, but critically during the cooling and compression of the atomic vapor. Thus a higher initial atom number is almost always desirable.[1] The value ($\sim 10^8$ cold atoms) given is one from empirical observations from our peers [125] but serve only as a guide.

Power consumption Most laboratory experiments need not worry about the power consumption of their devices, up to the limit of what is achievable with their local power grid. It is perhaps obvious that the same cannot be said for any device which hopes to be portable. Critically we are only considering the electrical power consumed in generating the magnetic trapping field required by the device; we are ignoring the power consumed/required by lasers, computer control systems and vacuum maintenance. We are careful to distinguish this work apart from any efforts to theoretically derive a truly minimized power consumption, and we simply wished just to reduce the required power by some significant amount rather than use iterative algorithms to find a true global power minimum.

Field properties The model of efficient trapping and cooling of atoms in a magneto-optical trap assumes that within the trapping region the magnetic fields vary linearly and are aligned correctly to the polarization of the laser fields. This linearity is only true for the case of a pure quadrupole field. Higher order field components will reduce the overall trapping force and cooling effect, as well as reducing the exact alignment of the laser and magnetic field axes. An ideal infinite linear field is of course not possible, but a close approximation will have cascading benefits for the final atom cloud properties, specifically in terms of trapping efficiencies and final atom numbers.

3D-Printing suitability Additive manufacturing, or '3D printing', has a strong disruptive potential to traditional manufacturing method. However, there are limitations to what is it capable of, more thoroughly discussed in Section 3.3, which must be taken into account when a design is

[1] To avoid upsetting my ion-trapping colleagues, I'm only considering atomic vapors/clouds.

made. Ideally our design would be complicated enough to make traditional manufacture somewhat inconvenient, without overcomplicating the design to the point that printing is no longer feasible.

Power/electrical connection This requirement is arguably experimental convenience than a necessity; the structure must be able to be connected to off the shelf power connections (also known as power feedthroughs) which pass through the vacuum chamber wall. In principle a bespoke connection could be made to clamp the structure to such a feedthrough; however, with the freedom of additive manufacturing, as discussed next, it was hoped that the structure itself could be designed to readily fit onto a commercial device.

Thermal mass The expected outcome of the work was the production of a small, i.e. cm, scale object carrying current. Larger scale externally mounted coils often require $10-100\,\mathrm{A}$ which can generate a significant amount of joule heating and can often require water cooling, even with the benefit of convective air cooling. The deformations in the magnetic field profile due to this heating are negligible with respect to their overall affect on the atoms. However in a much smaller system, where thermal deformations may occur on the same scale as the object size, it may be possible to observe a change in atom number or shape. The final device must either then be sufficiently passively cooled, or have enough thermal inertia that induced mechanical stress/strain are minimal on the timescale of measurement.

3.3 Additive manufacturing considerations

Additive Manufacturing has the potential to provide a step-change for both prototyping and mass-production of devices and structures. The ready paring with commonly found CAD [2] packages and the availability of open-source software and hardware provides a wealth of both highly academic and hobbyist knowledge to produce almost arbitrary designs. Nevertheless, there are restrictions. In this section we discuss the design considerations required by these restrictions for our specific printing technique, in regards to the production of a quantum device.

Selective Laser Melting (SLM) was the chosen technique to 3D-print our device [126]. This method employs a high-power ($200\,\mathrm{W}$) laser beam to melt a fine metallic powder, layers of which are added successively by a mechanical sweeper within an inert gas environment. Structures are formed 'bottom-up', beginning first with several layers which are melted directly onto a large build-plate. This method allows for numerous alloys to be printed: aluminum, titanium, stainless steel, steel and silver [127]. The variables for printing method, material and environment leave a staggering amount of parameter space to be explored by those who work in the field, meaning some materials in particular are more well understood and their printing more reliable than others. Further, choice of material and the post-treatment processing defines a common range of final mechanical, thermal and, critically for the generation of magnetic fields, electrical properties [128].

The layering of successive materials requires a distinct approach when structures are designed. Traditional techniques create the desired shape(s) through milling or cutting out material from solid blocks. Tools must be manipulated on numerous degrees of freedom to achieve this, and when paired with computer guided software leaves an impressive parameter space for machinists to work with. SLM, and other similar methods, construct components as successive layers which,

[2] Computer Aided Design - e.g. Solidworks, Ultimaker Cura

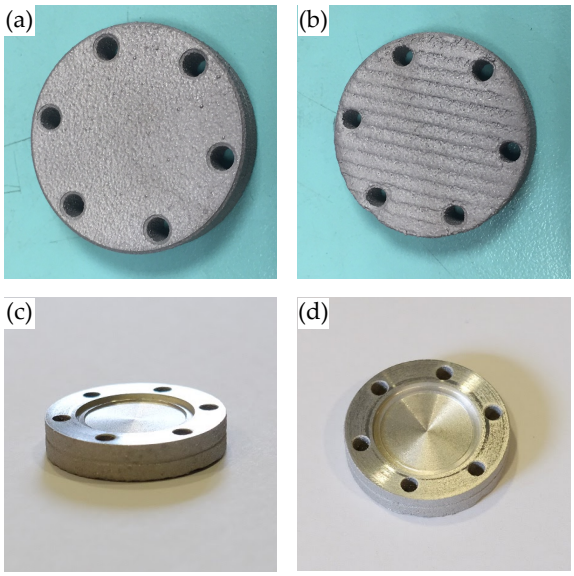

Fig. 3.1 Images of a CF16 3D printed vacuum flange. (a) Post-printing, top surface of the flange. (b) Post-printing, bottom surface of the flange. Ridges where the support structs were printed and then removed are clearly visible. (c) Glancing view of flange post-processing, showing the knife edge on the internal ring. (d) Top view of post-processed flange.

after the initial base-plate layer, must be self supporting. The designer must carefully consider overhangs, regions where material protrudes away from the main structure, that require a scaffold of additional material to be removed in post-processing. Internal voids, which are difficult to manufacture traditionally, can be created but, as in the case of SLM, any un-melted alloy powder will be trapped unless holes are included in the original design or drilled in after. Further, the appearance of stress-induced warping is a common problem. Thin layers experience high thermal gradients and mechanical strain from layering which make un-supported parts highly prone to warping during manufacture.[3]

[3] Whilst our experience of this field is academic, a great number of amateur and professional guides exist for similar problems in polymer printing and can provide some insight [129]

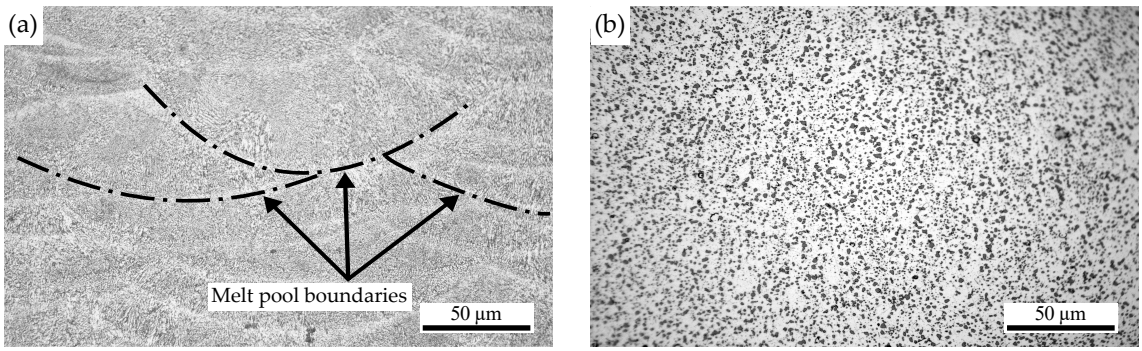

Fig. 3.2 Optical microscope images showing typical surface patterning of SLM-printed structures, specifically an Al-Si10-Mg alloy. (a) An as-printed structure immediately after manufacture; darker grey regions are separated by channels of lighter material which form during printing. (b) After solution heat treatment (SHT) a more uniform distribution of silicon pools in a mesh of dark grey is seen. The scale bar depicts 50 µm.

In regards to the microstructure produced, powder based printing methods raised a number of potential impediments for our application as the grainy nature of the powered layers and resultant surface finish are generally incompatible with ultra-high vacuum-based technologies[90, 91, 130]. It was also speculated that the melting pools of powder may form air pockets where gases could leak from within the vacuum or even cause micro-craters if they are near the surface. In Fig 3.1 (a) and 3.1 (b) we show a CF16 vacuum flange-like structure which was printed via SLM in an aluminum-titanium-silicon alloy. In the first figure you can clearly see the grainy surface profile of the flange, whilst in the second the ridges are from the, now removed, structural supports which are cut from the printed surface a with wire erosion technique. The grained surface demonstrates the threshold for the smallest surface feature possible with SLM, and is not at all suitable for a CF-style knife formed (printed) as part of the monolithic component, as was the original intention. In order to solve that and to get an understanding of the internal structure, material was milled away in post-processing in order to create a knife-edge profile, as can be seen in Fig 3.1 (c) and 3.1 (d). From these images the material seems mostly uniform and without visible air pockets.

Once printed, there exists a growing tool box of post-processing techniques [89] with which mechanical properties such as stress, strain, elasticity and durability can be tuned. Solution Heat Treatment (SHT) is one such method [131–133]. Fig 3.2(a) shows an optical micrograph of a material printed in SLM, specifically in this case an aluminum-silicon-magnesium alloy. As successive layers of material are added and melted, heterogeneous boundaries form which directly impact the macroscopic mechanical response of the structure; typically the response is direction dependent, e.g. differing perpendicular or parallel to the print direction. It was suspected that these irregular formations may also affect the flow of current. The SLM process restructures the material into a more homogenous distribution of silicon particulates suspended within an aluminum matrix, akin to a raisin pudding, see Fig 3.2(b). The clearer pathway for current to flow would hopefully improve electrical conductivity, whilst the resultant mechanical changes would likely be negligible for our applications. This electrical result was so far untested.

3.3.1 Printing details

With the general design aims given in the previous sections, along with the broad additive manufacturing considerations, we are still left with a vast parameter space of variables to chose from. However the choice of material was limited by external constraints on the machinery used, which left us with just one option, an Al-Si10-Mg alloy. Whilst not the most conductive material available for printing, with a silver alloy being possible, it left us with enough scope to trial as a prototype quantum resource to test our design criteria. Given that, what follows is the specific printing methodology and post-processing used.

A Renishaw AM250 selective laser melting (SLM) machine is used to produce Al-Si10-Mg samples from a powder-alloy of chemical composition Al 88.9 wt%, Si 10.7 wt%, Mg 0.5 wt% (particulate sizes 15 μm to 100 μm) [126, 133]. Structures are created by melting the successive layers of powder with a 200 W Yb-Fiber ($\lambda = 1064$ nm) laser. Here Al-Si10-Mg, as opposed to other alloys, is used for the convenient electrical properties and low cost.

Once printed, the structure is heated at 520 °C for 1 hour, followed by water quenching and artificial aging at 160 °C for 6 hours with both steps carried out in a pre-heated furnace with an air atmosphere [131].

3.4 Cylinder trap design iterations

With the considerations outlined in Section 3.3, we began to form the basic shape of the atom trap. One of the primary guiding principles is to maximize the volume of the current carrying material, i.e. maximizing the current density, around the trapping region and so reduce the required electrical power. The trap region defined a restricted volume where no material can exist, and is given by the crossing of six laser beams of diameter D forming a tri-cylindrical region. Our sister labs commonly accommodate beams of diameter between $25-50\,\text{mm}$, which is a product of the most readily available optics, and so we aim to have a system using beams of 15 mm. There is no strict upper limit to how large our device could be; however, our prototype should fit well within the internal volume of off-the-shelve components which from our available stock allowed for a maximum volume of $35\,\text{cm}^3$ with a largest dimension of 5 cm. Further, the device's smallest features cannot be such that the structure warps during printing, from empirical deduction this suggested cross-section areas of no smaller than $2-4\,\text{mm}^2$.

Our aim is the generation of a magnetic quadrupole with the trap. The exact path of the current flow which best uses this volume could have been algorithmically optimized. By defining limiting behaviors, such as optimal power consumption, low heating, minimal structural deformity, low inductive response, high magnetic field linearity and higher order field suppression, one could envision how enough parameters may be defined in order to minimize an appropriate cost function. However the ratio of relative effort to output for such an analysis in this project is limited, as there is still significant uncertainty as to the viability of any printed material in UHV. To simplify the process, the current path around the available volume was shaped by cutting the conductor into separate monolithic components, approximate to one of the common geometries seen in magneto-optical (and magnetic) trapping, see Sec. 2.6. The result leaves a shape which is subjectively similar to the Ioffee-Pritchard scheme, see Sec. 2.6.2 and Fig 2.8, with mismatched currents in the straight arms, as shown in Fig 3.3(a).

Translating this path into a printable structure, we worked towards a design which would be simple and small enough such that the printing time would be minimal, i.e. on the order of eight to twelve hours. To converge our design features and aims into a final printable device an iterative process took place in which CAD models were fed back into finite element simulations. The final printed structure is shown in Figure 3.3(b), with a digital render with laser beams shown in Figure 3.3(c). The full design iteration process is described in detail below, here we list the brief key features.

The trap, commonly referred to here on as a cylinder trap, consists of two monolithic components SLM-printed and heat treated as per the details in Section 3.3.1, in an AlSiMg alloy. Electrical isolation between the parts is maintained by air (or vacuum) gaps, and electrical contacts to commercial power feedthroughs are made through two clamping structures on each 'half' of the device; these are the rectangular forms in Fig 3.3(b). These connecting arms also serve as

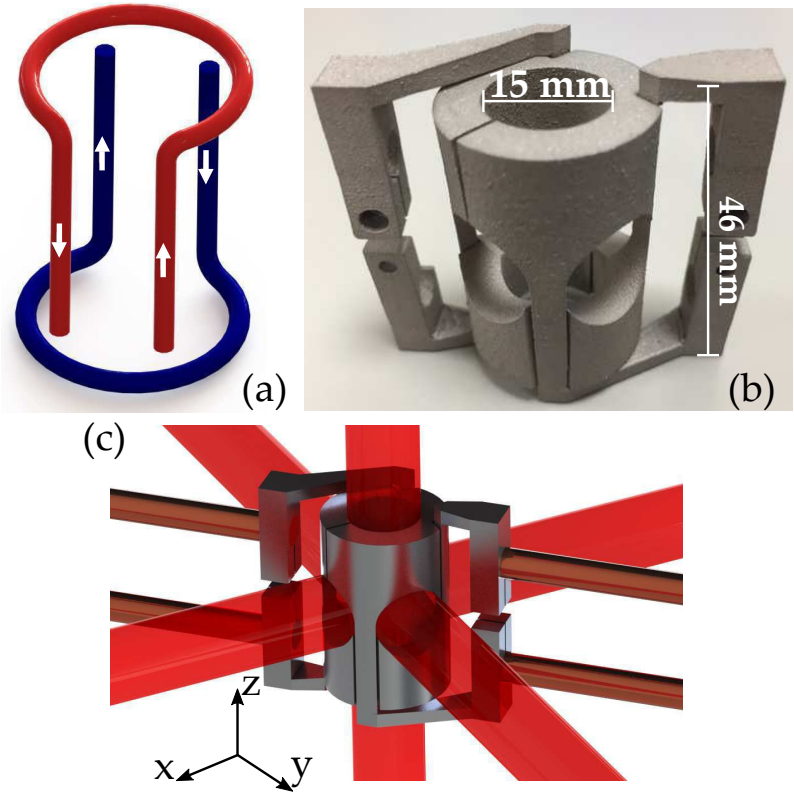

Fig. 3.3 (a) Schematic of the cylinder atom-trap current flow. (b) 3D-printed atom trap structure. (c) Digital render of the cylinder structure shown with vacuum feedthroughs and laser beams.

the structural anchor for the two pieces, and as heat-sinking pathways via the feedthrough pins. Bearing in mind the limits of additive manufacturing, we chose a shorter feedthrough connection to avoid warping during manufacture, as well as having a cross-section large enough that the material would be self supporting after printing struts were removed. Excessive material, where little current flows, was left on the top and bottom (z-axis) of the structure to provide more thermal mass to the device. In addition, having the electrical connections/arms further from the central trapping region minimized any contributions these may have had in the final magnetic field.

Iteration Process By quantifying the aims in Sec. 3.2 we evaluated various iterations of the cylinder trap to make a justifiable choice of final design. This analysis is of particular importance as the final structure will occupy a fraction of the volume when compared to traditional externally mounted coils, and the distance atoms are from the material surface will be equitable to the devices feature size. The result is that any divergences away from an ideal quadrupole due to non-ideal geometry or irregularities in printing will have a much greater effect, as the field such irregularities produce could be non-negligible when compared to the bulk-field of the device.

We show a selection of the design iterations in Fig 3.4, each of which were attempts to understand how the magnetic field responds to changes in the structures architecture. Fig 3.4(a) shows the initial form designed following the rough current paths of an Ioffe-Pritchard trap (Sec. 2.6.2), this later became the core structure which formed the final trap design, shown in Fig 3.4e, with the addition of electrical clamps. In Fig 3.4(b) widely spaced connective arms were added as a precursor to the electrical clamps in order to test their perturbative effect on the final

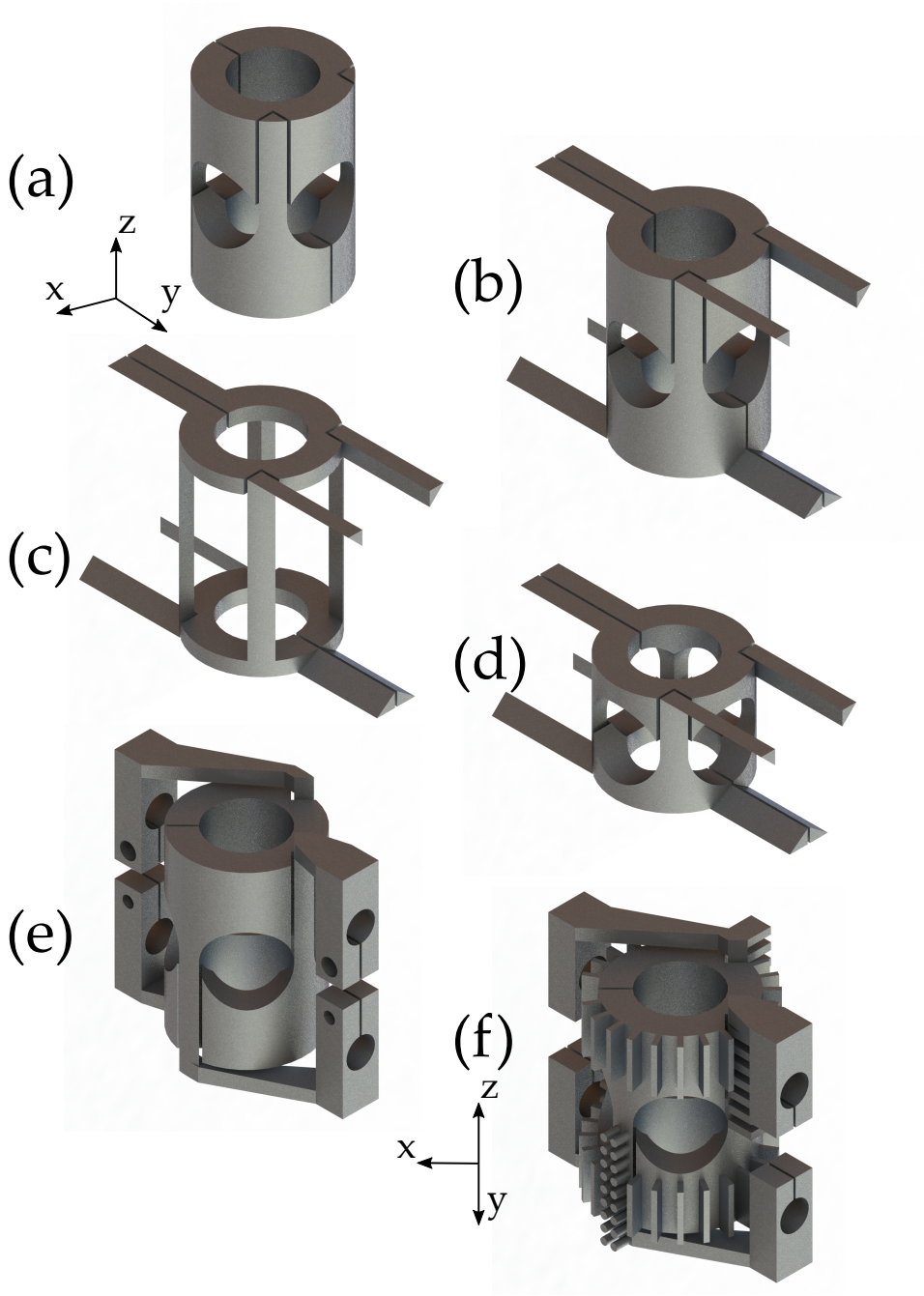

Fig. 3.4 Iterations of the Cylinder Trap design. A selection of designs generated within a CAD package, and then simulated in finite-element software environments. (a) Core final design. (b) Addition of connecting arms and support structs. (c) Removal of internal material to create more uniform current density. (d) Shrinking of internal volume to conserve power. (e) Final design, with feedthrough clamps. (f) Increasing surface area for great radiative thermal emission. The evolution of the trap was driven by the cylinder trap design aims, see text for comparison and results.

magnetic field. Narrower arms were added with the intention of providing structural support, although they could also be used as alternative electrical contacts. Figures 3.4(c) and (d) show attempts to generate more uniform current densities through the whole path of the device, in a tall (c) and short (d) form case. Finally, Fig 3.4(f) shows the design as in (e), but with fans and protrusions in order to increase the total surface area to improve the rate of radiative cooling.

Current flow It was natural to assume, based on our understanding of anti-Helmholtz coils, that the strong axis of the magnetic field produced by the schematic in Fig 3.3(a) would align with the z-axis. This was quickly found not to be the case once the design in Fig 3.4(a) was proposed. The cause is best demonstrated by first extracting data from a electrical current finite element (COMSOL) calculation and then choosing the highest percentiles of the current elements it outputs. The resultant current-elements are normalized, for visual aid, and plotted in Fig 3.5, effectively showing the highest concentration of current density. We see, most prominently in Fig 3.5(b), that the structure forms effectively two anti-Helmholtz loops along its x-axis, which dominates the incomplete loops oriented along the z-axis.

Retrospectively this result was not surprising as the current will always take the path of least resistance, which in our case, where material density and microstructure has been homogenized, is equitable to the shortest distance. The regions where relatively small amounts of current flow could in principle be removed, which guided the iterations as in Fig 3.4(c-d), where the current density was made uniform through the device by ensuring a roughly constant device cross-section, see Fig 3.5(c). Once the field characteristics are taken into account, however, we find that trying to maximize only the current density is not sufficient.

Field gradient As we have seen in Chapter 2, it is the strength of the linear magnetic field gradient, when paired with correctly prepared laser fields, which determines the upper capture velocity limit and the cooling distance required for a specific species of atom. To produce any gradient the structure must consume electrical power, scaling as $P \propto I^2$, and so we can rank the performance of our designs in terms of the field gradient per amp, $\mathrm{Gmm^{-1}A^1}$. For the designs (a-e) in Fig 3.4 we find $\mathrm{d}_x\mathrm{B}_x/\mathrm{A} = (-7.5, -7.2, -5.8, -7.7, -7.8) \times 10^{-2}\,\mathrm{Gmm^{-1}A^1}$, which gives the magnetic field gradient for the x-axis component of the magnetic field along the x-axis itself, which for all cases is the strong axis of the field, as per the coordinate definition in Fig 3.3. The calculated values of $\mathrm{d}_x\mathrm{B}_x/\mathrm{A}$ are comparable, with a clear exception in (c). This is most likely a result of the long and rectangular form of the current path given by iteration (c), where the dimensions no longer adhere to the ideal anti-Helmholtz configuration of $d = R$, where d is the center to center distance of two loops of radius R.

We expect that the strong field gradient should have the ratio $-2:1:1$ with respect to the two other axial components, which is the characteristic signature of a ideal quadrupole field, and equally of an ideal anti-Helmholtz configuration. We get the following ratios for cases (a,b,e) $(2.00:1.01:1.01), (2.00:1.06:0.94), (2.00:0.97:1.03)$ and for (c,d) we find $(2.00:1.57:0.40), (2.00:0.60:1.40)$, having grouped together similar structures. We clearly see that cases (c,d) are not at all adequate. In particular for case (d), the current paths along the prongs have a greater effect on the field within the main trapping volume simply due to their proximity. This additional, and non-negligible contribution is detrimental to the quality of the final quadrupole field.

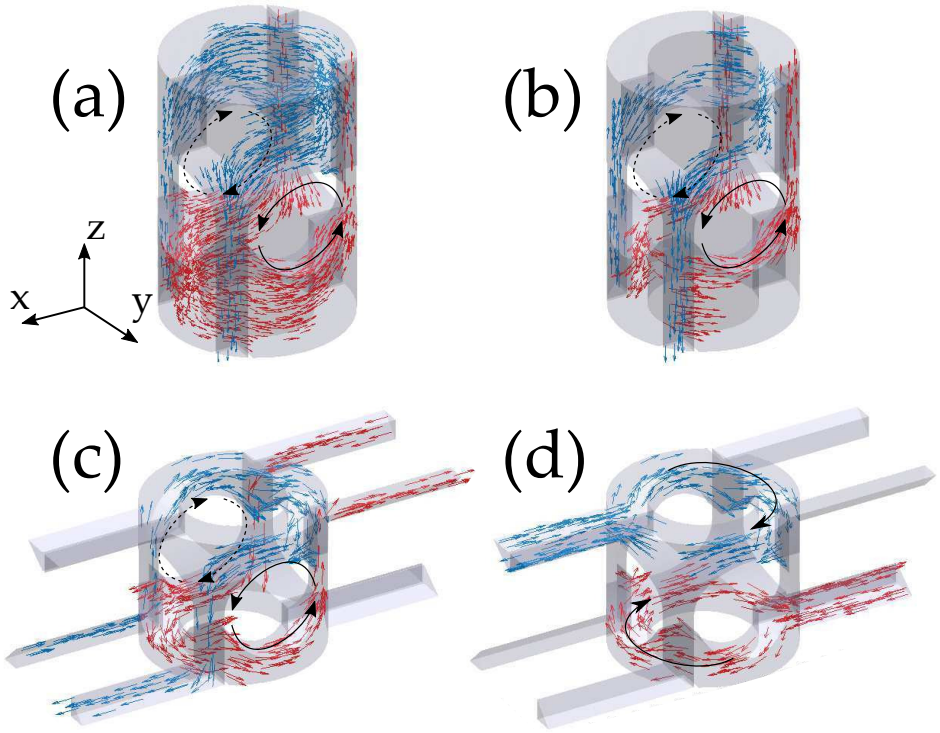

Fig. 3.5 Variations in majority current flow in the Fig 3.4(a) and Fig 3.4(d) designs, each case shows normalized current magnitudes. Arrows indicate current flow direction. (a) Path of largest 40 % of current magnitudes. (b) Path of largest 10 % of current magnitudes. (c) Path of largest 40 % of current magnitudes, in the standard configuration. (d) Path of largest 40 % of current magnitudes, in a Helmholtz configuration using the alternative electrical contacts.

Linear region In order to provide an estimate for the linear region extent for each design, we compare $\mathrm{d}_i\mathrm{B}_i$ $(i = x,y,z)$ calculated at the origin $(x,y,z = 0)$ to the magnetic field gradient component along each axes. Calculating the divergence of the respective field gradient along each axes with respect to the gradient at the origin, we set a threshold of 20 % past which the field is no longer considered linear and thus has an increasingly negligible contribution to the efficient cooling and trapping of atoms. This approximation is rough, but we can justify disregarding the field after this threshold as the gradient tends to zero away from axis as the point of interest approaches the current carrying structure. In the 20 % threshold, the linear regions are $(\Delta x, \Delta y, \Delta z) = [(5,5,5),(6,6,8),(5,6,3),(6,6,6),(6,6,9)]$ mm for cases (a-e) respectively. The ratio of the linear extends is a direct reflection of the field gradient magnitude ratio, and so in cases (a,b,e) which are effectively identical, with each having the same core architectural features, we see rough agreement from the field gradient result. While for cases (c) and (d) we again see how the geometry of the device causes a significant divergence from the required quadrupole field.

Effective volume As an extension to the axial linear region, we can take the values calculated further, and calculate an effective trapping volume, where we are assuming a cuboid volume whose three spatial dimensions are given by the values $(\Delta x, \Delta y, \Delta z)$ found above. This volume would ideally match perfectly the overlapping region defined by the six laser beams. This in itself requires clarification: the symmetric cuboid volume whose length (and width, height) is given by the beam diameter, D, has a value $V_{cuboid} = D^3$; while the true tri-cylindrical volume (a so-called tricylinder

Steinmetz solid) defined by the three beams is $V_{Steinmetz} = 8(2-\sqrt{2})D^3 \approx 4.7D^3$. For the case of a 15 mm beam size, this gives 16×10^3 mm^3 and 9×10^3 mm^3 for the cuboid and Steinmetz volumes, respectively. Compared to the effective linear volumes supported by the geometries in Fig 3.4 one gets, in order (a-e), $V_{linear}/V_{Steinmetz} = (0.21, 0.21, 0.07, 0.14, 0.24)$. These ratios provide a guideline to compare how the far the linear field gradient region extends across the total volume defined by the overlapping beams. Larger values are desirable for our design.

Thermal behavior Joule heating is a natural consequence of passing a current through any material with non-zero resistance. Generally a low steady state temperature is required, with the device in question losing heat through contact with thermal baths, convective air flow or, to a lesser extent, radiation. Coil systems typically rely on liquid cooling systems, or implement cooling-down times between cycles allowing for heat to dissipate. Increasing the overall cycle time goes against the principle of a device with a high atom output rate. Heat removal in vacuum environment is further complicated as there is no air to induce convective cooling, and water cooling has the risk of flooding the vacuum chamber. The result is that device has to rely solely on the thermal contact provided by the electrical feedthrough connections, and so the simplest way to reduce the final device temperature is to ensure a low a current as possible is used to generate the magnetic field.

3.5 Cylinder trap characteristics

3.5.1 Cylinder thermal and electrical properties

Following printing, the cylinder trap's electrical and thermal properties were characterized in order to test and verify the effects of solution heat treatment, and create a benchmark for analysis for when the cylinder is no longer directly accessible, i.e. mounted within the vacuum system. The resistivity of the material before and after SHT was of particular interest. Four point current-voltage (I-V) measurements across a treated structure yielded a cold resistivity of $5 \times 10^{-8}\,\Omega$m or a resistance of $(640 \pm 4)\,\mu\Omega$ for our geometry which is a 20% reduction when compared to the as-printed structure (non-treated) resistance of $(800 \pm 20)\,\mu\Omega$. A direct comparison of pure aluminum puts the conductivity of this Al-Si10-Mg alloy at 70% of the value for bulk material at room temperature. Whilst there seems to be a clear correlation with the heat treatment process and the resultant conductivity, the exact nature of the improvement is still under investigation [94]

The dominant cooling mechanism of the mounted device is thermal conduction through the electric feedthrough simultaneously serving as mechanical mount. The body of the vacuum chamber serves as a secondary, much larger, heat sink to this. Convection (air cooling) is irrelevant in this set-up, however in-situ measurements were not possible in our setup. To estimate the thermal behavior of the device when installed we performed air-side measurements of the steady-steady temperature resistance for various applied currents, up to 50 A. This would allow for a calculate of the temperature coefficient α described as $R = R_0[1 + \alpha(T - T_0)]$, where R_0 and T_0 are the room temperature resistance and the room temperature, respectively. A value of $\alpha = (3.6 \pm 1) \times 10^{-3}\,\mathrm{T}^{-1}$, which puts it within the region of bulk Aluminum [134]. At 50 A, the highest steady-state temperature in air was found to be 36 °C, measured at the corner of one of the cylinder arms.

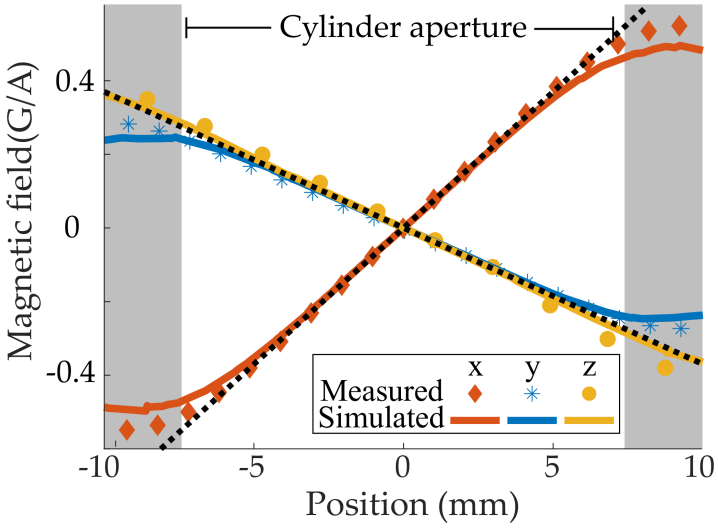

Fig. 3.6 Plot of calculated (finite-element) versus measured magnetic field magnitude along each axial direction. Dotted lines here show ideal $-2:1:1$ ration between strong and weak axes. Along all three optical axes, the linear field region extends over the full cylinder aperture, ensuring optimal laser cooling.

3.5.2 Field characteristics

For MOTs using ^{87}Rb a trapping magnetic field gradient of $\sim 10\,$G/cm along the strong axis is typical. In the ideal case fields would be perfectly linear within the trapping region, which for the cylinder is roughly defined as the region of the six overlapping laser beams. The finite element calculation of the predicted magnetic field profiles, for the design shown in Fig 3.4, along each cartesian axis is shown along side measurements along the same axis in Fig 3.6. Field measurements are taken using an axial field probe on a Hall effect Gaussmeter (Hirst GM08). The fields produced by the cylinder are a close fit for the fields which would be produced by an equivalent anti-Helmholtz configuration, having both the $-2:1:1$ ratio between the strong and weak axes as well as the same field geometry. A subtle, but important, observation should be made here regarding the primary axis of the cylinder trap. The strong-axis of the trap actually points along the x-axis, and not, as would be expected for Helmholtz loops, along the z-axis. This is a result of the current-flow as discussed in Fig 3.5, and has a natural consequence on the choice of light polarization in order to achieve the correct addressing of the magnetic sublevels shown in Fig. 2.3. Specifically this means we must switch the circularity of the light for z- and x-axis.

A field gradient of 10 G/cm is achieved for an input current of 14 A thus meeting the empirically set target, and in agreement with the finite element calculation, $-7.8\times10^{-2}\,$Gmm^{-1}A^{-1}, while still providing a significant range of currents, $1-50\,$A, for optimization and testing within the range of negligible Joule heating. Measurements at currents up to 50 A with corresponding gradient of 37 G/cm have been performed, which confirmed the expected linear relationship between field gradient and current.

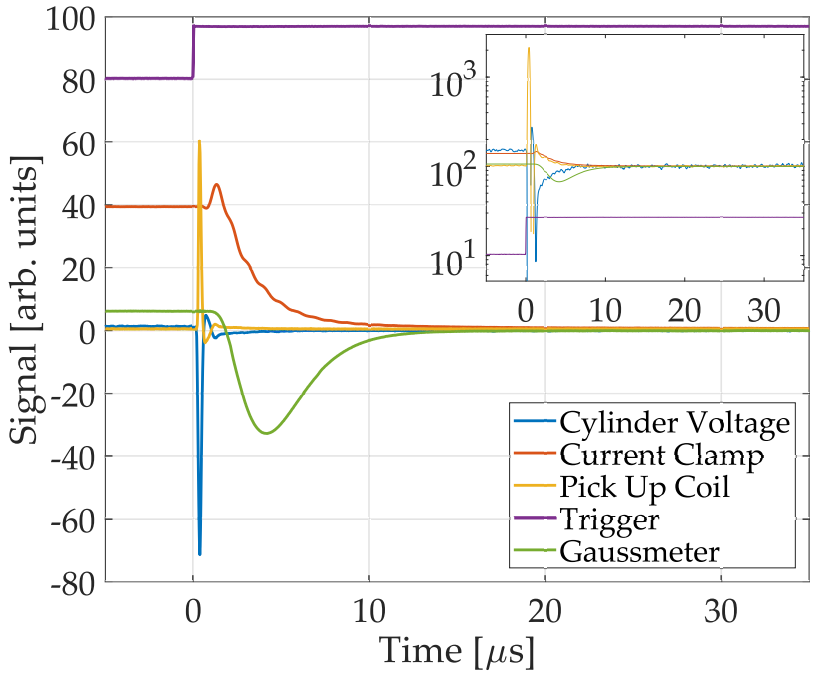

Fig. 3.7 Magnetic field decay measurement. The plot shows the characteristics of the switch-off process for the cylinder, using a current of 15 A. The voltage across the device itself (blue trace) is displayed, along with the current flowing via a current clamp (red), after sending a trigger (purple) to open an IGBT. Also shown is the voltage induced in a pick-up coil due to changes in the magnetic field (yellow), along with the signal from a Hall effect Gaussmeter (green). After an initial transient period, the Hall probe signal decays to below 10 % of its initial value within (13.0 ± 2.3) µs, after which time all signals settle to their steady state background readings. The inset depicts the same data set on a semi-log plot to emphasize the similar decay times of all measured signals, as well as exaggerating the smaller features of the signals. A fast-switch is achieved as a result of bespoke, in-home constructed electronic high-current switches, which were inherited by the author from a previous researcher.

3.5.3 Cylinder trap inductance

The sensitivity of the trapped atoms to magnetic fields is critical to trapping them, however they are just as sensitive to extraneous stray fields. These could be from an environmental source or experimental noise. Of particular concern to experimenters are those generated from eddy currents induced from the inductive properties of the trapping structures or even their housing, i.e. the vacuum system itself. A key advantage of any trap designed to be housed within the vacuum system is that one need not consider eddy currents induced within the chamber walls. However, internally mounted chips, coils and the cylinder trap will have a characteristic decay time which must be understood. Magnetic fields generated by the structure(s) after switch-off can limit the experimental cycle length in typical cold atom devices.

To characterize this switching process, the voltage across the cylinder was measured along with the current flowing through it using a current clamp (Chauvin Arnoux P01120043A), as a function of time after opening an insulated gate bipolar transistor (IGBT). In addition, the magnetic field inside the cylinder during the switching was measured using a Hall effect Gaussmeter (Hirst GM08) and its derivative with a small single-turn pick-up coil. Both the Hall probe and the pick-coil were

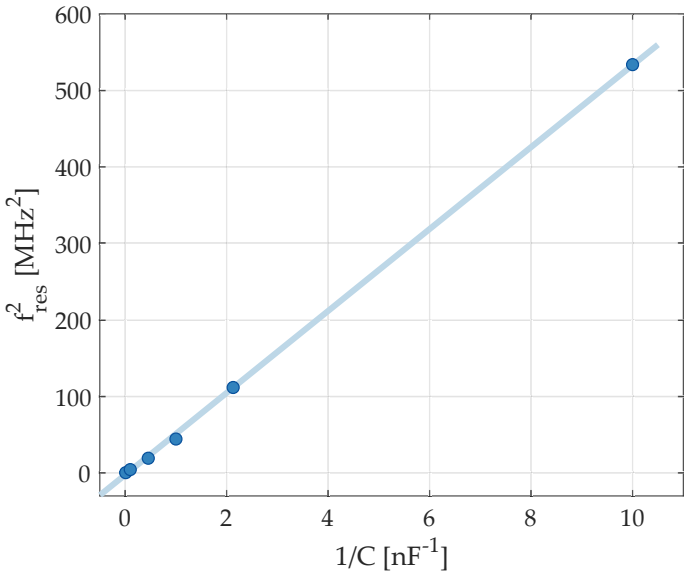

Fig. 3.8 Cylinder inductance measurement. A plot showing the resonant frequencies, $f_{\text{res}}(C)$ of a parallel *LC* circuit for various known capacitances, from which an inductance of $(0.49 \pm 0.05)\,\mu\text{H}$ is extracted from the linear fit, as described in the text.

oriented along the strong eigenaxis of the quadrupole field, at the position of largest field. The results are shown by the signal traces in Fig 3.7, obtained for a current of 15 A, corresponding to a magnetic field of (6.2 ± 0.6) G at the position of the Hall probe.

Shortly after opening the IGBT, a large fly-back voltage develops across the cylinder, as expected when switching a current through an inductive load. Some oscillatory behavior can also be seen, arising due to contact resistances and small parasitic capacitance and inductance within the circuit, which are non-negligible in comparison to the impedance characteristics of the cylinder itself. Following the initial transient period of the switching process, the magnetic field measured with the Hall probe is seen to decay below 10 % of its initial value within $(13.0 \pm 2.3)\,\mu\text{s}$.

Finally, in order to determine the inductance, L, of the cylinder the resonant frequencies, $f_{\text{res}}(C)$, of a parallel *LC* circuit for various known capacitances, C, were measured with a network analyzer (Mini Radio Solutions miniVNA). Fig. 3.8 shows a plot of ${f_{\text{res}}}^2$ against $1/C$, and using the relation ${f_{\text{res}}}^2 = 1/(4\pi^2 LC)$, a value for the inductance of $(0.49 \pm 0.05)\,\mu\text{H}$ is extracted from the gradient of the linear fit.

3.6 Experimental system

The architecture of nearly all cold-atom research-based experimental systems is very similar and well established. We can subdivide experimental systems into three sub-systems connected by overall purpose: a vacuum chamber consisting of multiple components for the production and maintaining of ultra-high vacuum (UHV) conditions; an optical bench for the preparation of many laser beams with precise frequencies, polarization and power; and finally structures to generate magnetic, electrical and/or radio frequency fields. Supplementary to all of this are supporting electronics racks and computer-based control systems.

As we aimed only test the cylinder trap against the requirements listed in Sec. 3.2, we opted to build a relatively simple experiment with well understood equipment to limit the number of potential variables and hurdles. Where possible, newer models or techniques were used with the general motivation being to reduce the overall experiment volume and/or simplify the construction.

3.6.1 Vacuum system

The presence of undesirable atoms, molecules and particulates has a critically limiting effect on the production of a MOT, magnetically trapped clouds or BECs. Typically experiments are thus housed in vacuum chambers where the volume can be evacuated, providing an almost-empty space for the experiment to be carried out. All equipment, including the enclosing structures themselves, must also not outgas, that is emit particles, and should provide a sufficient diffusive barrier that particles cannot desorb through the material from air into the vacuum. Other than the cylinder trap itself which as of yet is an unknown, all the vacuum housing and equipment used to 'pump-down' (the process of evacuating the vacuum chamber) are chosen as they are well established materials or processes for these purposes.

The cylinder trap was contained within a standard spherical octagon vacuum chamber [Kimball Physics, MCF600-SphOct-F2C8] (See Fig 3.9(a)) with optical access windows (two CF100 (100 mm diameter) and eight CF40 ports) which aligned to the same common cartesian axis that the cylinder was designed against. All vacuum sealing surfaces are selected to be con-flat (CF) knife-edge sealing types, having good UHV performance with the flexibility of being removed easily unlike, for example, indium sealing. CF type sealing make use of copper, or silver plated, gaskets into which each of the two connecting components cuts into with a circular knife-edge and held tight with bolts, forming a physical barrier to stop leaks. The additional access ports not used for optical access are connected to vacuum measurement devices (Fig 3.9(g)), vacuum pumps (Fig 3.9(a-c)) or sealed with a blank flange. A CAD render of the system, is shown in Fig. 3.9 where optical equipment for lasers is omitted for sake of clarity.

Prior to installation all vacuum equipment, and anything to be installed within the vacuum, is 'UHV-cleaned' to remove dirt and, critically, residual oils from manufacture and handling. This process is carried out in a clean-room environment where components are submerged into an ultrasonic bath multiple times in various liquids, each time removing residual contaminants which would harm the vacuum. Whilst exact procedures depend on the component materials and how fragile it is, the overall process goes as follows; a warm soapy water bath removes most residual oils and rough particulates and is then rinsed with deionized water to avoid further mineral deposits; a bath of just deionized water to dissolve any leftover soap; a second rinse with deionized water; finally a bath of acetone, ethanol or methanol, depending on the material, breaks down and removes any persistent contaminants. Components are air dried in a filtered-air environment and wrapped in oil-free foil for storage.

Removal of extraneous atmospheric particles once the vacuum is sealed is carried out through a staged series of vacuum pumps[4]. The first of which, not shown in Fig. 3.9, is commonly a diaphragm pump [ours, Pfeiffer Vacuum MVP 040-2] which takes our small system from

[4]The specific details of vacuum pumping is not in the scope of this work, however a reasonable reference can be found in [135]

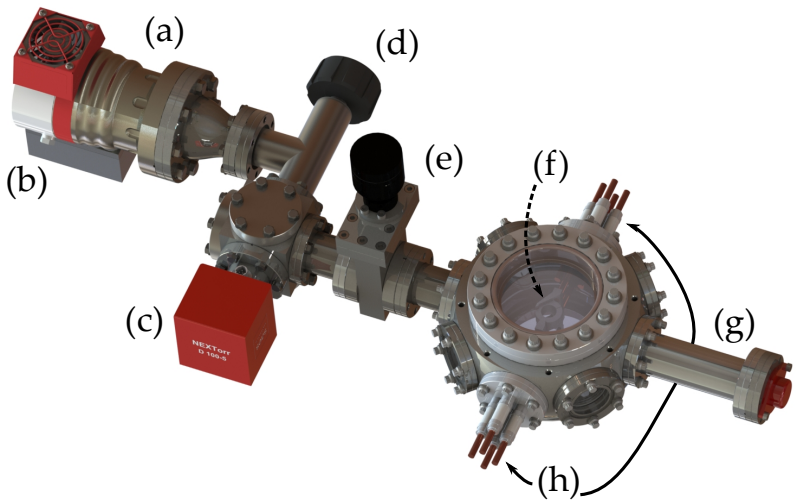

Fig. 3.9 Rendered image of our vacuum system. (a) Turbo-molecular pump. (b) Flange for roughing pump connection. (c) SAES Getter pump. (d) Angle valve, closes pathway to (a). (e) Gate valve to seal (c) away from main chamber in case of outgassing. (f) Cylinder trap housed within main chamber. (g) Vacuum gauge. (h) Two four-pin vacuum feedthroughs.

atmospheric pressures, 1×10^{-5} mbar to roughly millibar pressures at which point the fluid-like flow of particles transitions to a projectile-like motion, where the pump ceases to work efficiently. Equally one can consider this a transition in regards to the particle mean-free path, going from several nanometers to one on the order of several meters. A turbo-molecular pump (turbo-pump, for short) [Pfeiffer Vacuum, HiPace 80] is then activated which makes use of specially oriented high RPM (1500 Hz) fan blades which preferentially redirect colliding atoms out of the system. In very clean systems it is possible to achieve around 10^{-9} mbar pressures with just the turbo and diaphragm pump combination.

After the initial room temperature pumping, which typically takes only 1-2 hours depending on the system size, is it common to then bake-out the entire system at a high temperature. The main aim of which is to desorb material from all the internal surfaces of the vacuum system, while the secondary aim is to induce suffusion of sub-surface trapped gases throughout the material. In either aim, particles are to be removed via the turbo process and are both generally more efficient the higher the temperature is allowed to go, up to the limit of melting structures. The practical limiting upper temperature is most often optical viewports whose optical coatings generally are limited to up to around $180 - 200\,^{\circ}$C. In our case the 3D printed structure had to also be considered, see Sec. 3.3, luckily for the cylinder trap this was roughly the same limiting temperature as the viewports. Once the total system temperature is raised gradually to avoid mechanical strain from thermal gradients, to a steady 190°C, the system is kept there for several weeks. The ideal length of time is somewhat uncertain. Two weeks is a general guide but this is mostly a function of experimental demands and time constraints. Based on the empirical work done on similar systems, a bake-out of up to a month is more than adequate. However if the system has a lower limiting temperature or is physically much larger, one could envision a bake-out of several months to achieve a good vacuum environment.

The final stages of pumping to achieve what we now call ultra-high vacuum (UHV), or roughly $< 10^{-10}$ mbar is mostly commonly reached through a combination of active ionization techniques

and passive adsorption materials. An ion pump element ionizes the residual gases within the vacuum system, which are then accelerated towards a cathode and either sputter cathode material, generating a sticky surface (a getter) for particles to adhere to, or the ions themselves are buried deep within the cathode. In most systems a secondary additional passive getter pump is used to supplement the ion pump. Over the last few decades it has been common to see titanium sublimation pumps in experiments, which use a titanium emitter to coat the internal surfaces of a large (roughly one meter) cylinder for unwanted gases to adhere to. In our system we used a next-generation device which combines a small ion-pump element with a large surface area sponge-like getter material in a device on the scale of tens of centimeters [Saes NEXTorr D 100-5]. The combination of the two elements is sufficient enough to require only this one device, rather than two separate components. This also aligns with our aim to reduce the required experimental size and power consumption for such systems.

The NEXTorr device is kept in a hot-mode up to this stage of the bake-out, having been switched on once the steady-state system temperature had been reached. This avoids gradual contamination where particulates are retained rather than letting them be flushed out by the turbo. Prior to full activation of the NEXTorr getter element, we first must activate the rubidium dispensers. Alkali metal dispensers [ours, SAES Rb flat-terminal-type] consist of between $4-9\,\mathrm{mg}$ of active metal suspended in a reducing agent and sealed with a so-called activation layer to protect the dispenser from air contamination which can cause sudden and destructive oxidization. Once housed in the vacuum chamber and at around $10\times10^{-8}\,\mathrm{mbar}$ during the peak chamber temperature, the activation layer is removed with a high-current and diffuses through the turbo. This process is highly contaminating to the ion and getter pump, and so must be carried out before any pump activation so the residual particles are removed. The current standard for such dispensers are non-ideal for small and portable systems due to their low material capacity, as the reducing agent is required, and high running temperatures can cause emissions of unwanted species. For our purpose it was sufficient, however we direct the reader to [79, 136, 137] for consideration.

In a similar process, the NEXTorr getter and ion elements are then activated by passing a high current to rapidly boil off particles. There is an issue hidden here, the getter/ion activation could also contaminate the now-exposed dispenser element. To mitigate this we mounted our dispensers onto the un-used pins of the feedthroughs, see Fig 3.9(h) which are 'upstream' to the diffusive flow of particles from the main chamber, to the NEXTorr and then out toward the turbo pump. After this final activation the system is closed with the angle valve and cooled down to room temperature, the background pressure rapidly drops to the desired $<10^{-10}\,\mathrm{mbar}$ as a result. Unfortunately in our initial experimental system the vacuum gauge to measure the pressure more precisely failed, and so we could only achieve this upper-bound reading from the NEXTorr device. The pressure achieved was believed to be sufficient for the production of a MOT, but perhaps not adequate for a long-lifetime magnetic trap.

3.6.2 Laser and optical system

Laser frequencies

The keystone of atomic physics experiments, and measurements making use of atomic species, is the homogenous behavior of specific isotopes of atoms independent of the exact location and time at

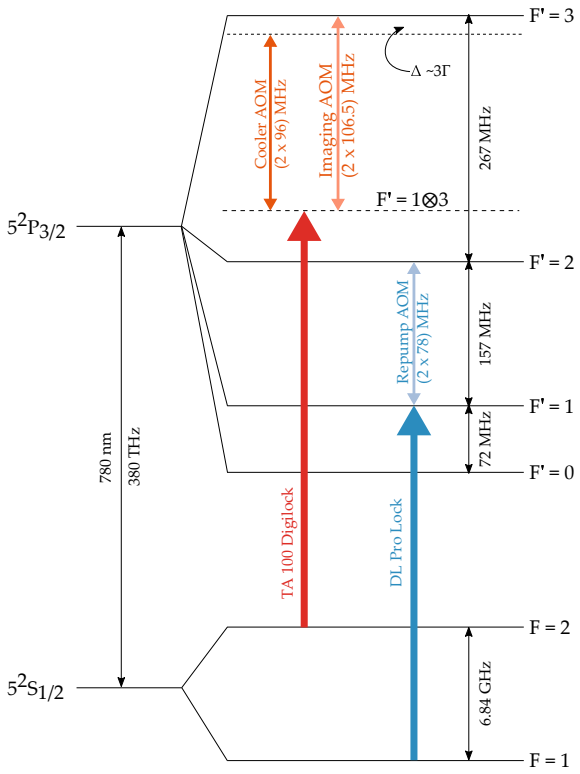

Fig. 3.10 Transitions of the D_2 line of ^{87}Rb [103]. A TA100 Pro laser, which is stabilized using a Toptica Digilock module to the $|F = 2\rangle \rightarrow |F' = 1 \otimes 3\rangle$ transition, provides the base-frequency with which AOMs shift to the main (red detuned $\Delta \sim 3\Gamma$) cooling and (on resonance) imaging transition $|F = 2\rangle \rightarrow |F' = 3\rangle$. The repumping transition $|F = 1\rangle \rightarrow |F' = 2\rangle$ is provided by the combination of a DLC Pro, which is locked independently from the TA100 with its own in-built locking module to $|F = 1\rangle \rightarrow |F' = 1\rangle$ line, and then shifted with an AOM.

which tests are carried out. The cost for experimentalists however is that in order to probe, measure and make-use of such fundamental quanta requires the use of precise, coherent and stable laser with which to address them; the result being that laser systems have become the backbone of ultracold atom experiments [138]. For the purpose of laser cooling ^{87}Rb there exists an adequate cycling transition, also called the cooling transition [103], on the D_2 line at 780 nm, which is shown in Fig. 3.10. This is conveniently accessible through now readily available [139] semiconductor diode lasers, which were originally popularized through their availability in common household items like CD and DVD players. In reference to Fig. 3.10, in order to individually address the hyperfine levels of the D_2 line, which has a natural linewidth of $\Gamma \approx 2\pi \cdot 6\,\text{MHz}$, we would require a laser linewidth on the order of $\approx 2\pi \cdot 1\,\text{MHz}$. To this aim the raw output of the diode laser, with linewidths of several tens of megaHertz in the regime of higher power lasers [140, 141], are typically coupled into an external cavity, narrowing the linewidth to below 1 MHz [142, 143, 139].

In practice a single laser frequency is not sufficient for a cold atom experiment as multiple transitions, both desired and not, must be used; in Fig. 3.10 we show the full range of transitions used for the cylinder trap experiment. The main cooling transition on the D_2 line is the $|5^2S_{1/2}, F = 2\rangle \rightarrow |5^2P_{3/2} F' = 3\rangle$, which as discussed in Chp. 2 is typically red-detuned from resonance by $\Delta \sim 3\Gamma$. This is provided by a Toptica TA100, whose initial seed power of $\sim 40\,\text{mW}$ is boosted with a tapered amplifier chip to powers up to 3 W. Whilst this power (density) is much greater than the

saturation intensity of ^{87}Rb ($I_{sat} \approx 1.67\,\mathrm{mWcm^{-2}}$, where laser beam size is on order of 2 mm), significant losses occur in the preparation of the laser light.

The laser powers involved mean there is a finite excitation probability on the $\left|5^2S_{1/2}, \mathrm{F}=2\right\rangle \rightarrow \left|5^2P_{3/2}\mathrm{F'}=2\right\rangle$ transition. Once here atoms may then decay down to the $\left|5^2S_{1/2}\mathrm{F}=1\right\rangle$ ground state, where they will accumulate as the 6.8 GHz energy gap inhibits excitations. To combat this, a small fraction of the light is diverted for a 'repumping' laser. This is provided by a Toptica DLC Pro outputting up to 100 mW, which couples the $\left|5^2S_{1/2}, \mathrm{F}=1\right\rangle \rightarrow \left|5^2P_{3/2}\mathrm{F'}=2\right\rangle$ transition, allowing atoms to then spontaneously decay back into the cooling transition cycle.

Fine adjustment of the frequencies are made through implementation of acousto-optical modulators (AOMs) along each (cooling, repumping and imaging) laser line, which also provide control over laser power and fast switching ($\sim 10\,\mu$s). AOMs [144] make use of piezoelectric components to induce acoustic (radio-frequency) wavefronts within an optically transparent crystal. Some of the light is scattered through the crystal and in turn absorbs (or destroys) a discreet quanta of phonons, given by the conservation of momentum, and thus affect the final photon frequency. A user controlled input RF frequency allows for precise control of the impinging radio-frequency of the crystal and so provides a tool to tune the laser frequency with the precision of 1 MHz; while by control of the signal amplitude one also gains a way to control the beam power and in tune also a method to 'switch off' the incident light. This switching is not perfect however, and slower mechanical shutters are required to completely extinguish the beam. In our system we implement a double-pass AOM configuration [144–146], which accounts for the dependence on the diffraction angle on the modulation frequency input into the AOM. At the expense of the additional beam power losses on the second pass, this scheme allows for the output frequency of the AOM to be varied without having to re-align and optimize the optical path, as the net angular refraction of the beam is zero. The incident light and the input RF signal both have a heating effect on the crystal and AOM casing which can alter the overall efficiency and performance, to account for this all of our AOMS are left on 'hot mode', i.e. their input signals are continuously running during experimental runs to avoid the sudden thermal shock that is associated with the switching on or off the impinging light or RF signal.

Laser stabilization

The presence of experimental noise is most obvious in its effects on the laser systems used within cold atom experiments, seen both through direct stability tests on laser power, frequency and polarization but also in the secondary effects this has on the trapped atoms. Most commonly observed in atom number variations, spatial oscillations of the cloud's center of mass or in the worst cases in the destruction of the cloud itself. Noise and experimental drift must be mitigated and accounted for by experimenters.

Optics, including source lasers, are placed on large (meter long) optical tables, which themselves are 'floating' on gas-damped supports, which in turn are often placed on isolated foundations to minimize vibrational noise from and around the building. Where possible the bulk of the optics and laser setup are housed within matt black (to avoid strong back-reflections) containment boxes, which provide some thermal isolation, but more critically avoid vibrations and dust transmitted through air. Precision air conditioning units controlling both ambient temperature and humidity

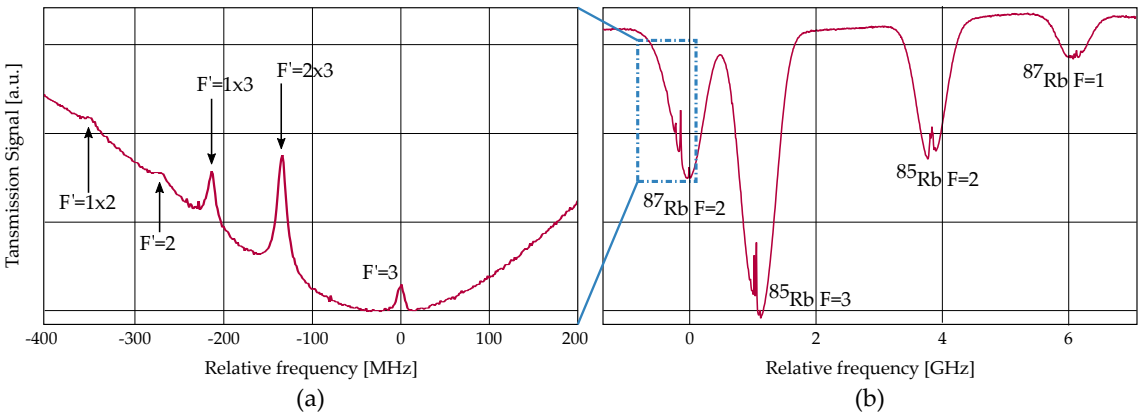

Fig. 3.11 Absorption spectroscopy signal of the D_2 line of ^{87}Rb obtained across a ^{87}Rb enhanced Rb vapor cell(a) Shows the zoomed-in spectrum for the $\left|5^2S_{1/2}, \mathrm{F}=2\right\rangle \rightarrow \left|5^2P_{3/2}\mathrm{F'}=?\right\rangle$ transitions. (b) A wider view showing the Doppler valleys and some hyperfine transition peaks for both ^{87}Rb and ^{85}Rb lines. Note the change in units for the frequency axis.

are common-place to avoid periodic drifts of temperature causing correlated mechanical drifts in optomechanics, e.g. mirror mounts, as well as protecting lasers from condensation forming on their critical components. The flow of air from these units is designed to be laminar and filtered, again to minimize dust and vibrations, however this still can cause disruption on the optical components, and so the isolation box also protects from direct air flow. Finally, electronics are installed in bespoke circuits to avoid ground loops forming, where noise and equipment signals can be transmitted into other more sensitive elements.

Despite the above preparations it is still necessary to provide active stabilization of the laser frequency to compensate for both slow (minutes to hours) drifts in temperature and faster (sub-second) oscillations from electronics, commonly referred to as 'laser-locking'. A laser reference is created for this purpose through Doppler-free absorption spectroscopy [147] which provides a method to resolve the hyperfine transitions of the D_2 line of ^{87}Rb [98, 99].

An example spectroscopy signal can be seen in Fig 3.11. As per the commonly described system setup [148, 99], this figure is obtained by passing a dithered (several MHz) *pump* beam through a ^{87}Rb enhanced vapor cell (not necessary, but makes the ^{87}Rb much stronger than the more abundant ^{85}Rb isotope) with an intensity on the order of $I_{pump} \geq I_{sat}$, where I_{sat} is the saturation intensity of the transition in question. In this regime one must consider both the inhomogeneous effect of the Doppler-broadening of atoms, due to their variation in velocity (equivalently, temperature) as given by the Boltzmann distribution, and the homogeneous broadening from spontaneous emission [99]. The combination of the two creates an absorption profile which is a convolution of a broad Doppler profile with a velocity-dependent selective delta-like function (in the limit of low temperatures); the latter which burns a hole into the profile which corresponds to an identical peak in population of the excited level. The power broadened width of this hole is given by $\Gamma' = \Gamma\sqrt{1+(I/I_{sat})}$ [149]. When a secondary counterpropagating beam is included, the *probe* beam, of exactly the same frequency but generally of much lower intensity, $I_{probe} \ll I_{sat}$, and then overlapped near resonance a narrow (up to limit of the natural linewidth Γ) transmission line through the sample is observed. These can be readily seen in Fig 3.11(a) with peaks labelled F' = 3 and F' = 2. Crossover peaks, denoted in

the form in Fig 3.11(a) as $|\mathrm{F}=2\rangle \rightarrow |\mathrm{F'}=n\otimes p\rangle$, result when the swept laser frequencies match exactly halfway between pairs of excited state levels. [5]

In order to lock our lasers we make use of the signal generated as in Fig 3.11(a) to carry out modulation spectroscopy [150]. The laser frequency is modulated and passed through a lock-in amplifier to generate an error signal, also known as a derivative signal, which can then be passed onto a proportional-integral-derivative (PID) controller to lock the laser frequency to the desired reference transition.

Our experimental setup made use of two individual laser outputs, each requiring their own reference cell for locking. The repumper laser is locked via an internally installed Toptica DL Pro Locking module as part of the DLC Pro Digital Controller. The repumping transition is $|\mathrm{F}=1\rangle \rightarrow |\mathrm{F'}=2\rangle$ line, however it is experimentally more convenient to lock the laser to the reference signal of the $|\mathrm{F}=1\rangle \rightarrow |\mathrm{F'}=1\rangle$ transition as the peak is marginally more resolvable by the locking software. We then shift the signal via the double-pass AOM system by $2\times 78\,\mathrm{MHz}$, which also allows us some freedom to adjust the frequency and power using the AOM control parameters, as already discussed. The cooling transition is, for similar reasons, locked to the prominent crossover peak $|\mathrm{F}=2\rangle \rightarrow |\mathrm{F'}=1\otimes 3\rangle$. We achieve locking of the TA100 laser via a Toptica Digilock Module [SC110] installed into the same rack as the main laser control unit, which provides its own separate control software and control over various PID settings. The locked reference laser is split across two AOM lines; one is red detuned for the cooling transition ($\Delta\sim 3\Gamma$) to the $|\mathrm{F}=2\rangle \rightarrow |\mathrm{F'}=3\rangle$ via a double-passed AOM set up $2\times 96\,\mathrm{MHz}$. The second is shifted again by a double pass AOM by $2\times 106\,\mathrm{MHz}$ to be on resonance with the same transition for use as the imaging beam.

Optics distribution

The preparation of the laser light for use in our experiment was carried out in a contained region of the optical bench, where the only inputs were power and control signals to the laser 'heads', AOMs, mechanical shutters and photodiodes; while its only output is a select number of optical fiber cables which pass on toward the vacuum system. This in effect created a literal black box where optically prepared laser light would output. There were a number of experimental motivations behind this: the stability of the laser beams in regard to thermal and airborne vibration noise; the freedom to position the laser system away from or even in a separate lab to the vacuum system; and the safety of users of the system. However in regards to the miniaturization of whole experimental systems this modular approach would allow for any compact source of laser light to replace the whole optical system, which is a stable requirement for any ultracold atom device [85].

The distribution of our laser setup can be seen in Fig 3.12; the two 'laser heads', one each for the TA 100 and the DL Pro, TA and DL for short, are shown in different colors which do not correspond to the actual laser emission color. Both have front outputs which are immediately controlled by a mechanical safety shutter, whilst the TA has an additional back output which we use for the cooler transition absorption spectroscopy reference. Across the whole distribution polarizing beam splitters (PBS) are paired with half waveplates ($\mathrm{L}/2$) to control the power distribution between

[5] We have made a point here to avoid calling this process 'saturated absorption spectroscopy', as this has been shown in [149] to be a misnomer as one must consider hyperfine pumping resulting from multiple ground states in a non-equilibrium regime to fully model the transmission profile.

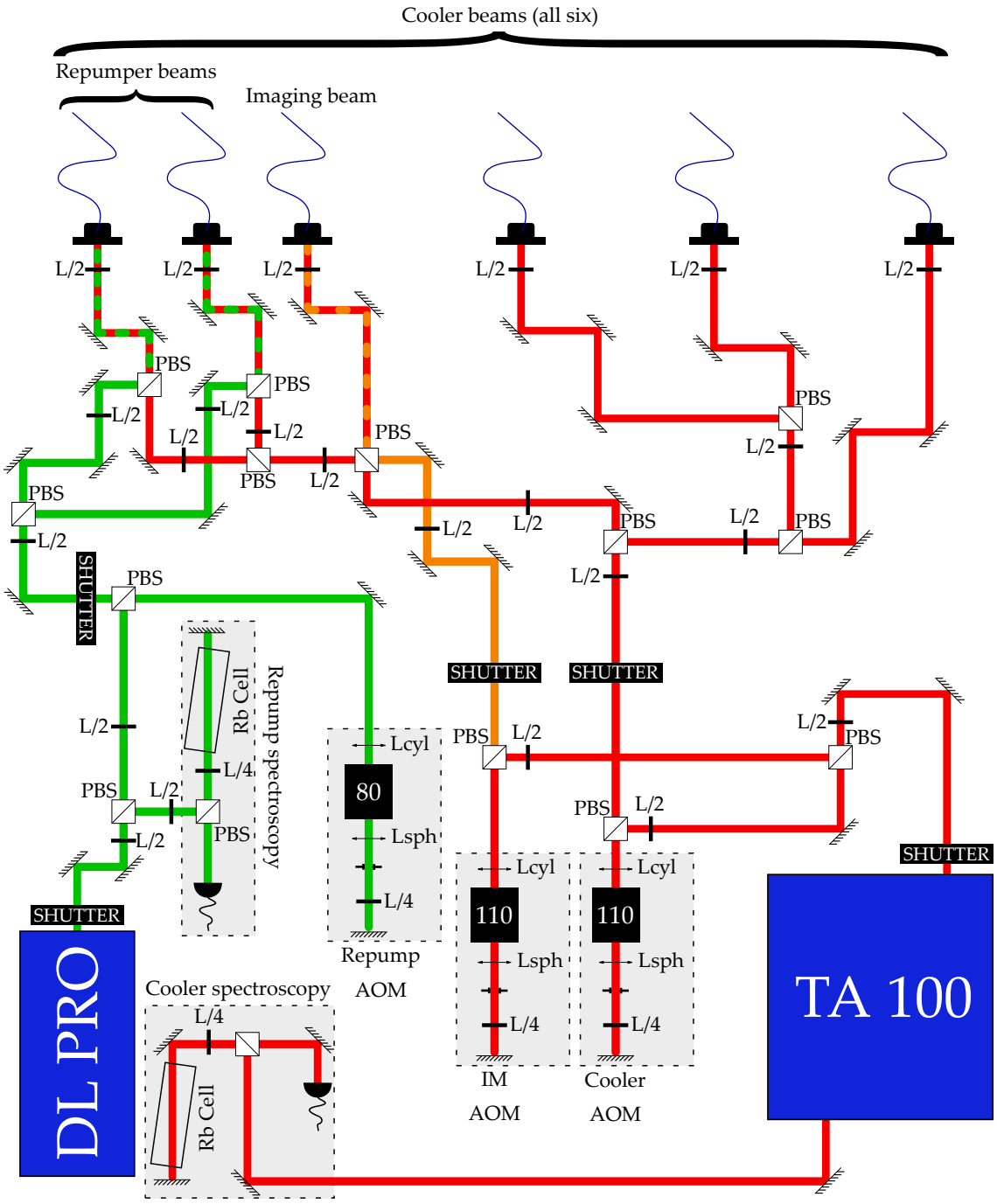

Fig. 3.12 Schematic of optical system used in the cylinder trap experiments. The three colors correspond to the three laser transitions of light used, and not to the actual laser color; green is the repumper, orange the imaging light and red the cooler. Dashed regions show where light is overlapped.

laser paths. As cold atom systems are particularly sensitive to both relative laser powers between counterpropagating beams, as well as laser polarization, particular care was taken to ensure all but the desired polarization was completely extinguished; this was done through various beam blockers (not shown) and by adjusting the angle of incidence for all components until a stable, definite polarization was fixed. AOM lines for each of the desired transitions can be seen with a number of cylindrical and spherical lenses (L_{cyl} and L_{sph} respectively) which ensure more efficient transfer of energy between the AOM phonons and the light by shaping the beam to match the crystal shape. On the each pass of each AOM, a quarter waveplate ($L/4$) is encountered forcing the now frequency adjusted light into a different path away from its original source pathway. Further PBS/waveplate combinations then equally divide, with respect to laser power, the beams for fiber coupling.

In our system we are limited in the number of optical input vectors as the cylinder trap itself blocks some routes, such that there are only six possible inputs to the vacuum system. This means that the total of nine beams, six for the three counterpropagating pairs of cooler light, two for a pair of counterpropagating repumper beams and a final imaging beam, must be overlapped where required. To achieve this, the linear light polarization for each input is specifically selected to align to either the fast or slow axis of the optical fibers, with particular care to then how this is then used on the vacuum side. As the PBS are significantly more robust for the transmission of light rather than reflection, the more critical cooler light is selected for transmission through a PBS on its final path leg and then be matched to the fast axis of the fibers with a half waveplate. The repumper and imaging beams are aligned, individually, for reflection into several of these PBS such that they are overlapping with the cooler light, and as a result align to the slow axis of the fiber once they have passed through the same half waveplate.

Using fiber optics provides a final stage of polarization and optical-mode cleaning, in the latter case meaning the final output is an almost perfect TEM_{00} laser mode. However misalignment into the fiber, or poorly aligned optical components earlier in the optical path, transmit directly into the final output polarization quality and stability. This is particularly apparent when the fiber undergoes thermal changes or mechanical stress, which is advantageous as a tool to measure the amount of misalignment if done intentionally. As a rule of thumb we work with a less than 5% polarization variation, when fibers are purposely deformed/heated, in addition to insulating fibers to mitigate ambient temperature changes and avoid sharp bends along the fiber line.

Vacuum-side light preparation

With the six optical fibers pathed toward the vacuum system, it is necessary to have out-couplers to take the highly divergent light output from the fiber ends and shape, correctly polarize and trim it to match the desired laser field required in the magnetic field region. This is carried out using so-called 'MOT guns', the basic components of which are shown in Fig. 3.13. Light, which may contain two perpendicular linear polarizations, outputs from an optical fiber of numerical aperture NA $= 0.12$ and core diameter of $4.5\,\mu m$[6] diverges strongly. It first is incident onto an quarter waveplate which transforms the linear into circularly polarized light with a handedness determined by the relative angle of the waveplate fast/slow axis to the fiber output; the required handedness is determined by

[6]Thorlabs: Polarization maintaining single-mode optical fiber PM780-HP type, with jacket FT061PS.

the relative alignment of the beam to the magnetic quadrupole axes. Secondary beams coupled into the same fiber along the other fiber axis will pick up opposite handedness.

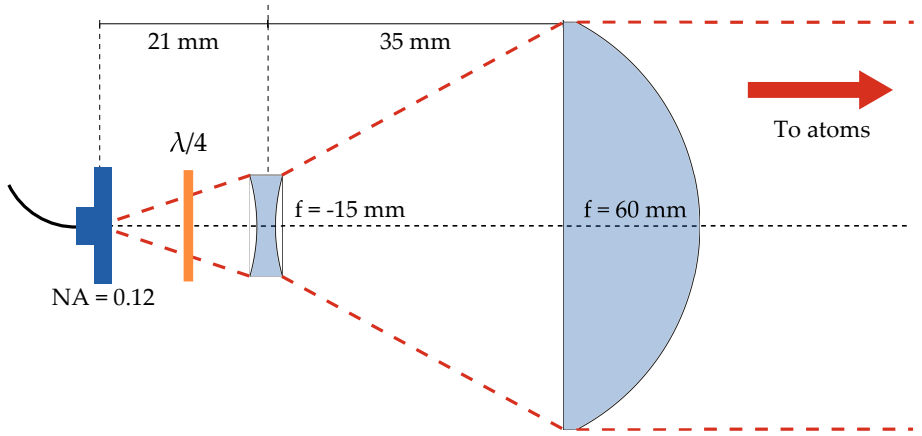

Fig. 3.13 Main components of a 'MOT gun': Highly divergent linearly polarized light from an optical fiber is pass through a quarter waveplate to create circular polarization and then shaped such that it is collimated to a specific beam diameter.

The combination of specifically chosen biconcave [LD2060-B – N-SF11] diverging and plano-convex [LA1401-B – N-BK7] lenses then shapes the beam output to a final $1/e^2$ diameter of around 50 mm[7]. The initial biconcave lens is in principle not necessary, however it further diverges the initial beam output so it reaches the correct diameter in a shorter length, reducing the MOT gun size. Five of the six MOT guns follow this schematic, with the six having the waveplate omitted due to the imaging setup we used to measure our atoms, as explained in the imaging section following. An additional iris is included in all the MOT guns so the beam diameter can be truncated. In regards to the cooling light specifically, the raw output of the MOT gun is a $1/e^2$ diameter of 50 mm with an actual per-beam power of 8 mW and peak intensity of 4 mWcm^{-2}, corresponding to $I_{beam} \sim 0.5 I_{sat}$.

3.6.3 Imaging system

The development of atomic systems has accordingly pushed the development of quantifiable methods to extract information about the trapped atoms, typically with destructive absorption imaging or non-destructive dispersive techniques [151]. In this work we make use of the former method, absorption imaging [152] in which a probe beam is passed through a cloud that expands for some time after its trapping potential has been switched off adiabatically. The length of this expansion time determines the extractable information imprinted onto the imaged atomic density, whose negative 'shadow' is imaged on a camera. Clouds imaged at short times, almost immediately after the potential is switched off, still retain the form of the potential and often will completely absorb the incident light around the central region of the cloud. For longer expansion times the momentum space distribution dominates as the cloud shape becomes Gaussian in the case of thermal atoms; analysis of such images allows for atom numbers, atomic cloud dimensions and temperatures to be readily evaluated over multiple experimental runs.

[7] See appendix for methodology and optimization procedure for optics systems used

Imaging optics

The probe beam, also called the imaging beam, is provided as part of the TA 100 laser line which also serves the cooling transition. Picking off a relatively small amount of power (several miniWatts), the light is passed through a dedicated AOM line to shift the locked laser light across the transition $|\mathrm{F'} = 1 \otimes 3\rangle \rightarrow |\mathrm{F'} = 3\rangle$ such that it is on resonance. This light is then overlapped with one of the cooler beams, shown in Fig. 3.12, and then coupled into the optical fiber such that its linear polarization is perpendicular to that of the cooler light. Imaging occurs at the end of a typical measurement sequence and must occur whilst the MOT beams are off so not to saturate the camera; while the fiber is oriented to accept both cooler and imaging light, in practice this means only one beam is present at any one time. The imaging light goes on through a MOT gun as per Sec. 3.6.2, and then follows the trajectory as shown in Fig 3.14, picking up circular polarization with the internally mounted quarter waveplate.

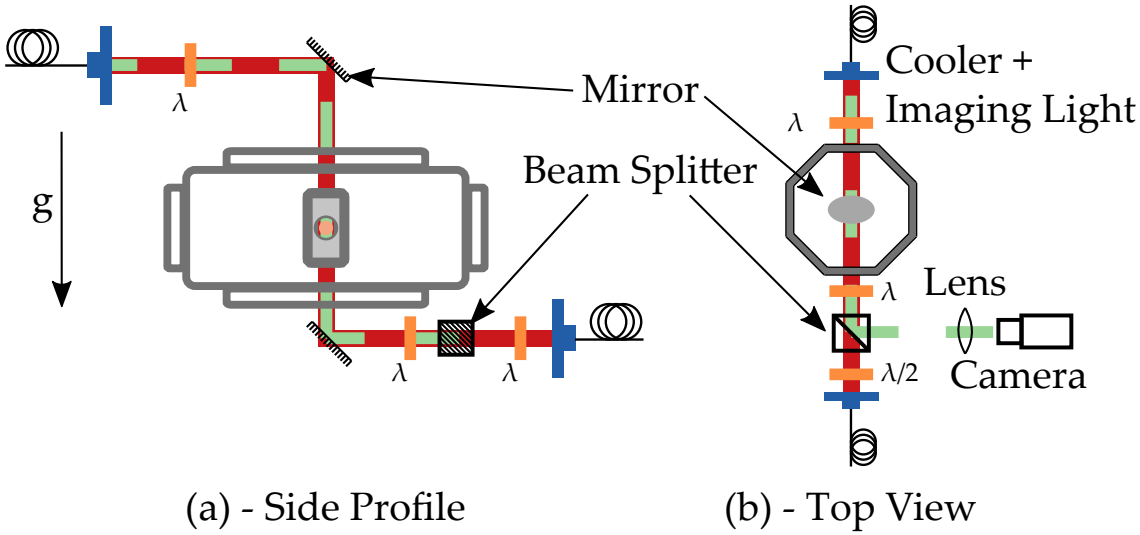

Fig. 3.14 Schematic of the imaging system path within the cylinder trap experiment. Red shows the cooler light, whilst the dashed green shows the imaging beam path. The imaging beam is overlapped with the cooler, and picked off after interaction with the cloud by a beam-splitter quarter waveplate pair.

The 15 mm aperture of the cylinder trap sets a limit on the amount of time a cloud atoms would be visible in the field of view of the imaging beam and camera, with a rough estimate of the edge of the cloud passing by the aperture within $30 - 40$ ms. The effective measurement window would likely be even shorter due to scattering off the cylinder surface causing disruptive effects on the final image. We chose instead to measure vertically, i.e. along the gravity axis, such that the atoms would appear to fall into the cameras view. The path taken by the imaging beam is shown in the side and top-view profiles of Fig. 3.14. As the imaging light is of a different circular polarization with respect to the cooler, we can pick it off after interaction with the atoms by passing it through another quarter waveplate, which makes it linear, and optimize it for reflection through a beamsplitter to then be passed onto our camera. This same quarter waveplate provides the correct polarization to the cooling light emitted from the lower MOT gun in Fig. 3.14(a), so no waveplate is included within this MOT gun. Our imaging camera is a Imaging Source DMK 23U445 CCD (charged-couple device), with square pixels $3.75 \times 3.75\,\mu$m distributed across a

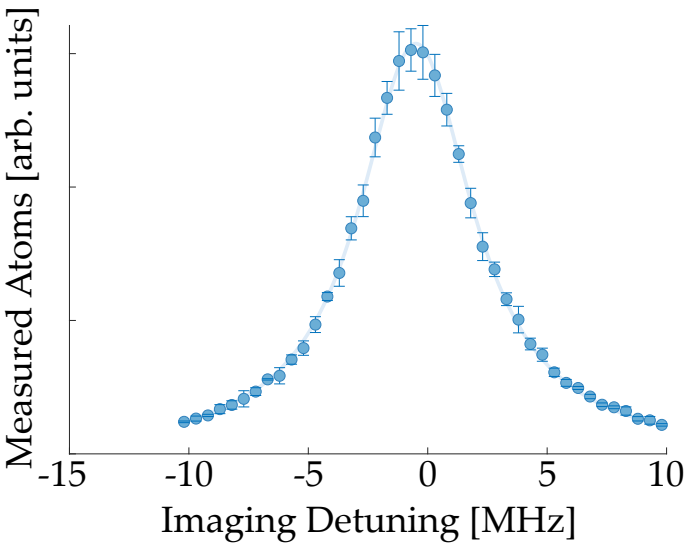

Fig. 3.15 The response of the atom number as the frequency the imaging light is shifted with the AOM. A Lorentzian fit is carried out and has a peak at zero, confirming our laser is at the correct expected lock point. Data for image used with permission from T. James and A. Gadge, University of Sussex.

Sony ICX445ALA sensor chip, providing a 1280×960 (1.2 MP) resolution. The beam itself had an initial total power of 2.5 mW distributed over the Gaussian profile of $1/e^2$ diameter of 50 mm, providing a peak intensity of $I_0 \approx 0.1 I_{sat}$. The lens distribution is set up in the afocal regime with a total *demagnification* of 0.5 such that even large clouds fit into the chip. The maximum resolution is set by the Raleigh criterion where $r_{max} = 1.22\lambda f/D$, where λ is the wavelength of the light, and f and D the focal length and diameter of the first lens, respectively. However the actual resolution is unlikely to approach this; clipping from the cylinder trap aperture and vacuum viewports limits the solid angle of capturable emitted light, which is further diminished as the first lens cannot be any closer than the reflection surface of the beam splitter in Fig. 3.14. An estimate of the actual resolution is achieved through imaging of a standard resolution target [8] in a test setup, which we measured to give a 56 µm resolution for our system.

An example of the response of the atoms to a frequency sweep of the imaging beam is shown in Fig. 3.15, which shows a clear Lorentzian profile. The width of this is a combination of the natural linewidth of ^{87}Rb (6.1 MHz) with the linewidth of our incident laser (< 1 MHz).

Absorption imaging

Our experimentally accessible information is the intensity of a two-dimensional projection of a cloud onto the surface of a CCD camera, which itself is made up of a finite number of pixels with a specific size. In order to extract properties of our cloud we must then first understand how light propagates and is absorbed through the cloud itself, and how the remaining light is then measured by the camera.

For the purpose of this discussion we use an on-resonant beam of low intensity $I_{in} \ll I_{sat}$ light passing through the cloud. In the $\Delta = 0$ approximation, the atoms do not impart any phase shift on the light as it moves through the cloud, and we need only consider the attenuation of the light

[8] We use a Thorlabs R2L2S1P1 High-Frequency NBS 1963A Resolution Test Targets, 2" x 2"

intensity. This allows for a simple formulation of the scattering cross section of the atoms, as follows $\sigma_0 = 3\lambda^2/2\pi$ [99]. According to the Beer-Lambert law we may then write the transmission of the imaging light, or probe beam, along the imaging axis z through the atomic cloud as [153, 154],

$$\frac{\mathrm{d}I}{\mathrm{d}z} = -n_{3D}(x,y,z)\sigma_0 I, \tag{3.1}$$

where I is the light intensity and $n_{3D}(x,y,z)$ is the three-dimensional density of the cloud. By integrating Eq. 3.1 along z and solving for the atomic density one gets,

$$n_{2D}(x,y) = -\frac{1}{\sigma_0}\ln\left(\frac{I_{in}(x,y)}{I_{out}(x,y)}\right). \tag{3.2}$$

This defines the column density $n_{2D}(x,y)$,

$$n_{2D}(x,y) = \int_{cloud\ size} n_{3D}(x,y,z)\mathrm{d}z. \tag{3.3}$$

We have also defined the optical density $\mathrm{OD}(x,y)$ as

$$\mathrm{OD}(x,y) = n_{2D}(x,y)\sigma_0 = -\ln\left(\frac{I_{in}(x,y)}{I_{out}(x,y)}\right). \tag{3.4}$$

Experimentally we see that the absolute intensity is not required, instead we just need the relative intensities between $I_{in}(x,y)$ and $I_{out}(x,y)$. The full process of the absorption imaging technique is shown in Fig 3.16. We first take an image of the probe beam attenuated through the cloud which has evolved over some given freefall time, giving Fig 3.16(a) and providing an estimate on I_{out}. Fig 3.16(b) is an image of just the probe beam light after the cloud has been allowed to dissipated to a negligible density relative to the background gas, as the cloud does not leave the field of view in our system; this provides I_{in}. Finally a background, or 'dark', image is taken with no probe beam such that other constant sources of stray light can be removed as not to contribute to the final image, giving I_{dark} and Fig 3.16(c). I_{dark} is then subtracted from both I_{in} and I_{dark} to get just the attenuation effect from the cloud.

Our experimentally determined ratios of intensities, with the I_{dark} correction allows for the optical density to be calculated as per Eq. 3.4, however we must take into account the finite pixel size and optical magnification in order to relate this to the atom number. This can be shown to be [100, 155],

$$N = \int n_{2D}(x,y)\mathrm{d}x\mathrm{d}y = \frac{A}{M^2\sigma_0}\sum_{\text{pixels}}\mathrm{OD}(x,y). \tag{3.5}$$

Where A is the pixel area and M is the system magnification. By carrying out a two-dimensional Gaussian fit to the measured optical density, which is given by,

$$\mathrm{OD}(x,y) = \mathrm{OD}(0)\exp\left[-\frac{x^2}{2\sigma_x^2} - \frac{y^2}{2\sigma_y^2}\right], \tag{3.6}$$

one can finally calculate the atom number with,

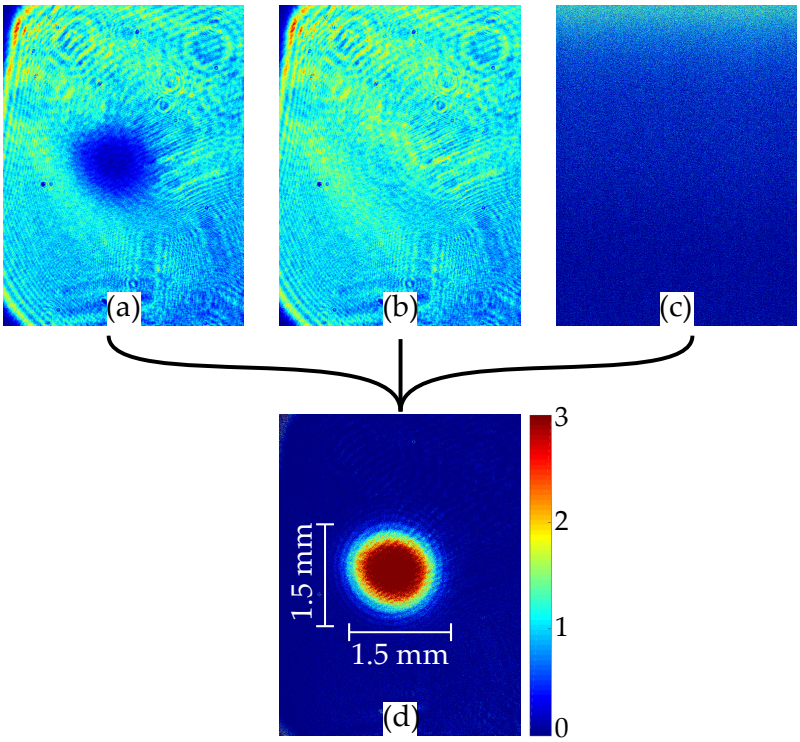

Fig. 3.16 Example absorption imaging process. (a) Raw image of atom cloud shadow taken by camera. (b) Atoms are left to fall out of view and a second light-only image is taken. (c) Light is switched off and a third, final dark image is taken. (d) Imaging processing allows for the atom spatial density to be reconstructed from (a-c).

$$N = \frac{1}{\sigma_0}\frac{A}{M^2} 2\pi\sigma_x\sigma_y \mathrm{OD}(0)\,. \tag{3.7}$$

Where σ_x, σ_y are the clouds two dimensional widths and $\mathrm{OD}(0)$ is the peak optical density, determined from the fitting process. Implicit within Eq. 3.7 is the assumption that the atoms behave as a purely thermal cloud trapped within a harmonic potential, which well describes both a MOT and magnetically trapped atoms [156].

3.6.4 Light-inducted atomic desorption

With the development of portable and compact systems there has been the growing requirement for methods to improve the loading rate and final achieved atom number of atomic vapor traps, both to increase the measurement cycle rate or to improve final signal to noise ratio. However this must be done while not impeding the lifetime of the resultant trap, especially in the regime of background-gas collision losses. Typical methods make use of dual chambers where atoms are pre-cooled and shaped in two-dimensional MOTs in a chamber of high background pressure, and then pushed into a science or measurement chamber via a differential pumping canal which limits diffusion from background gases [157]. Similarly, Zeeman slower style device paired with microfabricated chips connected via differential pumping passages [79] allows for atoms to be pre-cooled from dispensers, or an oven, before moving on to the loading region. These methods show promise but find their limits in the requirement for alkali dispensers to be left on for a

significant fraction of the experimental cycle, and so continually load into the background vapor after the initial trap, or add undesirable experimental volume.

The desire for the total system size to be reduce has pushed some towards single-chamber architectures [78]. To balance the need of high rubidium partial pressure during loading whilst maintaining a relatively low pressure otherwise, light induced atomic desorption, LIAD, has become a leading technique [158–160]. This method makes use of pulses of high-frequency light, typically in the ultra-violet region, to desorb atoms from the internal surfaces of the device during the loading period of the trap. This causes a sharp increase in the rubidium partial pressure as unused Rb which has adhered to the chamber is released, without any increase in dispenser current and so in turn avoids emissions of undesirable particulates or too hot to trap atoms. After loading the LIAD source is switched off during which the background pressure sharply drops, in principle then allowing for a longer lifetime trap. Using a similar system as described in [78] we installed a LIAD system below our main chamber to supplement our dispensers, as well as improve the lifetime of any magnetic traps added later to the design.

3.6.5 Determining MOT temperature

As mentioned in the beginning of Sec. 3.6.3, the projection of the cloud density distribution calculated from absorption imagining is dominated by differing macroscopic properties of the cloud depending on the length of time that has passed since the trapping potential was removed. The relative timescale is determined by the expansion time relative to the original oscillation time in the trap, $t \ll \omega_0$, in the limit where the trapping potentially is removed effectively instantaneously [161]. Assuming an initially Gaussian shape, when $t \ll \omega_0^{-1}$ the imaged density can be considered close approximations of the initial spatial extend of the cloud; in the $t \gg \omega_0^{-1}$ the ballistic expansion of the atoms dominates and the distribution can be used to directly infer the cloud temperature [161–163].

We can formulate the above for a cloud with an initial size $\sigma_i(0)$ and temperature T, then the time evolution of the cloud width σ_i, for $i = x, y$, is given as follows:

$$\sigma_i(t) = \sqrt{\sigma_i(0) + \frac{k_B T}{m} t^2}, \tag{3.8}$$

where for large expansion times, now given as $\frac{k_B T}{m} t^2 \gg \sigma_i(0)$, the initial size can be neglected and one finds,

$$T = \frac{m \sigma_i^2(t)}{k_B t^2}. \tag{3.9}$$

Example plots showing the evolution of $\sigma_i(t)$ in the cylinder trap system are shown in Fig. 3.17. As the imaging process is destructive successive images must be taken of new clouds with identical experimental settings, except for varying the time of flight; each point is an average of five such measurements. These particular measurements are for a cloud with no additional cooling other than that provided by the MOT trapping fields and give a final temperature of $(T_y, T_x) = (170 \pm 30, 180 \pm 10)\,\mu\text{K}$. As the cloud appears to the camera to be normal to the viewing plane, no adjusting of the viewing window had to be made, however there was likely some loss of optical focus as the cloud fell away from the focal point. Without a perpendicular view for comparison, it

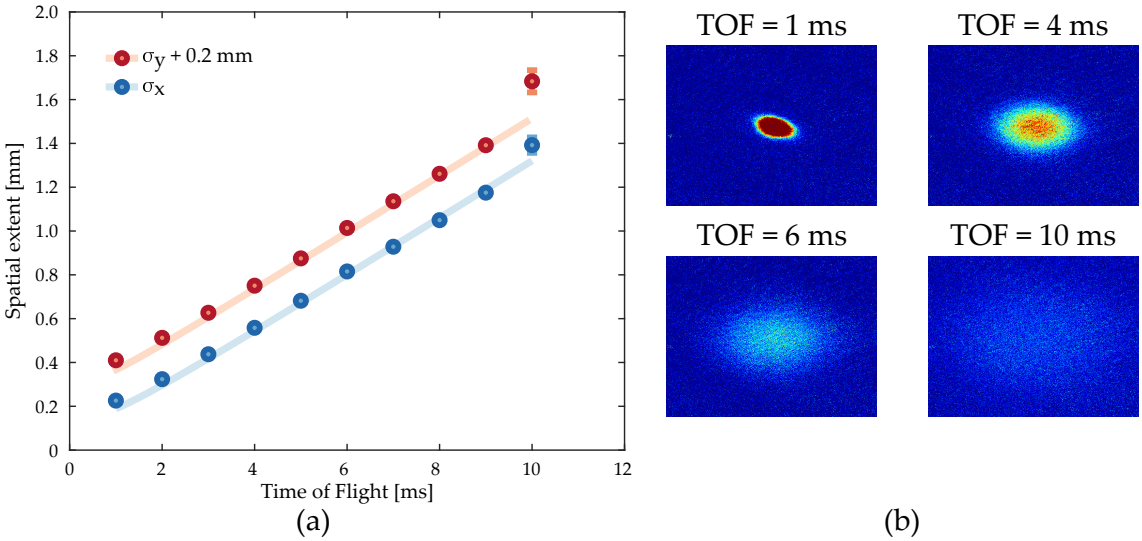

Fig. 3.17 Time of flight measurements used to determine the average MOT temperature for a given set of system parameters. (a) Plots of the measured x and y spatial extents of the cloud. The solid lines show a fit of the data using Eq.3.8. The y data are vertically offset by 0.2 mm so it can be seen more clearly. (b) Optical density examples at various time of flights. Note that for TOF $\approx$ 1 ms and below, the cloud is not Gaussian, and so Eq.3.8 does not hold, and so such data are not included in the fit.

is hard to estimate how much of an effect this had on the final temperature, however it likely caused a small over-estimate as the apparent cloud size would be bigger if the edges blur.

3.6.6 Control system

In order to generate, control, and experimentally test a cloud of atoms in a MOT, a fast and reliable computer-run control system is required. This must provide, at the very least, a number of transistor-transistor logical (TTL) signals which in their simplest are on-off switches for hardware and software triggers. Further a number of analogue signals are desirable to ramp experimental parameters such as, in our case, the optical detuning or cylinder current. Traditionally this relied on expensive hardware running bespoke user created software or scripts developed in environments such as C++ and LabVIEW, which require significant expertise in software development.

To provide a low-power, small-volume (1.21), and low-cost portable solution, we instead implement a master-slave configuration comprising of three micro-controllers. One master [Arduino Leonardo] provides twelve fast digital TTL signals, two of which trigger two slave [Arduino Due] devices which each provide two further analogue signals. A simple overview is shown in Fig. 3.18. A compact battery array can service the three 5 V micro-controllers and attached simple 12 V step-down and amplification circuits.

The accessible high-level integrated development environment (IDE) provided as part of the Arduino devices allowed for fast prototyping of experimental sequences, being similar enough to Python, Matlab and C to present only a minor learning curve. However we found it beneficial to use specific bit addressing within the IDE rather than top-heavy (and so slower) high-level if-statement based functions. This allowed us to cut the on-off pulse width from 5 ms to 100 ns. The resultant combination of the three units and the above pulse-width reduction provided a flexible enough

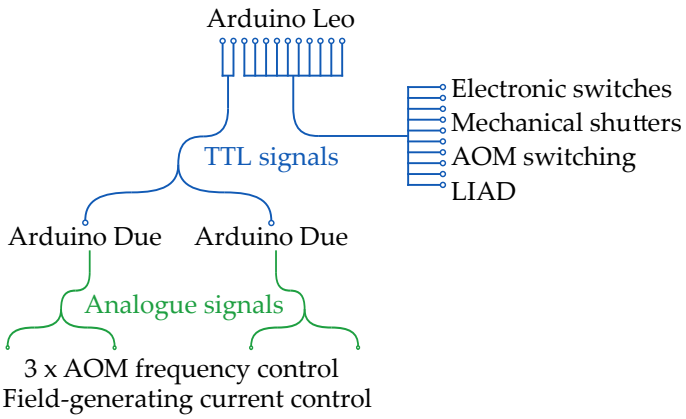

Fig. 3.18 Schematic overview of the hierarchy in the Arduino-based control system. All on/off TTL signals are provided by the Leo, two of these signals trigger two Dues, which provide a total of four analogue signals for various experimental equipment.

control space with which to scan and tune experimental parameters, and so test our cylinder trap's performance.

3.7 Performance of Cylinder Trap

The goal of the cylinder trap experiment was to test the feasibility of additive manufacturing as a technique for the production of quantum devices. Specifically it was investigated if metallic printed components would survive within a UHV environment, but also whether the structures themselves would impede the production or sustaining of the vacuum. Further, a number of comparative measurements were desired such that the device could be compared to similar structures producing large clouds of (ultra-)cold atoms. This section presents the major results for the cylinder trap in relation to the passive performance of the structure in UHV, and its active performance in the production of cold atoms.

3.7.1 MOT loading rate

The rate at which atoms are loaded into the trap is a critical number for systems which hope to have a short sequence cycle time, however it is also experimentally interesting as it reflects various properties of both the trapping fields and the background vapor pressure in which the trap is formed [164–166]. It is possible for the loading of atoms into a trap to be measured *in situ* via fluorescence imaging, collecting a fraction of the atom's spontaneously emitted light. This technique is particularly sensitive to scattered light and requires a clear light of sight to the clouds, both of which are issues for the rough diffusive surface of the cylinder trap and its limited optical pathways. Instead we measured the loading of the trap through absorption imaging, as discussed previously.

A selection of typical loading profiles can be seen in Fig. 3.19 for our cylinder trap in the regime where only the dispensers are used, i.e. no LIAD is implemented. Each data point is the average of five repeats of experimental parameters, and the light colored lines are fits of the system with the equation $N(t) = N_{eq}(1 - e^{-t/\tau})$. Here N_{eq} is the equilibrium atom number, t the experimental varied

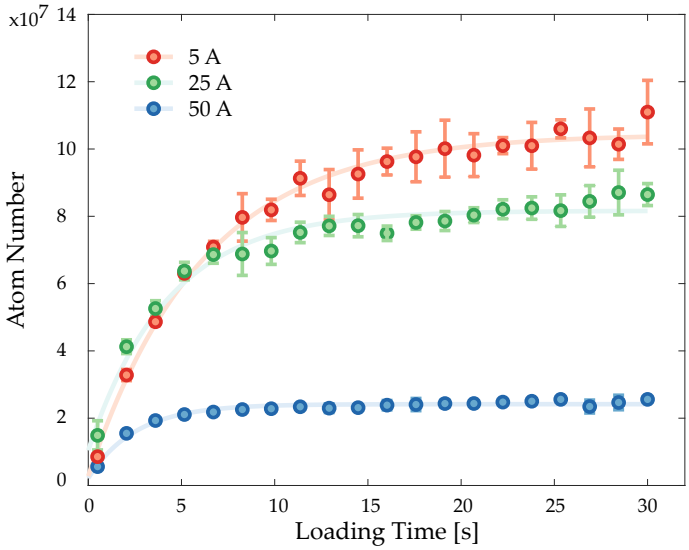

Fig. 3.19 Plots of typical loading curves found for the cylinder trap for differing cylinder currents, which is directly proportional to the magnetic field gradients. Curves are fit with $N(t) = N_{eq}(1 - e^{-t/\tau})$ to extract the final N_{eq} atom number and the charactertistic loading time, τ. No LIAD was used during loading.

loading time and τ the characteristic loading time of the trap. For the cases shown here with cylinder trap currents of $(5, 25, 50)$ A, the fitting provides $N_{eq} = (10.6 \pm 0.6, 7.1 \pm 0.7, 2.2 \pm 0.2) \times 10^7$ atoms and $\tau = (6.1 \pm 0.7, 4.3 \pm 0.9, 2.5 \pm 0.5)$ s. We see there is a clear trade-off between the final achieved atom number and the characteristic loading time, which from [164, 166] we see are determined and related as follows: $N_{eq} = \alpha P_{Rb} \tau$ and $\tau = 1/(\beta P_{Rb} + \gamma)$, where α relates to the MOT trapping cross section, P_{Rb} is the partial Rubidium pressure, βP_{Rb} relates to collision losses with other Rubidium atoms within the MOT and γ similarly relates to collisions with all atoms in the background gas, including stray hot rubidium atoms. It is the balancing act of these loss terms with the trapping cross section which determines the behavior that we see in Fig. 3.19 and the values we find for N_{eq} and τ.

Making use of the calculated characteristic loading time τ allows for a more efficient time scale to be set for typical system settings. That is to say there are diminishing returns in the atom number when $t \gg \tau$, within just 3τ 95% of the final equilibrium atom number is reached so there is little gain in loading the trap for much longer. In the case of high frequency measurement scans it may then make sense for a system to only be run between $\tau \leftrightarrow 3\tau$ to maximize the ratio of $N_{atoms}/t_{loading}$ and so overall reduce the full measurement time.

3.7.2 Cooler frequency scan

In the basic theory of a MOT [96, 99], it is the interplay of magnetic field induced Zeeman-shift, velocity-driven Doppler-shift and laser detuning which allows for a simplistic determination of the capturable velocities class. This in turn can be used to generate an estimate for the optimum laser detuning and magnetic field gradient. However, the full dynamics of a magneto-optical trap are elusive and various other experimental factors make it very difficult to generate a reliable prediction for the resultant atom number for a given atomic species, laser system and magnetic

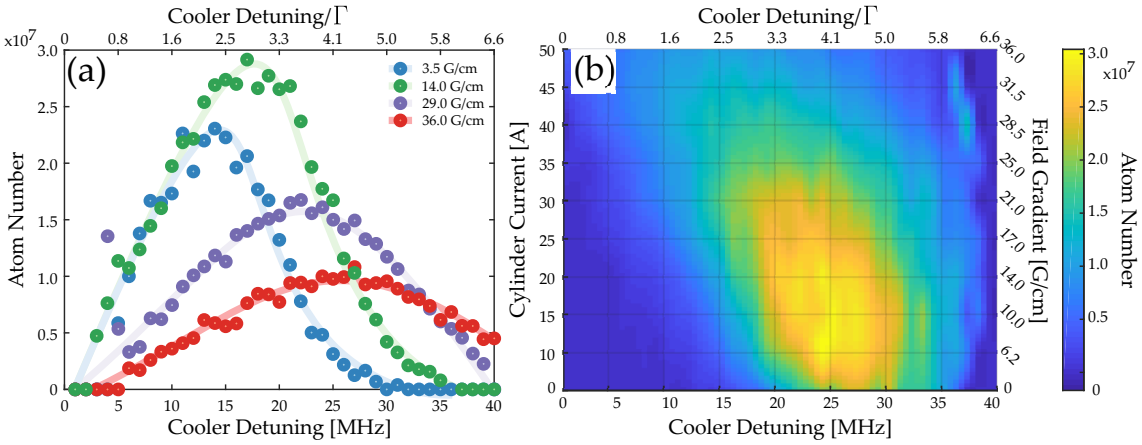

Fig. 3.20 Demonstration of the variation in the achieved atom number as the frequency of the cooler light is red detuned away from resonance at different cylinder currents, which relates to the magnetic field gradient at the trap center. (a) Selection of data showing the profile of the atom number as the detuning is changed. Solid lines are for visual aid and do not correspond to an analytically derived fitting equation. The negligible error bars are omitted to avoid cluttering the plot. (b) A cubic interpolation (Matlab) demonstrates the 2D profile of the atom number. See text for further details. Note that the maximum atom number in (a) is lower than measured in Fig. 3.19, as dispensers were run at a lower temperature (current) to avoid burning them out.

potential. These relationships must be at least explored experimentally such that at least a rough understanding can be gained to predict the achievable trap properties as systems reduce in size.

As such, Fig. 3.20 shows the resultant steady-state ($t \geq 2\tau$) atom numbers achieved for a specific cylinder current/magnetic field gradient as the cooler light frequency is red detuned away from resonance. There is a clear peak in the atom number for a given current and detuning, with a maximum being found at $\sim 20\,\mathrm{A}$ at $18\,\mathrm{MHz} \sim 3\Gamma$, corresponding to $\approx 14\mathrm{G/cm}$. The full range of data include currents from $1 \rightarrow 50\,\mathrm{A}$ in steps of $5\,\mathrm{A}$. In order to better visualize the two dimensional dependence of the atom number on current and detuning, we interpolate the data with a cubic-method, provided within the Matlab function *interp2*, in a grid of $0.5\,$unit steps within the data range. From the interpolation we see there is a rough higher atom number region between $8 \leftrightarrow 18\,\mathrm{A}$ and $18 \leftrightarrow 28\,\mathrm{MHz}$. As a benchmark, currents of $\sim 10\,\mathrm{A}$ correspond to $\sim 7\,\mathrm{G/cm}$ along the strong axis of the quadrupole. Data points in Fig. 3.20 which appear to show zero atoms are a result of the limitations of out camera system. Clouds of this size are to small to generate reliable absorption images, causing our fitting procedure to fail.

3.7.3 Atom number versus power consumption

No two ultracold atom experiments at the same, various experimental settings, procedures and architectures generate a parameter space of results which are difficult to compare directly without specifying individual, or several, metrics which are critical to the individual applications or measurement regime. One such metric is the initially trapped atom number. Many of these atoms are lost during the experimental cycle during which atoms are spatially translated, compressed and/or cooled, and so a value of $\sim 10^8$ atoms is desirable to correspond to the standards set in existing thermal atom quantum devices [33, 167, 168]. As one of the key aims of this device (See Sec. 3.2) is the electrical power consumed to produce these atomic clouds, we must consider the achieved

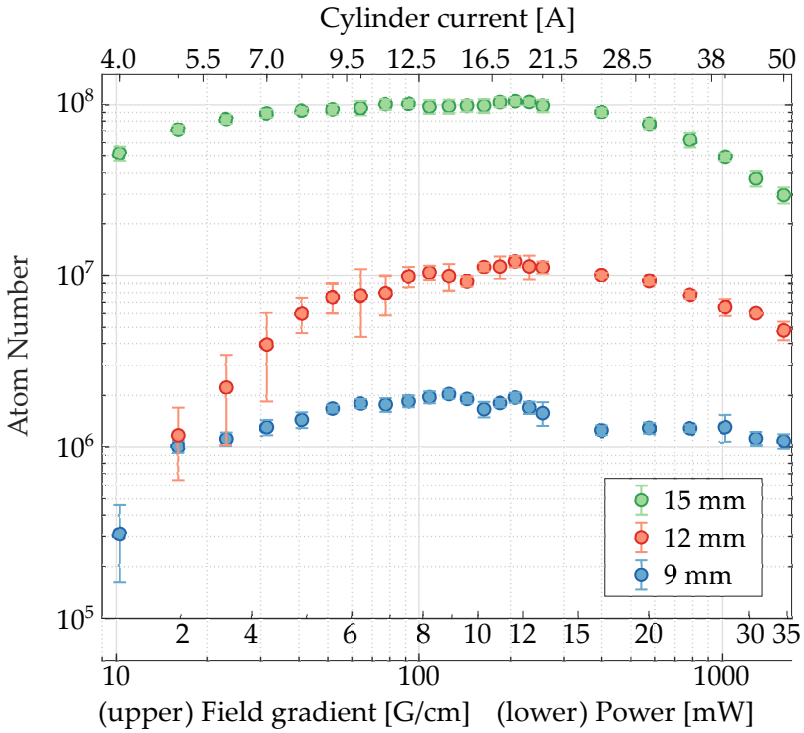

Fig. 3.21 Maximum atom number as a function of cylinder electrical power dissipation (current) for three beam diameters. The current range 4 A to 50 A corresponds to the magnetic field gradient range 3.2 G/cm to 40 G/cm

atom number in parallel to the power consumption. The overall reduction of the latter without significantly lowering the former is a key hurdle in the development of small, portable systems.

Our metric of performance is chosen to be the final atom number achieved measured against the required electrical power necessary to generate the trapping magnetic potential. Measurements are taken of the atom number via absorption imaging, for varying cylinder currents I which has a corresponding Ohmic power consumption $P = ZI^2$, where Z is the device resistance shown in Sec. 3.5.1 to be $(640 \pm 4)\,\mu\Omega$. Experimental settings are selected to best optimize the final atom number as discussed in Sec.'s 3.7.1 and 3.7.2, and the results are shown in Fig. 3.21. Data are collected in sequences of current scans, with ten runs alternating between scanning up or down in the cylinder current. These data are then analyzed and 'cleaned' such that null results and unrealistically high values ($> 10^9$) from incorrect fitting or other experimental faults are removed. As a result, averages are calculated using at least, based on the data removal, seven data points with error bars adjusted accordingly. In Fig. 3.21 the specific interpretation of the beam diameter perhaps needs clarification, as it is actually an indication of the aperture of an iris which is mounted onto the MOT guns. When fully open the aperture is 50 mm wide, matching the second lens in Fig. 3.13. As the cylinder itself clips the beam the largest possible aperture is the cylinder borehole diameter 15 mm, then the true $1/e^2$ beam waist would be found from a calculation of a clipped Gaussian beam initially having a $1/e^2$ diameter of around 50 mm. The iris is reduced to 15 mm to avoid excessive scattering of the waste light off the surface of the cylinder and other internally mounted vacuum equipment.

Let us first consider the attributes of the device in the case of maximum beam diameter, 15 mm by measurement of the energy dissipation across the cylinder itself. Atom numbers just

under 10^8 are reached for power dissipation levels of 30 mW, where the typical gradient of 10 G/cm corresponds to ~ 100 mW. We see a broad plateau which tails off above 300 mW and below 10 mW, where in the latter case atom numbers stay well above 10^7 even down to the lowest measured power of 4 mW. Values quoted here are specifically for the power dissipation across the cylinder itself; however, if all the connecting leads are considered, and so contribute to the total contact and material resistance, the power increase was found to be less than 50 %. In comparison to standard atom traps which can require up to 10 W of Ohmic power, such as externally mounted coil systems we will consider later, the power reduction is substantial. The atom number achieved as well as the electrical power consumed would be more adequate for a regime which eventually required a BEC, where in the subsequent experimental sequences after the MOT nearly all the initial atoms to be lost in evaporative cooling and inefficient transfer between trap minima.

Beam diameter The exact correlation between the achieved atom number N and any of the experimental variables, here now including the beam diameter D, is largely dependent on the specific experimental system. However building from the conceptual discussion of the device size in relation to the power consumption, and the experimental findings in Fig 3.21, it could be extrapolated that further miniaturization would lead to ever decreasing power consumption. As per the discussions in [99] regarding an upper bound on the capture velocity v_c [165, 166] and regarding the inclusion of the MOTs effective capture cross-section, there is some understandable uncertainty as to the exact lower limits on the volume of a viable MOT device for a cold atom source. The physically important volume, in regards to laser cooling, defines a trapping region given by the overlap of the six cooler laser beams, providing an optical field, and the linear magnetic field region, see linear region and effective volume discussions in Sec. 3.4. The coupling of these two regions is significantly more important as devices get smaller. In other words a smaller magnetic field generating architecture reduces the possible beam size; this critical when it has been shown that laser cooling with smaller beam diameters becomes increasingly inefficient where strong power laws have been verified, e.g. $N \sim D^{5.82\pm0.05}$ [169]. Allowing a sufficient, clear, aperture in the trapping geometry for larger laser beams is therefore a limiting constraint on the overall reduction in system size. It is the desired application, e.g. the choice of quantum sensing scheme, which drives the choice of aperture size. Our final prototype dimensions were chosen to guarantee the production of atom numbers in excess of $10^7 - 10^8$ atoms, so we chose the 15 mm diameter which puts the atoms cloud in that range while still keeping (Ohmic) power levels in the lower mW range.

With the above caution in mind, in order to empirically explore the lower limits of the aperture size, and consequently the prospect of significantly reducing the electrical power consumption (scaling with the cube power law as discussed), we perform a series of measurements with varying beam diameters with the cylinder trap the results of which are shown in the same Fig 3.21. Again these diameters are created from a clipping iris starting from an initial $1/e^2$ diameter of around 50 mm. We see that a 20 % reduction of the beam diameter from 15 mm to 12 mm still yields more than 10^7 cold atoms. If a corresponding scaling is done with the trap dimensions, a 50 % power reduction is achieved for the production of the same gradient. A further reduction to 9 mm, 60 % of the original size, achieves atom numbers of $(2.0 \pm 0.1) \times 10^6$. In this case an equitable shrink in the trap size would produce the same gradients at just 20 % of the original electrical power consumption. For all cases the atom number plateaus at currents of ~ 10 A, corresponding to field

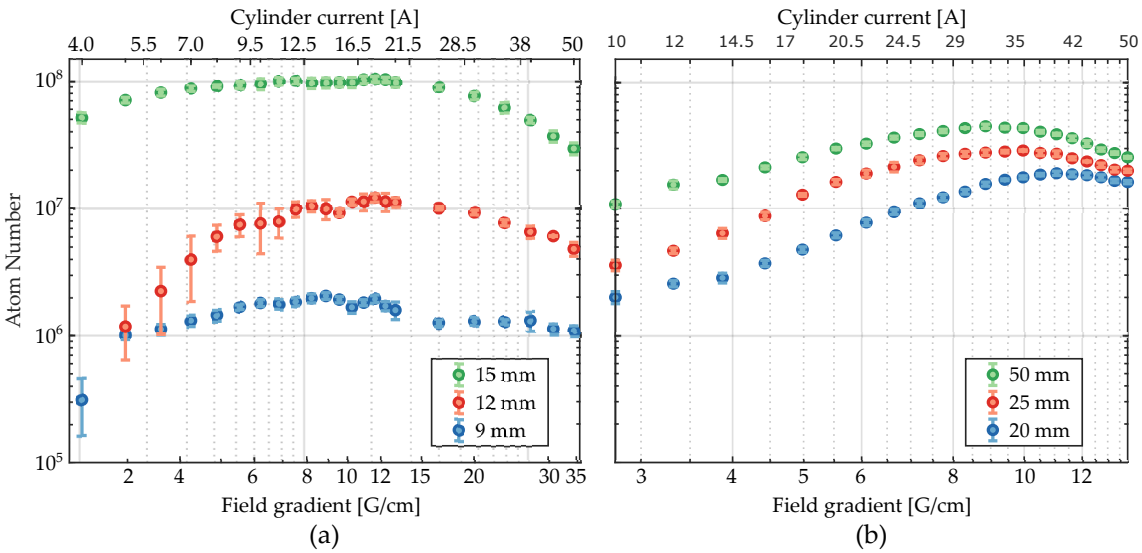

Fig. 3.22 Maximum atom number as a function of electrical power dissipation (current) in the cylinder trap (a) and an externally mounted coil system (b) for three beam diameters. The current range 4 A to 50 A corresponds to the magnetic field gradient range 3.2 G/cm to 40 G/cm

gradients along the strong quadrupole axis of ~ 7 G/cm. Again, as per Sec. 3.7.2 all currents and diameters are optimized for atom number in regards to the cooler frequency detuning.

3.7.4 Comparison with contemporary systems

While different experimental systems have variations we can use a contemporary set up evaluated under the same metrics as in the previous section to provide a clearer context to the cylinder trap results. In Fig 3.22(b) we show a similar set of measurements for a system with externally mounted coils, a standard six-beam MOT and dispenser-only sourced thermal atoms. Fig 3.22(a) is included again for clarity. Both systems have identical MOT guns designs (Sec. 3.6.2) which output Gaussian beam laser fields $1/e^2$ with diameters of 2 inches (50 mm), which are then truncated with iris diaphragms to the chosen diameter. Unlike the cylinder trap the external coil system can make use of the full range of the laser beam as there are no internally mounted structures within the main chamber to further clip the beam path.

In the coil case one sees a clearer peak around the 10 G/cm threshold for all beam diameters, with a small trend towards higher field gradients as the beam diameter is reduced. This gradient bears some agreement with the cylinder trap as to being a somewhat optimal target for MOT systems. However there are some obvious differences between the systems. The range in achievable gradients is significantly reduced for the coils. While they had the same range on input currents, they had a non-optimal geometry due to system constraints and were not in the ideal anti-Helmholtz configuration. Being externally mounted to a chamber identical to that which housed the cylinder also required that the coils be much larger, reflected in their electrical power consumption. To generate the same magnetic field gradient of 10 G/cm along the strong axes of the quadrupole, one requires 14 A and 36 A for the cylinder and external coils, respectively. In a crude comparison where one assumes both systems have the same Ohmic resistance, the coil system dissipates almost seven times as much power to create the same magnetic field gradient. This is however a severe

underestimate, and a calculation of the minimum resistance of the pair of externally mounted coils gives a $R_{coils} = 0.06\,\Omega$. In a direct comparison to the cylinder we find $R_{coil}/R_{cyl} \approx 100$, which does not include contact resistances nor joule-heating related resistance changes. In regards to power to generate 10 G/cm we find the ratio $P_{coils}/P_{cyl} = 600$; it is somewhat reassuring that this confirms the Ohmic resistance power scaling law of $P = ZI^2 \sim R^3$ for the cylinder trap length scale of 15 mm and the external coil radii of 12 cm. This readily compares with BEC experiments and other similar devices for quantum applications, where the power consumption can be up to 10 W.

It should be emphasized here that whilst we compared the produced magnetic field gradients for a given power consumption, a direct comparison of achieved atom number in the cases of Fig 3.22(a) and Fig 3.22(b) is highly ill-advised. Experimental variations such as the effective capture volume; the use of LIAD when paired with dispenser loading; the geometry of the magnetic potential, and the relative positioning of devices, effecting the local vacuum properties in the trapping region, to name a few, have a significant weighting on the final resultant atom number, cloud size and temperature. The final dynamics and behaviors are too multivariable for the analysis and measurements carried out in this work. We see this most prominently in the relative change in atom number as the beam diameters are reduced, for the cylinder trap a 20% reduction in D leads to almost an order of magnitude drop in the atom number when the peak values are compared; while for the coil system the 50% from $50 \rightarrow 25$ mm is match by a half drop in the atom number. The changes vary with field gradient too, indicating a more complex interplay between the beam diameter and the magnetic potential environment within which the atoms are captured.

3.7.5 Sub-doppler cooling procedure

To restate the adage of this work, the desired experimental protocol determines many of the targeted properties of the quantum resource. In this regard, the achieved temperature of the atom cloud is second only to the atom number in its importance, as colder atoms can enhance the performance of the sensor [170, 73], typically allowing increased trap lifetimes and interrogation times during the measurement sequence. Typically one considers the lower bound of the achievable temperature within a MOT as given by the Doppler limited temperature, T_D which for $T_D(^{87}Rb) = 146\,\mu$K, with any temperature below that arising from natural sub-Doppler cooling effects [96, 98, 99].

Without any additional cooling we produce a MOT with a temperature of $(170 \pm 4)\,\mu$K, an example optical density image of which is shown in Fig 3.23(a), which is slightly above the Doppler $T_D = 146\,\mu$K. In principle natural sub-Doppler cooling effects, such of polarization gradient effects, should have produced an even lower temperature. We suspect that slight deformities in the cylinder causing it to bend, and so affect the magnetic potential profile; misalignment of the optical beams, and finally poorly compensated stray fields limited our final achieved temperature. In the latter case, this is seen in a visual inspection of the expansion of the cloud on a fluorescence camera once the magnetic field was switched off. In this we clearly see, in a $\sim 1-2$ s window, the cloud expand and move down in the lab reference frame. Undesirable stray magnetic fields altering the effective magnetic environment experienced by the atom are typically a result of the Earth's magnetic field, but can sometimes be pinned down to local electronic equipment, and are generally removed with a set of compensation coils. These consist of three pairs of Helmholtz configuration

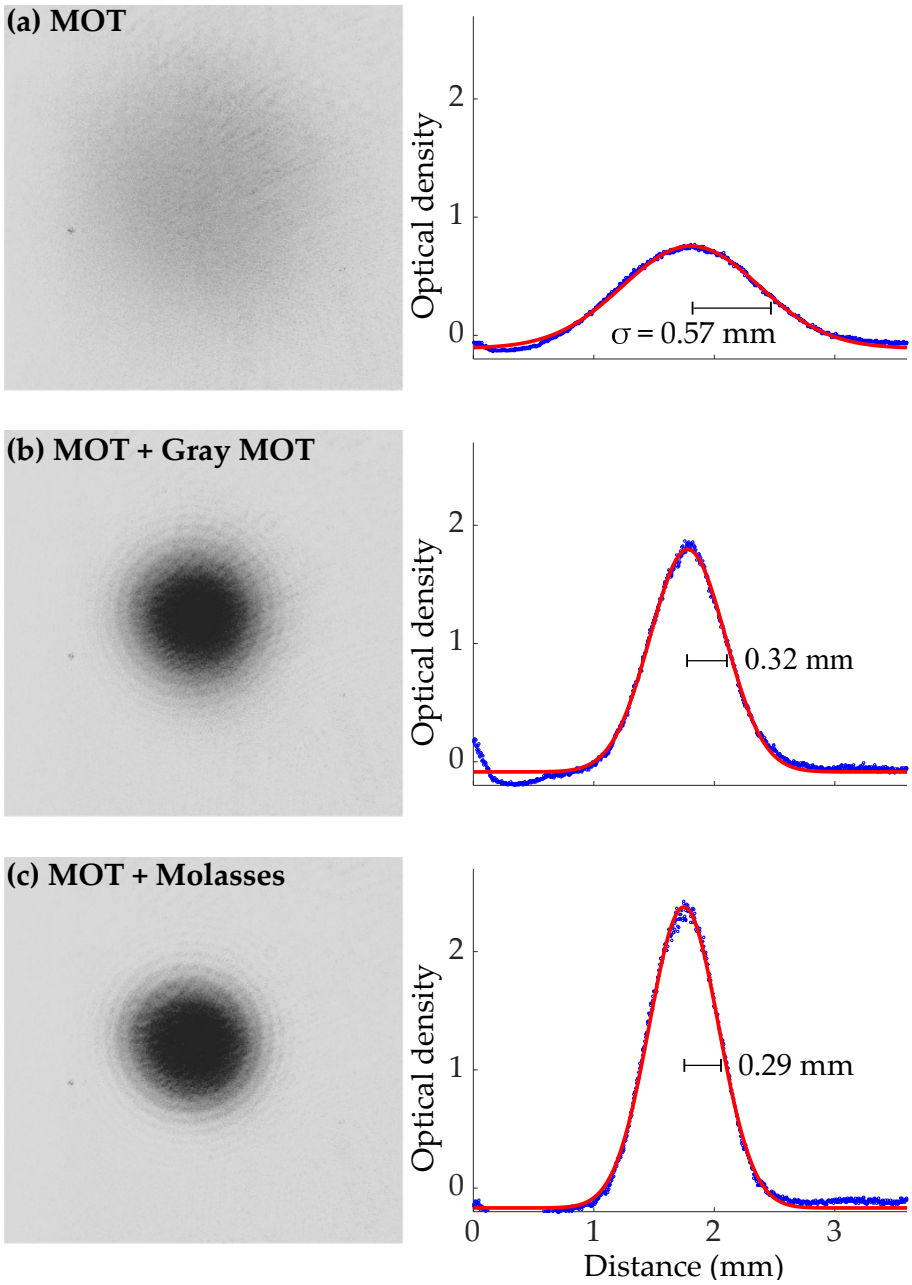

Fig. 3.23 Left: Optical density images of a cloud of atoms in three cooling regimes. Each single shot measurement is taken after 12 ms time of flight. Right: Vertically integrated optical densities (blue) with superimposed Gaussian fits (red). (a) A typical MOT cloud, (b) a MOT cloud after Gray MOT cooling (see text), (c) a MOT cloud after molasses cooling. The Gaussian width σ is indicative of the cloud temperature.

coils to compensate field discrepancies in each cartesian axis; at the time of measurement we did not have suitable coils to do this and so could not achieve a more reasonable sub-Doppler temperatures.

To reduce the cloud temperature further we employ more intentional sub-Doppler effects. Fig 3.23(b) shows an example optical density image taken following a simple 'Gray MOT' sub-Doppler cooling sequence carried out at the end of MOT loading, for full details see Sec. 2.2.4. This effect, in brief, makes use of the coupled effect of a spatially varying polarization gradient in the overlap of two counter-orientated circular polarized beams, *and* Sisyphus cooling [108, 26, 112]. In practice the optical field is detuned away from resonance while the magnetic trapping potential is unaltered. A frequency ramp of $6\,\mu s$ to a maximal red-detuning of 10Γ yields a cloud of $(3.7 \pm 0.2) \times 10^7$ atoms at an average temperature of $(29 \pm 1)\,\mu K$. We achieve even lower temperatures implementing a molasses (i.e. the optical field is ramped after magnetic confinement is removed) cooling scheme involving a $3.2\,\mu s$ ramp to a maximal red-detuning of 10Γ after MOT loading. An example from the molasses scheme is demonstrated in Fig 3.23(c), showing a cloud of $(4.0 \pm 0.2) \times 10^7$ atoms at a temperature of $(20.1 \pm 0.2)\,\mu K$. We found the variation in final temperature for Gray MOT cooling much smaller than for the molasses technique, for uncertain reasons. It is possible that switching off the magnetic field to carry out the detuning ramp (for the molasses case) somehow imparts a random thermal kick to the cloud, which we then see as a broader standard deviation in our measurement; however, this is purely speculative. It would also be worth investigating if the (quite small, relative to the optical) magnetic confinement during the Gray MOT cooling ramp means atoms are denser about the origin. Any misalignment of optical beams or stray fields would be more uniform across the spatially denser ensemble, which would be measured as a smaller standard deviation. Any improvements in the trap robustness and reliability would be important for portable systems, which may not be re-calibrated at all after production. It should be noted that the change in frequency, provided by the AOMs, also in turn reduces the overall peak intensity of the beam due to the efficiency profile of the AOM devices.

Chapter summary This chapter has introduced additive manufacturing (AM) as a method to produce a device to generate the necessary magnetic fields to trap atoms as part of a magneto-optical trap. A set of design considerations were outlined with respect to the limitations of AM, alongside which by consideration of common experimental parameters, a set of performance metrics were developed to test the device. These metrics and design considerations fed into a prototyping cycle within which field-generating structures were developed in 3D computer-aided design packages and tested in finite element software to both iterate and optimize design features. A proof of principle device called the cylinder trap was designed and printed. This also underwent a postprocessing procedure to improve electrical properties and improve the likelihood of survival within ultra-high vacuum (UHV) environments. The trap was place into a simple experimental setup, where atoms clouds of up to 10^8 atoms were generated with temperatures on the order of $(20.1 \pm 0.2)\,\mu K$ following molasses cooling and minimal electrical power consumption $\sim 100\,mW$. These trap properties were achieved without any measurable effects on the quality of the vacuum, with UHV measurements being taken of $< 10^{-10}\,mbar$. The device paves the way for further exploration of this new technology as a method to generate quantum devices, as well as rapid prototyping of experimental

Statement of contribution The research carried out and presented in this chapter was a significant portion of the author's research, and was done in partnership with fellow researcher W. Evans. As such it is difficult to draw strict divisions of contribution in regards to the experimental work. The design evolution of the cylinder trap was carried out by the author, with the original concept from P. Kruger, M. Fromhold and Y. Zhou at the beginning of the authors time at the University of Nottingham. Design iterations in CAD and calculations in finite-element software packages were carried out by the author, with discussions with our Additive Manufacturing partners to help guide the design aims. Similarly design and testing of the 3D printed vacuum flange was done by the author.

The experiment optical layout was design by myself, as were the early designs of the vacuum system. The construction of the experiment as a whole was done between the author and W. Evans, with data collection equally split. The initial drafts of our publication were created by the author. Initial measurements of the switch-off time were carried out by myself, however the significantly more thorough measurements presented were by W. Evans and T. Barratt. The comparative measurements shown in Fig. 3.22 were taken by the author, using a sister experiment with a similar set up. The Arudino control system was set up by W. Evans, with the author helping in debugging and testing of the sequences for our experiment.

Chapter 4

Blueprint for a Cold-Atom Source

4.1 Pathway to an cold-atom source

The primary goal of this work was the investigation of novel techniques and processes as stepping stones to the creation of a compact cold-atom source. This source would produce atoms for use in a stand-alone experiment, or would provide a flux of atoms to feed into a secondary experiment or measurement device. This is not a novel idea in itself, however there have been differing approaches chosen depending on the desired final application. We begin this chapter by reviewing some of these methods, in the context of working towards a next-stage device as a successor to the cylinder trap.

Cold atom sources In regards to the preparation of atoms in regions preceding the measurement location, it is common to see two-dimensional magneto-optical traps (2D-MOTs) [171–173] which are formed in bespoke vacuum chambers or glass cells. The cylindrical-shaped clouds form in regions of higher rubidium pressure and are then transported to regions of lower pressure, where the pressure gradient is maintained through a tight differential pumping tube. The cloud is typically then caught by a secondary three dimensional MOT configuration. The preparation of atoms in 2D-MOTs has a clear advantage in regards to its significant size reduction when compared to contemporary Zeeman slowers [174], but they require radial optical and magnetic confinement along its length and so adds further experimental bulk. In parallel single beam MOTs making use of concave reflective pyramidal, tetrahedral or conical surfaces [58, 60] milled into planes have existed for two decades now, and have shown promise for interferometric or gravitational sensors [57, 61, 62]. Viewed retrospectively, the arrival of *planar* grating structures, as opposed to structures milled into planes, developed naturally with this work. These single-beam grating devices [63, 65, 66] (or GMOTs) show great promise, generating all the necessary optical fields for a MOT trapped *above* the surface, so they can be interrogated with other probe beams readily, and integrated with other planar structures. GMOTs have been shown to achieve comparable sub-Doppler cooling [175] to our own cylinder trap. The very first reflectors and grating-based devices suffered from limited atom numbers, generally forming clouds in the range of only $10^5 - 10^6$ atoms, though recently 10^7 has become more standard.

Experimental limits on temperature In the techniques discussed above, including the cylinder trap work from Chapter 3, there are a number of hurdles to overcome. We consider first the limit of the temperature achievable by devices which solely produce atoms in magneto-optical traps, physically described as the recoil-limited temperature, see Sec. 2.2.4. This is a natural consequence of a system which applies optical fields to atomic systems. However, as described in Sec. 2.2.4, when transferred to a magnetic trap, atomic ensembles can be compressed and cooled via evaporative cooling, entering phase space densities not accessible in the MOT regime at the cost of atom number. The common end goal being the creation of a Bose-Einstein condensate, though this particular limit wont be explored in detail here. This cooling process is costly both in time, but more critically in atom number. Losses are inevitable as hot atoms are ejected and further losses can occur from background collisions, see below, during re-thermalization time. It is worth noting here that one can achieve smaller temperatures in a MOT simply by having a shallower trap, at the detriment of atom number, as the average temperature of the ensemble will then be naturally lower. This goes against our overall aim to have a large initial trap size.

Cycle time limitations Realistic field-based applications of quantum devices require that the total measurement cycle, from hot atomic vapor to the measurement of atoms is as short as possible. One approach is to improve the loading time of the MOT itself, arguably the largest allocation of time in the cycle, which for the cylinder trap we found a characteristic loading time $\tau \approx 2-6\,\mathrm{s}$, see Sec. 3.7.1, agreeing with contemporary work [51, 100]. To this aim, recent work [79] has shown promise in improving MOT loading times by creating an approximate Zeeman slower plus MOT in a compact hybrid package, recycling the same single beam used for the grating based MOT for the Zeeman slower. Alternatively, though not necessarily mutually exclusive, improvements can be made on the efficiency of transfer between the MOT and subsequent stage(s) of magnetic trap(s) [75, 176]. In doing so one can cede the desire for large atom numbers and settle for quick sub-second MOT loading times. Through the correct matching of trap properties, called mode-matching, atom numbers can be retained while the cloud is manipulated and transferred prior to evaporative cooling.

Trap lifetime In the techniques discussed, there is the mutual issue of *trap lifetime* [75, 79, 176]. It has been known since the early days of magnetic trapping [177] that the background pressure, or specifically collisions with stray background atoms, is one of the biggest limiting factors in regards to the retention of atoms within a magnetic, or even magneto-optical, trap[1]. Early magnetic traps **??** achieved on the order of 1 s trap lifetimes with a background pressure of 10^{-7} mbar, with the lifetime improving as the background is reduced. To complicate the matter, the background pressure of rubidium is required in order to generate the MOT itself, and typically the MOT location is by design overlapped with the position of the magnetic trap. Once the optical beams are removed and the magnetic-only part of the cycle begins, residual background atoms continue to interact with the cloud and cause losses. The need for a high-repetition rate limits the effectiveness of pumping processes to remove these atoms, and there is an argument that portable systems must recycle unused atoms to increase the device lifespan. Bespoke dispensers, as described in Refs. [77, 79] or

[1] Ignoring, of course, collisions with other trapped atoms in the trap itself.

LIAD based regeneration of adsorbed atoms [158], potentially offer solutions to the problem of both unwanted background atoms as well as device longevity. While 2D-MOTs offer a solution by pre-loading in a separate cell or chamber, this adds device size and additional complexity with additional optics.

Chapter outline In this chapter, I will discuss aimed at offering a solution to the issue of background pressure, whilst still outputting a reliable, high rate and high-number source of cold atoms. I will first give an overview of the 'timeline' of an atomic cloud as it progresses through the stages of an experimental sequence, up to measurement. This will seed the discussion of the design of a new cold-atom source, with the aim being to improve on the issues described in the introduction to this chapter.

4.2 Timeline of an atomic cloud

We introduce our atoms into the vacuum system via heated rubidium dispensers, which emit at a peak temperature in the range of 450 °C[2], putting the upper thermal RMS-velocity at $v_{th,Rb} \approx 460\,\mathrm{ms}^{-1}$. As discussed in Sec. 2.2.3, for a beam diameter of 50 mm, the MOT capture range is on the order of $v_c \approx 10\,\mathrm{ms}^{-1}$. Even though the capturable velocity is significantly lower than the RMS, we know empirically that there are still a sufficient number in the lower velocity classes to generate a MOT.

As we are building on the cylinder trap, we will take its results compared against contemporary results in [75] to extract target values for the MOT. From the atomic vapor we hope to capture a cloud of $10^8 - 10^9$ atoms. Estimated from Fig. 3.23 for a cloud with temperature $10 - 30\,\mu\mathrm{K}$, we expect a FWHM $= 2\sqrt{2\ln 2}\sigma$ in range of $1.0 - 1.5$ mm. Without fixing any strict experimental parameters just yet, we then aim to mode-match the magneto-optical trap to the preliminary magnetic trap such that there is an efficient transfer not only of atom number but also of phase-space density [178]. This is done by matching the aspect ratio and spatial distribution of the energy potential generated by the magnetic trap to the kinetic energy distribution of the MOT, though strictly we mean of the molasses-cooled cloud instantly after the optical and trapping fields of the MOT are removed. Assuming that the MOT cloud is spherical and that it is being moved into a purely harmonic trap, we can use the 1D case of Eq. 2.24 to calculate the *effective* frequency of the MOT. Having carried out similar sub-Doppler cooling processes, we take the hypothetical MOTs temperature and size to be, again from Fig. 3.23, 20 μK and $\sigma = 0.3$ mm, such that $f_{MOT} \approx 20$ Hz. Based on the temperature, we aim for the magnetic trap to have a very comfortable depth of 1 mK. The phase-space matching of the traps should make such a depth unnecessary, however experimental noise is unavoidable and could cause unwanted heating.

The final magnetic trap, if we consider it separately from the trap loading from the MOT, is determined by the final application of the atom source. However, the design intention is to produce an atom flux with a phase-space density beyond that achievable within a magneto-optical trap, and so the final trap must be sufficient for evaporative cooling, which we discussed in Sec. 2.5. Considering the work done in Refs. [27, 75, 100], we see that it is desirable during evaporative cooling to have a tight trap in regards to the frequency. The trap tightness determines the resultant

[2] SAES Rb flat-terminal-type

rethermalization time of the atoms, however it must not be to too tight such that atoms enter the regime of three-body or higher order collisions, causing significant losses [75]. There is an unavoidable increase in the trap depth when the tightness is increase, however this is not necessarily a negative, as during manipulation into this deep trap the ensemble will gain energy. Based on the work referenced in this section, trap frequency values of up to $\sim 2\,\text{kHz}$ are desirable. As we saw in Sec. 2.6.5, it is not possible to have an equally high trapping frequency in each cartesian direction and so we should expect one of the three trap frequencies to be significantly lower.

4.3 The Funnel Trap

This section presents the funnel trap design, a multi-stage device which would trap and cool atoms in a staged series of magnetic potentials, and are then propelled into another region for measurement. Each stage will be discussed, outlining the potential advantages when compared to previous work. Figure 4.1 shows an illustration of the basic elements of the structure, not showing the housing vacuum chamber, electrical connections or any mounting structures.

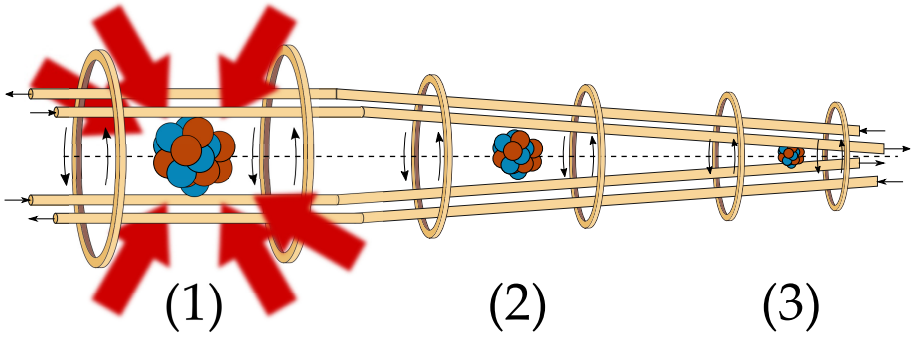

Fig. 4.1 Illustration of a multi-stage cold atom source. Each stage is not to scale. Stage (1): Atoms are first trapped in a MOT (MOT coils not shown), such that their center of mass exactly matches the position of the field minimum which is generated by an initial magnetic trap. Stage (2): Atoms are pushed down the funnel by successive coils, gradually being compressed by radially shrinking conductors. Stage (3): In the tightest end of the trap atoms can undergo rapid evaporative cooling, and then are propelled into the science region or chamber.

Stage One Atoms are first loaded from a background pressure in a standard magnetic optical trap consisting of six counterpropagating beams, or at least three sets of reflected beams, in order to ensure optimal optical fields for capture. The magnetic field is generated by a simple set of MOT coils, or a structure with an equivalent current path as per the cylinder trap. An Ioffe-Pritchard style magnetic trap is proposed, designed such that its trap center spatially overlaps with the center of the MOT. Using the typical spatial extents of a MOT, one can calculate the optimal geometric properties the IP-trap should have to best mode-match. The conductors for this initial magnetic trap are constructed such that they do not overlap any of the MOT beams, which will naturally form a lower limit on their distance to the trap center. Critical to this 'Stage One' in the device, is that the background pressure does not need to be tightly managed other than what is possible through current vacuum pumps, as once trapped in the first magnetic trap, atoms are pushed into 'Stage Two'.

Stage Two After the first magnetic trap, atoms are pushed through manipulation of the trapping coils into a funnel-like structure, several are shown in Fig. 4.1. This essentially consists of four tapering conductors of the same orientation as standard IP-trapping wires, providing gradually increasing radial confinement. This compression acts both to increase the atomic density, but also increases the radial trap depth. The rate of this tapering is somewhat arbitrary, as the transport through the funnel would be steered by the iterative control of the circular coils, similar to work carried out in Refs. [51, 179]. However the length of the funnel acts as a guided differential pumping tube, so there is likely some empirical optimum which balances out the passage of stray background fields to the lifetime of atoms as they are pushed through the guide.

Stage Three The final magnetic trap is loaded directly from the funnel transported atoms. Without the restrictions of the optical beams, as in the initial trap, this last stage can have more optimally designed conductors, such that a high-frequency, sufficient depth trap can be made with the benefits of three-dimensional conductors (see Sec. 2.6.1), hopefully with low electrical power. Without the presence of the hot vapor background atoms the trap lifetime should be improved. Atoms can either then be interrogated here for measurement, or propelled into a secondary zone, providing a flux of sub-microkelvin atomic ensembles. The independent stages of the funnel trap have an additional benefit. Once an ensemble of atoms has been produced and is pushed into the tapered transport region, the next magneto-optical trap can be formed. This would increase the average production rate of the source.

4.4 The coral chamber

Distinctly absent from the illustration in Fig. 4.1 is the housing vacuum system. During the work of the cylinder trap in Chapter 3.1, a simple off the shelf chamber was chosen to expedite the measurement. More important however was to ensure that any measured outgassing or vacuum pressure issues could be isolated to the printed structure itself. With the success of the cylinder trap, specifically in showing that SLM printed materials would survive and not detriment UVH environments, there is a natural question as to whether the same technique could produce a vacuum *containing* structure. If proven to work more exotic vacuum chamber designs would be possible, potentially reducing overall system size and mass. The pursuit of this proof of principle was the main output of collaborative work, awaiting publication (see preprint [95]), under the umbrella title of 'The Optamot Project'[3]

After an iterative design process, a simple chamber architecture was outlined consisting of two parallel CF40 (38 mm bores) sized viewports and eight CF16 (16 mm bore) viewports arranged around an octagonal perimeter. This would provide enough optical access to be somewhat flexible, as multiple identical chambers were printed for several groups. An internal skin of 2.5 mm is kept vacuum-side forming the backbone of the structure, with the thickness chosen to match the wall depths of commercial chambers. The core structure was then passed on to an optimization algorithm bespoke to our industry collaborators (Added Scientific) which aimed to reduce the overall object

[3] OPTAMOT: **OP**timised designs for **A**dditively manufactured **M**agneto **O**ptical **T**raps

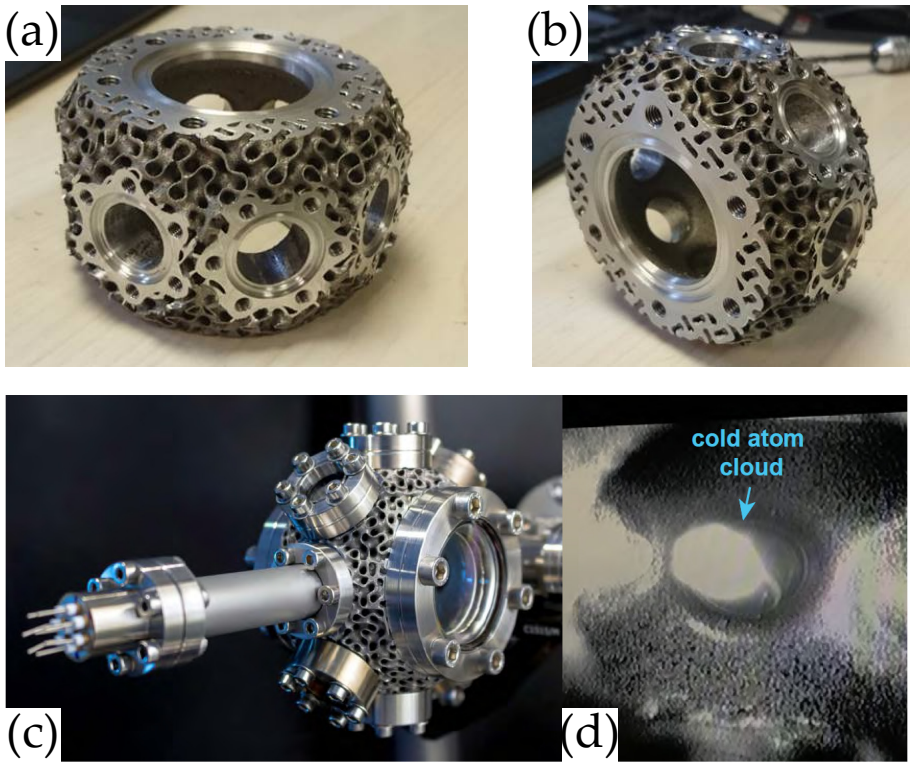

Fig. 4.2 Printed vacuum chamber, aka the coral chamber as features in the publication [95]. (a-b) Views of the coral chamber after machining of the knife edges, the chamber has two CF40 and eight CF16 viewports. (c) Chamber installed into a simple test system to demonstrate proof of principle. (d) A cloud of ^{85}Rb atoms trapped within the chamber, imaged with an infrared camera.

mass whilst still retaining structural integrity, the result of which is shown in Fig. 4.3 which we have dubbed the 'Coral' chamber, in reference to its sea coral appearance.

The full breadth of the results are presented in Preprint [95], but here I will present some of the major results relevant to this work. The chamber itself was printed using the same technique and material compound as the cylinder trap[4] and underwent a similar post-processing treatment. Vacuum knife edges, as per Fig 3.1, and threaded bolt holes were machined after printing and were tested for longevity and durability by W. Evans at Sussex. Torque tests to failure on the threaded holes showed the material held up to torque requirements from contemporary vacuum manufacturers (in the range of $100-200\,\mathrm{m}textkg$) and repeated sealing of the knife edges (up to ten cycles) revealed no obvious degradation when tested with a leak tester. One of the three identical chambers printed was installed into a trial system, as in Fig 4.2(c), and baked out at the relatively low temperature of 120 °C over 120 hours. This temperature limit was a result of a cautious approach by our additive manufacturing partners, who were concerned that higher temperatures could induce undesirable mechanical deformation and softening as a result of micro-structural changes due to heating. Softening in particular would reduce the ability of the flange to form a sufficient knife-edge cut into the sealing gasket. The system was pumped down using the same staged-process of vacuum pump as described in Sec. 3.6.1.

Fig. 4.3 shows scanning electron microscope images of the surface of the coral chamber. As in the cylinder trap, a major concern with the printing process was the presence of micro-voids or

[4] Al-Si10-Mg powder-alloy of chemical composition Al 88.9 wt%, Si 10.7 wt%, Mg 0.5 wt%

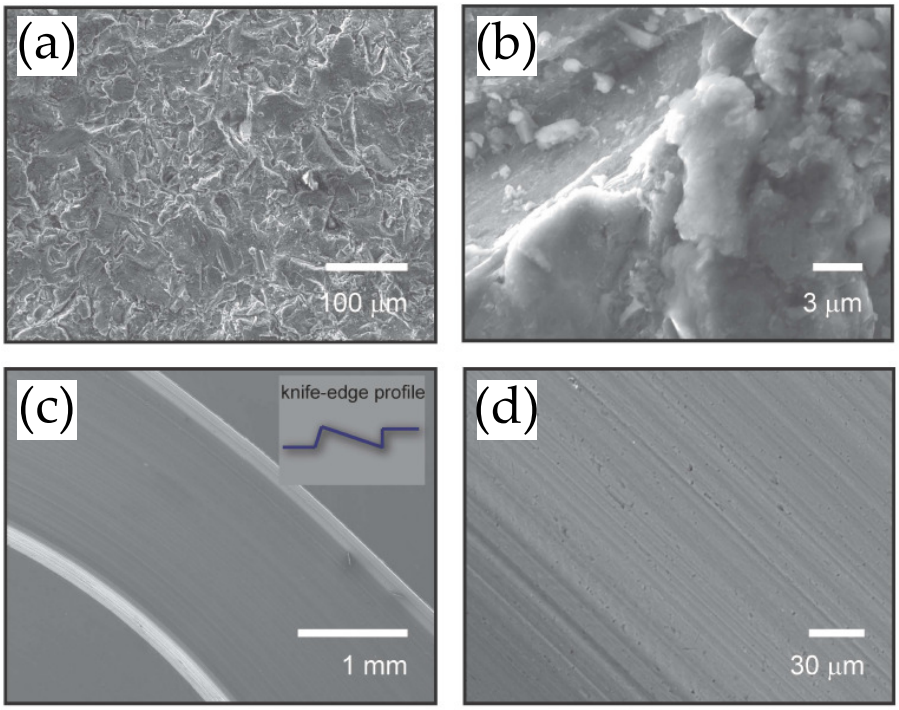

Fig. 4.3 Scanning electron microscope (SEM) images of the surface of the coral chamber, taken from reference [95]. (a-b) The surface prior to post-printing heat treatment, showing the surface roughness typical after printing. This is in comparison to (c-d), which shows the surface after post heat-treatment and having had the knife-edge machined. Inset of (c) shows the profile of this knife edge. Of particular note is the uniformity of the surface, with no air gaps or voids, and the sharpness of the knife edge.

fractures within which air pockets could form, significantly reducing the quality of the vacuum. Larger voids and fractures would also inhibit the effectiveness, or completely ruin, the sealing surface of the knife edges machined after printing. Figs. 4.3(a-b), showed the un-machined surface which had a measured surface roughness factor $S_q = 5\,\mu\text{m}$ measured as the RMS height over the sample area, with lateral features in the range of $1 - 10\,\mu\text{m}$. Figs. 4.3(c-d) show the surface after having been machined for the knife edge. Across all the images there is no evidence of significant cracks, tears or deep pores. In particular the machined surface features are purely a result of the machining tools, with no material details orthogonal to the machining direction and critically, no evidence of cracks across the knife edge itself. This result further corroborated the outcome of Chapter 3, and paves the way for more complex architectures.

The stand-out result of the printed chamber is achieving an upper pressure reading of $< 10^{-10}\,\text{mbar}$, limited by the measurement capabilities of the NexTorr ion pump filament. Whilst a pressure of $10^{-9}\,\text{mbar}$ is maintained for 48 hours with no active pumping. This is of particular interest for portable applications, as it significantly reduces the overall electrical power requirements of any future devices. The chamber itself weights 245 g, making it 50 % lighter than similar commercial products[5]. The durability of the material in regards to knife edges and bolt holts also bodes well for the chambers longevity as a reusable component.

[5] Kimball Physics, MCF275-SphHex-Cc2A6

As a final note on the coral chamber, evidence from x-ray photoelectron spectroscopy (XPS), carried out in the University of Nottingham by R. Campion, suggested the untreated and unmachined surface of the material had a protective top layer, composed of a disproportionate amount of magnesium. This layer is removed evaporatively if temperatures exceed 350 °C, but also through material post-treatment or machining. Significant outgassing of magnesium is found once this critical temperature is reached, but this is generally well beyond functional temperatures of common chambers which are usually limited to no more than 200 °C. However, local hot spots do occur due to dispensers and vacuum pump elements, and so this should be taken into account for future designs.

4.5 The magnetic traps

4.5.1 Trapping regimes

In the discussion of the Ioffe-Pritchard in Sec. 2.6.2, it was put forward that through specification of the desired trapping regime it would be possible to design an optimal configuration for a simple stick and loop case. This will be the starting point of our funnel trap discussion, and will then go on to feed into a realistic design which fits our aims, whilst being experimentally feasible.

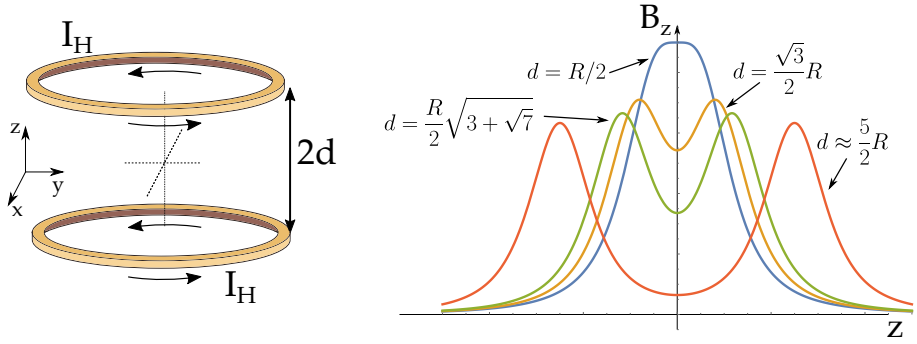

Fig. 4.4 A simple demonstration of the optimal regimes of a pair of coils in the Helmholtz configuration (a). (b) The z-component of the magnetic field strength along the axial direction of the loops. Showing, from top to bottom, the standard Helmholtz regime $d = R/2$; the maximum curvature regime $d = (\sqrt{3}/2)R$; the non-quartic component regime $d = \sqrt{3+\sqrt{7}}(R/2)$; and finally the regime of $\approx 90\%$ depth where $d = (5/2)R$.

In our simple model, laid out in Fig, 2.8, the four wires are straight forward to define in regards to the resultant depths and trapping frequencies they generate, using Eq. 2.35 and Eq. 2.34. We instead look to fix the geometry of the Helmholtz loops, and can consider these independent from the fields generated by the wires, the basic layout is shown in Fig. 4.4(a).

We can then define four regimes for consideration, with the aim being to improve the overall field quality and output whilst minimizing the required electrical power. For comparison, the first is the Helmholtz regime $d = R/2$, where d is the total separation of the coils and R the coil radii. The second regime is maximum curvature, which from Eq. 2.23 we see directly relates to the trap frequency. Thus we can find the maximum trap frequency by maximizing the curvature at the trap center ($z = 0$) with respect to the coil separation, i.e. solving the following for d,

$$\partial_d(\partial_{zz}\mathrm{B}_z|_{z=0}) = 0\,, \tag{4.1}$$

which gives the null solution $d = 0$, and $d = \pm(\sqrt{3}/2)R$, where we can take the positive solution as the system is symmetric. Whilst the curvature has a direct impact on the trap frequency, the presence of higher order terms of the field when expanded can generate complex behavior potentially limiting the quality of the magnetic trap produced. Higher order terms of Eq. 2.31 only exist for even terms, and contribute less. We chose then to zero the fourth order term in the expansion, which we shall call the non-quartic term regime, and find solutions of the form $d = \pm\sqrt{3 \pm \sqrt{7}}(R/2)$, where again we can take the positive solution. The final regime considered is in which the trap depth provided by the coils is 90 % of the maximum. This balances the requirement for the magnetic trap to have a non-zero minimum, whilst having sufficient depth to confine the atoms axially. This is done numerically and one finds that $d = (5/2)R$ to reach this regime. The four regimes are easier to compare numerically, as follows: $d = (1/2, \sqrt{3}/2, \sqrt{3 \pm \sqrt{7}}/2, 5/2)\,R \sim (0.50, 0.87, 1.19, 2.50)\,R$ for the Helmholtz, max curvature, non-quartic term and 90 % depth term in order.

Consequences of MOT geometry

We have already discussed, see Sec. 2.6.5, how such idealized regimes are difficult to implement in reality as the cost of optimizing one parameter, e.g. curvature/frequency, can make others, depth, impractical. However the calculations in Sec. 4.5.1 provide a guideline for what is achievable when one or several parameters are relaxed. This becomes particularly apparent when a restrictive geometry is put into the framework, as will be discussed here.

As outlined in Sec. 4.5.1, stage one of the funnel trap consists of a magnetic trap whose minimum is overlapped with the central position of a magneto-optical trap. The presence of the MOT beams (as this is a six beam configuration) restricts the available volume to the magnetic trap. This problem is similar to that of the design of the cylinder trap, in that we are trying to efficiently use the space not occupied by beams for conductive material.

The MOT geometry is defined in Fig. 4.5(a), showing two pairs of orthogonal beams in the plane, with the third pair not shown but going into and out of the plane. In the standard alignment, all three pairs of beams are orthogonal, however MOTs are possible when the relative angle of the planar beams is reduced [100]. In this picture, the system is completely determined by the beam radius, $D/2$, the angle θ, and the application-defined value a. Considering our case of two loops, one each in the upper and lower whitespace in Fig. 4.5(a), the value a defines the minimum radius that can exist whilst allowing the passage of atoms through the loop itself. We can then write the total seperation, S, as $S \geq D/\cos\theta + 2R\tan\theta$. Which, since D is already greater than zero, implies that $S > 2R\tan\theta$ Using the regime calculations from Sec. 4.5.1, we have expressions relating the separation $S = 2d$, to the radius R, and so can derive maximum angles for θ below which each regime is geometrically possible. This is done by calculating the threshold such that $2R\tan\theta = AR$, where the factor $A = (\sqrt{3}, \sqrt{3 \pm \sqrt{7}}, 5)$, giving $\theta_{max} = (40.9, 50.0, 68.2)^\circ$. Which suggests that it is not possible to reach the maximum curvature regime when using the standard geometry where $\theta = 45^\circ$ without the loop entering the forbidden region of the beam paths.

In these calculations a different process is required to solve the problem of designing the initial trap with a minimal power consumption, given a particular regime. As our aim is to mode-match this

first trap to the MOT shape, we can instead try to find solutions which fit the geometric constraints whilst providing a specific trap frequency, e.g. 20 Hz. This is done by reformulating our system in terms of the current required to achieve a specific trap frequency where the frequency is found from Eq. 2.23, and then minimizing this current with respect to one of our geometric parameters (S, R or a), where the choice of which is arbitrary as they are dependent on each other. The final expressions have numerical solutions and give the following, for a choice of standard beam size $D = 25$ mm: $\theta = 45^\circ$ gives $S = 25.6$ mm, $R = 7.9$ mm and $I_{45} = 4040$ A; $\theta = 35^\circ$ gives $S = 38.9$ mm, $R = 7.3$ mm and $I_{45} = 4640$ A. For either case, these currents are incredibly impractical for single loops, which suggests a final design will require circulating of the current.

4.5.2 Spatial alignment of traps

Attempting to optimize our system for a specific regime within our system bounds has not been fruitful so far, and so here we will try to calculate the regime under which the magnetic trap minimum position is exactly aligned to the geometric center where the MOT will form. In an *unrestricted* system, which we consider here to inform our understanding of our own system, the solution is trivial. Consider a single isolated loop, arranged such that gravity points down along the loop's axial center. Atoms will be trapped, or levitate, above the loop with minimal current at the point where the maximum force due to the magnetic field generated by the loop is equal and opposite to the force due to gravity, which occurs at $z = R/2$. The current at this minimum can be found to be $I = (m_{Rb}g/\mu_0\mu_B)5^{5/2}R^2$, where m_{Rb} is the mass of rubidium, g the acceleration due to gravity, μ_0 the permeability of free space and μ_B the Bohr magneton. All such solutions however would clash with the optical beams in our case.

Solving for the single loop with the boundary condition $S \geq D/\cos\theta + 2R\tan\theta$, provided by the MOT geometry, requires numerical evaluation of the system. We can evaluate it for the following system where $D = 25$ mm and $\theta = 45^\circ$, and minimize the current with respect to the choice of radius R, which gives $R = 11.7$ mm, $S = 48.4$ mm for a current of $I_{min} = 637$ A. Whilst this is high, we are starting to approach a region in which multiple recirculated loops may be able to achieve an approximation to such a system. The introduction of gravity into our formalism highlights the considerations of gravitation sag on the cloud once it is loaded into the initial trap. So far the funnel trap has been defined without regard to its relative position with respect to the directional force due to gravity, however from now we will assume it points along the axial direction of the funnel. A truly portable device would have to be much more flexible, however as we will see later, it is only a significant problem for the initial capture of the cloud, as once compressed the effects due to gravity are outweighed by the local magnetic field strength.

4.5.3 Stage one trap: recirculated current

The position-matching calculation from the previous section gives us a baseline with which to calculate a *recirculated-loop* system in which we approximate a coil with a series of stacked, concentric loops. To make this calculation more realistic, a choice of wire diameter is required such that the thin loops can be stacked with the appropriate separation. A 1.1 mm max diameter UHV

compatible, Kapton-insulated wire was selected[6], which has a max load of 10 A. The stacking pattern of the circular 'inner' coils is shown in Fig. 4.5(b). A Matlab calculation was then carried out in which, from a single pair of thin loops, the number of loop stacks and concentric rings was increased, calculating the magnetic field and effective energy profile each time with gravitational effects included. By using a minimum energy search algorithm [core function Matlab inbuilt *fminsearch*] about the geometric center of the trap, the trap minimum was found. Knowing the position of the trap center then allowed for a Hessian calculation of the magnetic field magnitude curvature, and so then a calculation of the traps frequencies and depths.

The results are the recirculated calculation are shown in Fig. 4.6, with the following parameters:

- The four wire current was fixed at 150 A, to be recirculated later, with the wire positions on a square fitting a circle of radius 12 mm.
- The number of layered stacks, n_{layer}, and number of concentric loops n_{loops} is increased from $(n_{layer}, n_{loops}) = (1,1)$ to $(n_{layer}, n_{loops}) = (50,6)$ symmetrically (on top and bottom).
- The maximum radius is $R = 11.2$ mm, shrinking down to $R = 5.7$ mm for the smallest sixth concentric loop, leaving an narrow passage of about 10 mm diameter for atoms to be transported through into the funnel region (Stage Two).
- The stacks vary from 29.5 mm to 56.5 mm measured from the geometric origin of the loop geometry.
- The current in the lower set of loops is fixed at 20 A per loop, with the upper loop having exactly $2/3$ of this value. The exact ratio of currents will be best determined experimentally to ensure the trap center is at the origin, as there will be imperfections in the winding of the loops.

Considering Fig. 4.6(top), though it is true for all three plots, there are diminishing returns for the improvement of the trap position as the number of layer stacks is increased. This is a natural consequence of the $\sim 1/z$ relation for the field strength of a loop relative to the distance away from it. Or simply put, it is more efficient in regards to the current density to pack in more current closer to the region of interest, which in our case means more concentric loops are better than more layers. Based on this, we chose a recirculated design of 12 layers and 6 concentric loops which gives the following trap properties: $f_{(x,y,z)} = (17,20,8)$ Hz at $r_{min} = (0,0,-3)$ mm and a smallest depth of 1.7 mK. These numbers are quite promising for our application, however we must now recirculate the four wire structure to get a final design. As a note, we have overshot the maximum current of the commercial wire, however from experience this can be done somewhat confidently if only done for a short time and with enough heat sinking of the coils.

Recirculating the four wires

A similar procedure was then carried out for the four wires in which pairs of wires were connected to form rectangular loops, the side profile of which is shown in Fig. 4.5(b). The addition of loops and

[6] Allectra, 311-KAP-100

concentric 'rings' in this case required a careful consideration of the geometry of the MOT beams, leading to a tapered design where the rectangular area defined by each loop had to increase further away from the trap center, to allow for the spreading MOT beams. To complicate the previous calculation of the circular loops, the upper and lower ends of the rectangular loops contribute to the field along the z-axis. Specifically the lower structure contributed *with* the circular loops, pointing along the same direction as can be see in Fig. 4.5(b), while the upper connections worked *against* the circular loops.

This interplay between the two sets of conductors had unforeseen consequences on the effective trap depth. The trap depths calculated in Fig. 4.6 assumed that the minimum energy barrier existed along one of the cartesian axis, which for the case of the circular loop optimization was along the z-axis. However, the combination of gravitation sag and the more complex geometry with the rectangular loops shifted the minimum energy barrier out of the x-y (or radial) plane. In order to find the 'hole' in the trap three dimensional energy iso-surfaces were created, by setting a specific iso-temperature value, e.g. 1 mK it is possible to then visualize the appearance of holes in the surface through which atoms above the set iso-temperature would escape. An iterative process was then carried out in which the number of rectangular loops and stacks were varied until the iso-surface was closed for a specific energy/temperature value.

Fig. 4.7 shows the final result of such a process, with the central blue region depicting the z-x view of a 950 μK isosurface. The lower loops carry 13 A, and the upper 1 A. The square conductors are six concentric rectangular loops of five layers, carrying 20 A. Two dimensional cuts of the isosurface are shown in Fig. 4.7(c-d), showing this particular configuration of currents gives an effective depth of about 900 μK. Trap frequencies are calculated to be $f_{(x,y,z)} = (18, 22, 5)$ Hz, at a trap position of $(0, 0, -1)$ mm. In order to avoid to detrimental interference of the upper rectangular loops with the circular coil stack, the rectangular profile is stretched up. This effectively creates a U-shaped profile for what was originally the four Ioffe wires.

The achieved frequencies, trap positions and depth of this circulated trap all fall surprisingly close to the original aims of the stage one trap. Whilst we were unable to put design the trap exactly within one of the optimal regimes as shown in Fig. 4.4, we were at least able to approach the mode- and position matching requirements. As a last note on this model before moving on to the final trap design, it is clear from Fig. 4.7(a) that a cloud of a temperature even well below the isosurface value will lose some atoms if it is pushed down through the inner radius of the lower loops. To test the compression of the cloud, Fig. 4.8 shows the same set of calculations for an increase in the rectangular loop current to 30 A. The effect is to increase the frequencies to $f_{(x,y,z)} = (5, 27, 32)$ Hz and lift the trap position to $(0, 0, 1.5)$ mm, whilst the 950 μK surface at its broadest spans now ~ 7 mm, fitting into the 10 mm inner diameter of the lower coil.

4.5.4 Stage three trap: the final magnetic trap

The design and modelling of the final trapping region in principle follows the same procedure as the initial trap, without the geometric restrictions of the MOT beams but requiring significantly higher trapping frequencies, on the order of $1 - 2$ kHz from Sec. 4.2 and depths in the region of $1 - 2$ μK. However, as we can now move the conductors much closer to the trapping region it is no

longer appropriate to use the approximation of infinitesimal wires and loops as the cloud center of mass position will be potentially less than a millimeter away from the conductor surface.

We take the situation in which the Ioffe-bars (up to now the wires) are within the radius of the loops, as depicted in Fig. 2.8. We define some central cylindrical volume which the atoms occupy, where the cross section diameter is given the label t_g. The four Ioffee bars can then occupy any of the space around this forbidden region. The standard wire cross section is circular, as in Fig. 4.9(a), with each 'bar' having a radius R with their relative centers on a standard square of diagonal length $t_g + 2R$. Using t_g and the cross sectional area $A = 2\pi R$, we can then define other conductor shapes in terms of the same area A with the same fourfold symmetry around the forbidden region. Three such alternative conductor shapes are shown in Fig. 4.9(b-d). Each design has potential advantages in regards to the optical access it provides, e.g. for imaging beams, or the efficient distribution of current density.

As the Ioffe bars are free-standing, they cannot be too small otherwise they are likely to bend or warp during installation. A diameter of 1 mm was chosen, as this would be the smallest feature size with $R = 0.5$ mm. The internal void where the atoms would reside was then chosen to be 550 µm which should be sufficient based on the typical atom cloud sizes for these frequencies, as shown in Ref. [75].

Each cross section was then constructed within a finite-element package (Comsol) and the current density calculated and exported for field calculation into Matlab with currents of 35 A passing in the bars. In each case axially confining loops of $R_{loop} = 1.5$ mm used with a total separation of 16 mm found through manual adjustment to improve trap frequency and depth. Of the four conductor cross-sections, the segment-styled cross section out performs the others very slightly. The trap frequencies found were $f_{x,y,z} = (1000, 1000, 200)$ Hz, with minimum depth of 4 mK and a $B_{min} = 1$ G at the energy minimum location which is effectively at the geometric origin. The numbers for the cloverleaf style trap are very similar; however, the nearest surface to surface distance in this cross section is 0.05 mm which would be very restrictive to optical access even for highly divergent imaging methods. The segment variation had instead a smallest distance of 0.1 mm. The current of 35 A is potentially a source of experimental issue when actually implemented, however when compared with the conductor area of similar-sized wires [see again, Allectra, 311-KAP-100], the total cross-sectional area A is roughly three times the size of the 10 A limited wired used in the initial magnetic trap. With sufficient heat-sinks, this still puts the model within the realms of possibility.

4.6 Funnel trap model

With the calculations and models calculated in the previous sections (4.5.3,4.5.4), this chapter will conclude with a realistic design of the funnel trap. A selection of CAD renders are shown in Fig 4.10. Experimental design is an iterative process, with various unforeseen constraints and hurdles, and so this will likely only form the 'core' architecture of a final model.

The main chamber of the trap is roughly equivalent to the coral chamber, with six viewports designed to match the CF16 standard aligned on the main plane of the chamber, and two further orthogonal viewports of the same size pointing into and out of the page. Six of these make up the

three pairs of optical access ports for the magneto-optical trap, with two 'spare' ports for imaging, vacuum connections and/or electrical feedthrough connections to air. The fluting of the viewports allows for fastening bolts to be accessible by hand, however a similar analysis could be carried out, as per Fig. 4.4, so that bolt-holds can be sunk into the main chamber volume with sufficient structural strength to sustain the fastening process. In interior skin of at least 2 mm is maintained throughout.

Two MOT coils with a roughly 40 mm radius and in the ideal anti-Helmholtz configuration of $d = R$ exist in the X-Z plane, however they are omitted from the figure for visual aid. The recirculated circular and rectangular loops of the initial magnetic trap, designed to capture the MOT efficient through positional and geometric mode-matching, are approximated in the design with block conductors. These are highlighted in Fig. 4.10(C-D). The circular loops are supported by the monolithic chamber design by symmetric fluted mounts. In the upper-coil case this mount is solid, however in the lower coil this mount is hollow, providing the magnetically trapped atoms passage over 20 mm through to the main funnel region, while also acting as differential pumping between the higher-pressure main chamber volume to the lower-pressure funnel-region. The diameter of the passage is 8 mm, which based on work in Ref. [100], will likely be too wide. A graduation could be added to shrink the diameter, with the confining currents compensating for this and compressing the atoms. A similar scaffolding-like structure supports the rectangular loops, partially visible in Figs. 4.10(C-D) as the V-shaped arms, arranged such that the optical access from any of the viewports is not blocked. All of the structural mounts provide a frame upon which the coils can be constructed, but also act as heatsinks to the main body of the vacuum chamber.

The conical appendix to the lower end of the chamber shown in Fig. 4.10(E), similar to conical vacuum adaptors, contains Stages Two and Three of our funnel trap design, including to the length of the differential pumping tube. The wider and upper part of the coil appears to be directly connected to the main body of the chamber; however, the cone is a separate monolithic component fastened against the upper body with a standard knife edge seal. This is necessary so the conductors in the highlighted area can be installed. These conductors consist of four tapered Ioffe bars with the cross section, see Sec. 4.5.4, banded by a series of shrinking coils which help transport atoms along the axial length of the funnel. The structure ends with a straight set of conductors spanning 5 mm to make up the final, high frequency region of the trap. An access port is provided below either to emit the atoms or for imaging purposes.

A number of experimental hurdles present themselves when the design in Fig. 4.10 is considered. Across both regions of the two-chamber design, what is not shown are connecting wires and structures to mount conductors to feedthroughs. The omission avoids a complex mess of conductor geometries, most of which will be reliant on the actual commercial or bespoke-made product used. In regards to constructing the coils in the upper chamber, a larger access port may be required in the plane of the small viewport.

During the atoms passage through the differential tube they must be compressed to avoid them hitting the inner diameter of the tube itself. This is straight forward with Ioffe-like structures, however there is a region between lower cone chamber and the upper where conductors cant pass without through holes, which would act as additional differential pumping passages. In custom commercial chambers it is possible to have feedthroughs installed which span chambers whilst

maintaining a vacuum seal, and so would solve this issue. It is not clear yet if this has been accomplished with 3D-printed materials, and so would require further investigation.

Finally, in the cone chamber there is currently no structural support, and consequently no heat sinking, to fix four tapered conductors and the circular loops. It would be possible to have additively manufactured supports, however the sizes of the structures would mean difficult aspect ratios for the printing process, resulting in many of the supports themselves snapping during printing or post-processing. Since the cone volume requires little optical access, one potential solution would be to suspend the various loops and tapering bars into a layered, non-electrically conductive but highly heat-conductive material. This would appear similar to a many-layered sponge cake, with hollowed regions in which conductors would be placed in order and having a central void in which the atoms would exist. Common UHV-compatible solutions used in atom chips and PCBs [51, 100] are materials such as Polyether ether ketone (PEEK), Rogers (commercial name, used often in radio frequency circuitry), or a machinable glass-ceramic (commercially known as Macor). The benefit of one material over another is often driven by what is locally manufacturable, and would require significant investigation to test the feasibility of such a structural design.

Chapter summary In this chapter we have investigated a next-generation atom source which would output a flux of sub-millikelvin atoms. The proposal has multiple stages, the first of which is designed to best capture atoms from a magneto-optical trap by matching the spatial distribution of the ensemble with a magnetic trap. The layout of this first magnetic trap was driven by a series of calculations to try and optimize this mode-matching. After this trap, atoms are compressed and transported along a guided three-dimensional funnel, through a differential pumping aperture, into a tight trap. Here rapid evaporative cooling can occur, whilst benefiting from a minimal background pressure. simultaneously to this cooling, the next MOT can be formed in the high-pressure region, reducing the average cycle time. A model is presented, consisting of a two-volume printed vacuum chamber with internal supporting struts, providing both support and thermal dissipate channels. This design was encouraged by promising results of the coral chamber, an additively manufactured miniature vessel tested down to $< 10^{-10}$ mbar.

Statement of contribution In regards to the non-OPTAMOT part of this chapter, the authors contribution was 100 % of the research, calculations, modelling and design presented here. This included building of a Matlab toolbox to calculate the unusual geometries presented in an iterative way, allowing for fast calculations of different schemes. However, this work was presented multiple times to my peers and so was helped by discussions with W. Evans, F. Orucevic and P. Kruger.

The initial conception of the OPTAMOT project came from the printed vacuum flange, and the author presented several speculative designs to Additive Manufacturing group. W. Evans build on these primarily with L. Coles of Added Scientific (a spin out of the research group), though with some input from myself, and developed the coral chamber design presented here. The author contributed to the experimental testing of the coral chamber, including designing the optical systems used in the ‘Blue Lab’ at Sussex University.

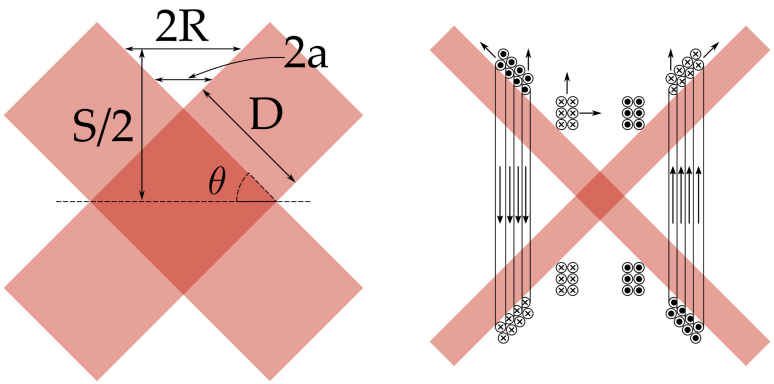

Fig. 4.5 Designing the initial trap for atoms to be efficiently captured from the MOT. (a) The geometry of the MOT beams, which determines the available volume for the magnetic trapping conductors. (b) An idealized Ioffe Pritchard trap can be constructed in the available space around the MOT beams. The inner conductors form the Helmholtz loops and thus the axial confinement, and outer structures provide confinement in the radial plane. Arrows indicate the direction of additional loops or additional layers to improve the field properties and reduce the required current.

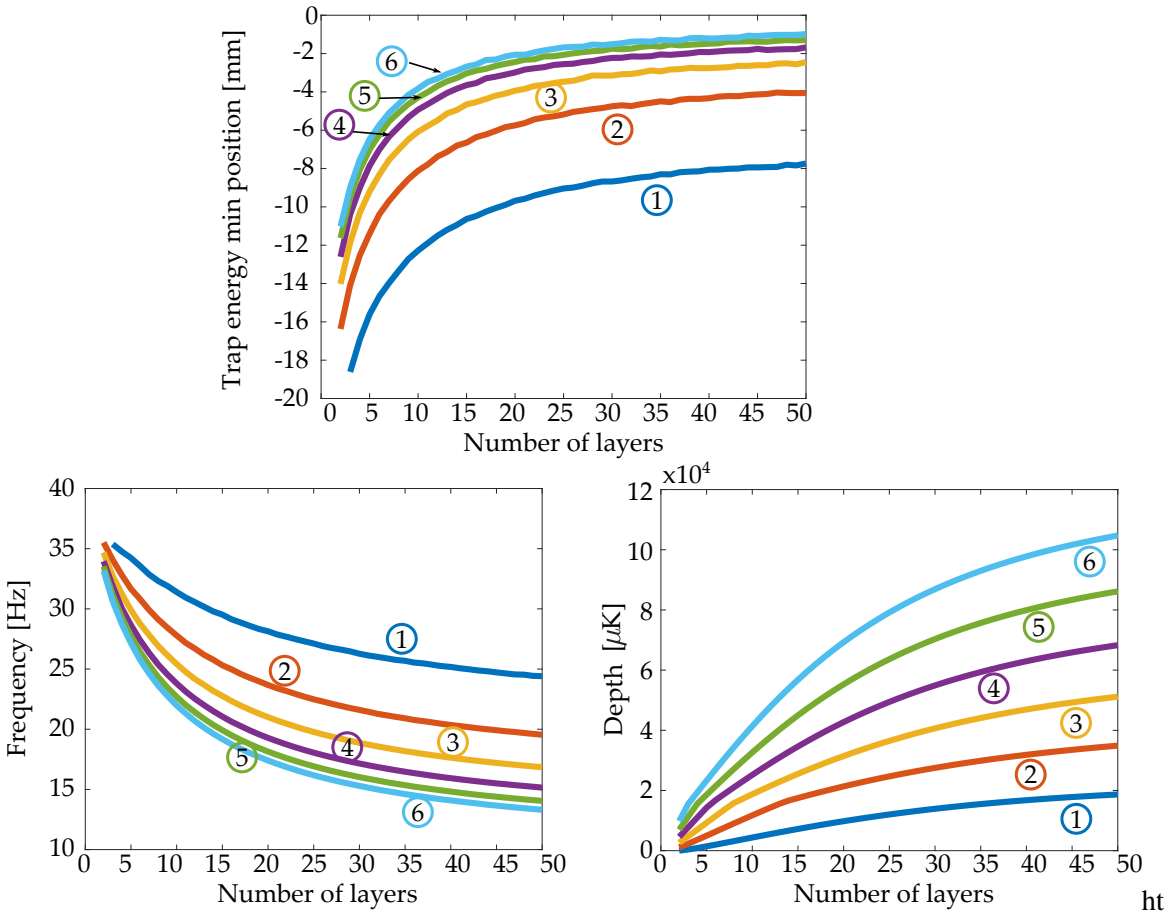

Fig. 4.6 Calculations of trap properties for the design for the stage one trap, specifically the circular loops, see text for details. Numbers $1-6$ indicate the number of concentric loops, started from the outer loop of $R = 11.2\,\text{mm}$ to an inner loop of $R = 5.7\,\text{mm}$. Top image: Position of energy minimum of the trap, offset from geometric center at 0 mm due to gravitation sag. Bottom left: Trap frequency (along z axis) calculated via Hessian method at the energy minimum. Bottom right: Depth of trap along the z axis, calculated by $E_{peak} - E(r_{min})$, where r_{min} is the position of the energy minimum and the subscript peak indicates the energy calculated at the lower of the energy peaks along the z-axis.

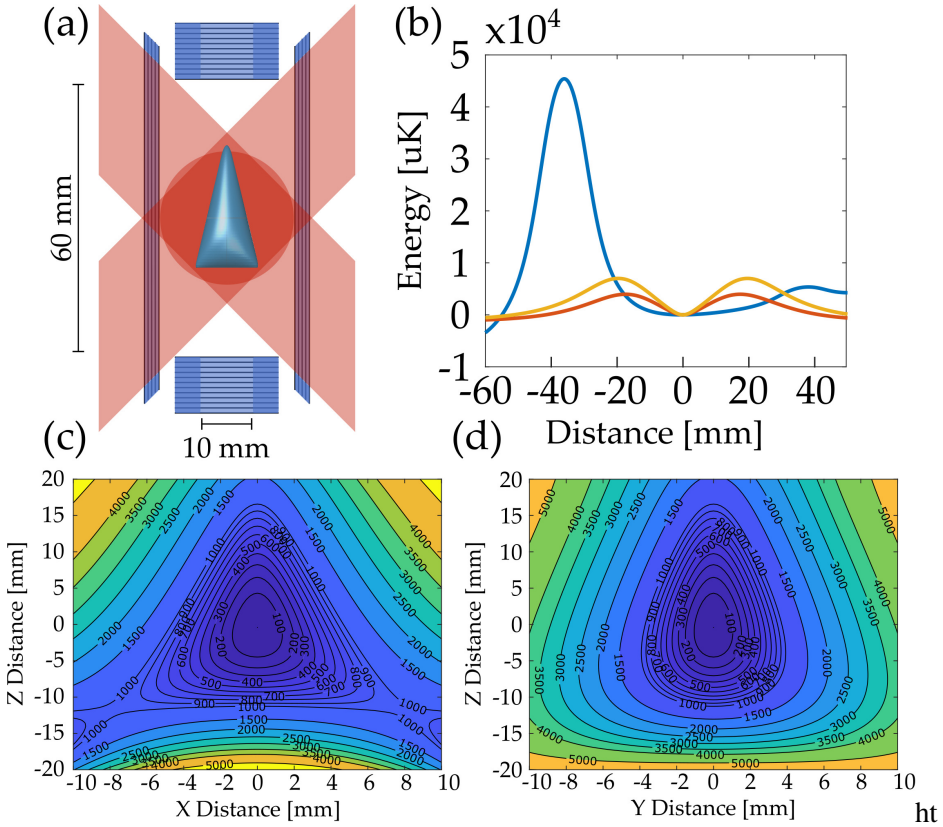

Fig. 4.7 Demonstration of a realizable conductor design to capture atoms more efficiently from the MOT through mode-matching of the trap geometry. (a) A composite image showing the position of the MOT beams overlapped with a 2D projection of a 3D energy isosurface of 950 μK generated by the magnetic trapping structure. The MOT beams are shown to illustrate how the conductors must fit their profile, but would not be active during magnetic trapping. The Helmholtz loops consist of six concentric rings in twelve layers, the lower carrying 13 A, and the upper 1 A. The square conductors are six concentric rectangular loops of five layers, carrying 20 A. (b) Energy profiles along each cartesian direction, originating at the position of the energy minimum which for this structure is at −1 mm. (c-d) Energy contours in the XZ plane (c) and YZ plane (d) in units of μK.

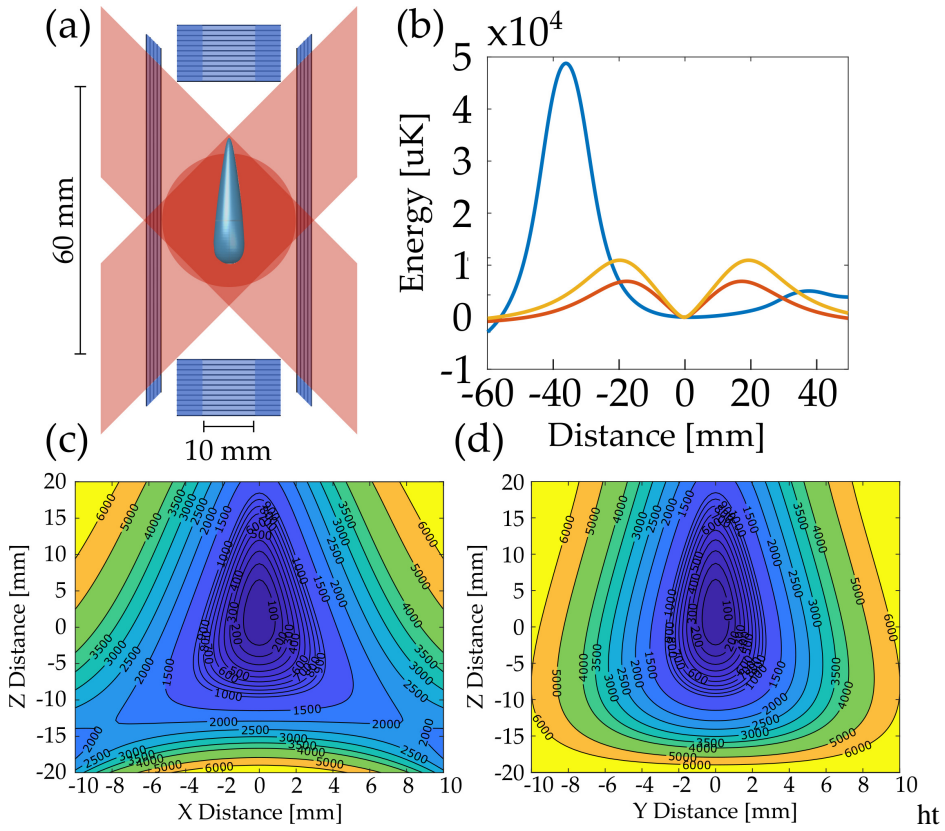

Fig. 4.8 Demonstration of the initial magnetic trap after radial compression such that the cloud can be pushed into the funnel structure. The geometry is the same structure as in Fig. 4.7, however the rectangular loops current has increased from 20 A to 30 A. (b) The energy profile, as in previous figure, measured from the energy minimum at -1 mm. (c-d) The energy contours measured in μK in the XZ plane (c) and YZ plane (d).

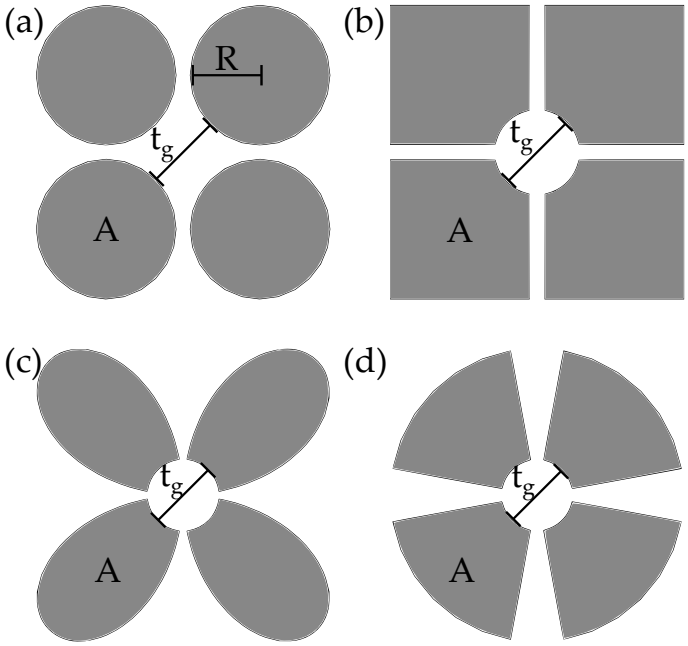

Fig. 4.9 Conductor cross sections examples for the lower end of the funnel trap. In order to have a like-for-like comparison, the geometry of the profiles are derivative of the first circular design. (a) Circular cross sections of radius R, with an internal void of t_g. In the limit of minimizing the distance between conductors in a four-fold symmetric design, these two parameters completely determine the geometry. (b) A square design where each conductor has an area A, as in the circular. (c) A clover-leaf design which has a more optimal current density distribution. (d) A segment design, which may be more useful for highly divergent imaging techniques.

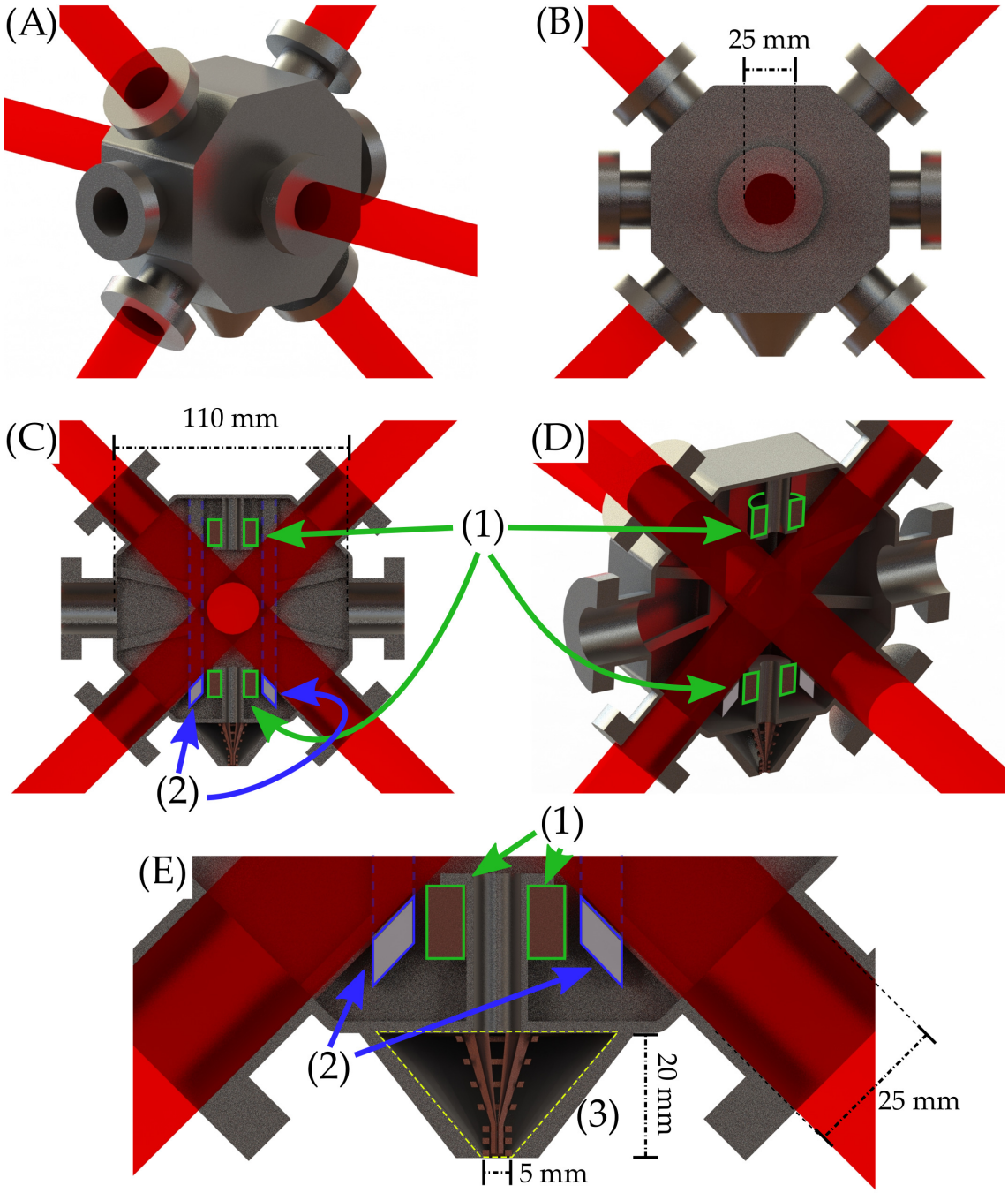

Fig. 4.10 A render of the proposed composite design for a funnel trap. (A-B) Exterior view of simple chamber design with fluted connectors for viewports. MOT beams are shown in red. (C-D) Section view of inside of main chamber. (1) Green outlines/arrows indicate the circular coils used in initial magnetic tap. (2) Blue outlines/arrows indicate the rectangular coils used in the initial magnetic trap. (E) Section view, zoomed into the area of the funnel-like region of the trap. Yellow region outlines region of lower pressure, ending in the final magnetic trap. The design aspect ratio is quite different to the schematic presented in Fig. 4.1, which is not surprising considering the orders of magnitude of temperature, magnetic field strength and cloud spatial extent spanned by each experimental stage. The results in a 'top-heavy' scheme in regards to the MOT and initial magnetic trap.

Chapter 5

Conclusion and Outlook

5.1 Thesis retrospective

The last 120 years has seen explosive growth in our understanding of atomic systems, the properties of light, and the interactions between the two. A century after the revolutionary development of quantum theory and quantum mechanics, experimenters now have the foundation and tools to cool and trap clouds of weakly interacting atoms. With this, we have seen the recent creation of Bose-Einstein Condensates, putting the field of ultracold atoms at the forefront of physics research. Ultracold atom laboratories, which we define as those concerned with the manipulation of individual or clouds of atoms at sub-millikelvin temperatures, are now a global feature in the physics landscape. However their aims and techniques are often distinct, arguably because there is still uncertainty as to the best way to achieve their goals. This is especially true within the field of quantum simulation and quantum computing [180, 181].

The work presented in this thesis looks to explore moving what were traditionally lab-bound experiments towards devices which are *portable*. Analogies are often drawn between this miniaturisation and the development of computer hardware over the years. The scope of applications for atomic systems outside of the lab are those which may be solved through precise measurement of magnetic, electric or gravitation fields; or which require the stability and accuracy of atom-based frequency standards. I direct the reader to the introduction of this thesis, or the major reviews in Refs. [32, 33, 73].

The main body of work in this thesis was the investigation of novel manufacturing techniques for ultracold atomic systems. Specifically, we considered how the relatively new process of *additive manufacturing*, or '3D-printing', may be used as a tool with which experimenters can produce complex and bespoke components. We can group the methodology followed into the production of conductive structures, the production of vacuum architectures and the development of a cold atom source.

In this final chapter we will give an overview of the processes and techniques used, with an emphasis on specific results obtained. This will be compared against the aims of the work, followed by a discussion of the areas where improvements could be made in future devices.

5.2 Thesis content overview

5.2.1 Cooling and trapping of atomic species

This chapter covered the physical background required to understand the basics of cooling and trapping of atomic species, specifically ^{87}Rb. Much of this physics is now well established, and so the topics followed the presentation as is common in typical texts on the topic.

The quantum picture of atomic structure was given, up to and including the nature of the hyperfine lines and Zeeman splitting. This allowed us to describe the semi-classic model of light-matter interaction, where light is considered a classical wave impinging on the quantum atom. Through addressing an appropriate choice of hyperfine levels, one can then use the scattering force to generate optical molasses, which when paired with magnetic fields allows for magneto-optical trapping. Purely magnetic trapping is then introduced, allowing for evaporative cooling to be carried out and finally, with some significant experimental work, Bose-Einstein condensation.

A review of various magnetic trapping structures is given, compared for the properties of the trap geometries they produce. Although it is difficult to predict exact atom cloud properties from such calculations, they provide a framework with which to consider the pros and cons of different architectures.

5.2.2 The Cylinder Trap

This chapter covers the design and testing of the cylinder trap, an additively manufactured structure built to generate the magnetic fields necessary for a magneto-optical trap. This work contributed to the publication *3D-printed components for quantum devices* [94].

The goal of this section was to develop a proof of principle experiment making use of additive manufactured structures as part of a quantum system. Two proposals were tested. In one a very simple CF16-compatible vacuum flange was printed using selective-laser melting techniques in an Al-Si-Mg alloy, with an ultra-high vacuum sealing knife edge cut into it in post-processing. The flange also underwent a post-processing treatment, called solution-heat treatment, which altered the microstructure of the material, depicted in Fig. 3.2, improving rigidity. This was placed onto a simple test vacuum setup, leak tested with a helium-based leak detector and then pumped down to UHV ($< 10^{-11}$ mbar) in a standard bake-out and cool procedure. No leaks were detected and UHV was achieved as measured on a standard low-pressure vacuum gauge.

The second proposal was to design and print a structure which would exist *within* a UHV environment and generate the fields necessary for a magneto-optical trap. With portability in mind, the following design aims were outlined:

- Production of $\sim 10^8$ cold atoms.
- Minimal electrical power consumption.
- Produces a close approximation to a quadrupole field.
- A mostly linear magnetic field in the trapping volume.
- Design achievable with standard 3D-printing capabilities.

- Connection to electrical feedthroughs.
- Adequate thermal mass to minimize deformity from joule heating.

These design aims were then evaluated against the considerations and constraints of additive manufacturing. As in production process, there are limits in what is achievable in terms of surface quality and feature resolution. As the process is a by-layer construction, one must also consider overhangs, warping and removal of excess power/material after printing.

An iterative design process was then carried out, between computer-aided design (CAD) software and finite-element calculations, to develop a structure which would fit around the volume defined by the three pairs of counter propagating beams. A design was settled on, which we now call the cylinder trap, having the best per-ampere field properties such as magnetic field gradient and the extent of its linear regime, while still fitting the above listed design aims. The design is shown in Fig. 3.3, showing simulations and measurement of the magnetic field it produces.

To test the structure, a simple cold-atom experiment was designed and constructed from scratch. While the flange test was successful, there was still some doubt as to whether the cylinder trap would outgas or survive the bake out process. To minimize the uncertainty in the measurements of the vacuum quality, the experiment used well known commercial laser systems and vacuum equipment. A compact optical breadboard of optics was constructed, and a simple imaging system designed for measurement[1]. A low footprint, simple computer control system was designed and implemented by laboratory partner W. Evans, making used of Arduino microcontrollers. This allowed significant time and power savings in comparison to common cold-atom control systems using often difficult to learn LabView software.

The vacuum system, shown in Fig. 3.9, was pumped down successfully to UHV pressures with the cylinder installed. The cylinder trap was measured, through absorption imaging, to capture upwards of 10^8 atoms with sub-Doppler temperatures on the order of $(20.1 \pm 0.2)\,\mu\mathrm{K}$ following molasses cooling and minimal electrical power consumption $\sim 100\,\mathrm{mW}$. By shrinking the optical beam size, down to 9 mm a miniature system was simulated for a speculation on future work. A brief comparison with a contemporary experiment was carried out, with uses externally mounted coils, to show the significance of the improvement.

Cylinder trap: discussion

The results of the cylinder trap experiment were very fruitful. They demonstrated, as far as we are aware, the first application of 3D printed conductors for use in a quantum device, both trapping a large atom number, and critically not being a detriment to the UHV conditions required in ultracold experiments.

Retrospectively it was disappointing that the failure in our vacuum gauge stopped us from producing an accurate measurement of the pressure. Additionally, it is likely that a slight beam misalignment inhibited us from reaching lower molasses temperature. Nevertheless as a proof of principle, the trap's success helps pave the way for additive manufacturing to become a common feature or method for ultracold and quantum devices. A more thorough discussion on the technique will be left until after the summary of the next chapter.

[1] Imaging systems were designed and optimized using OSLO optics software.

5.2.3 Blueprint for a Cold-Atom Source

Following the cylinder trap, this chapter considered a next-generation device with the specific aim to generate an even colder source of atoms. These atoms would be then transported or emitted to a secondary science chamber. This begins with an overview of atomic sources in general, highlighting how common issues with the background pressure, cycle time and final achieved atom number and temperature of such designs is limiting.

By describing a timeline of an atom cloud, starting with the emission of atoms from a dispenser to near-BEC phase-space densities, I discuss how mode matching of a magnetic trap to the MOT geometry could help improve atom-transfer efficiency. At each experimental stage example trap properties are given. These are collected either from the cylinder trap work or from contemporary sources, with the goal being to develop a set of design targets. This feeds into the introduction of *the funnel trap*: a three dimensional, multi-stage trap which more optimally traps atoms from a six-beam MOT, transfers to a pure magnetic trap and then transports atoms through a funnel-like structure to a region of very tight confinement where fast evaporative cooling can occur.

In parallel, the *coral chamber* is presented. This work was part of a larger collaboration between Sussex, Nottingham and industry partner Added Scientific. As the spiritual successor to the vacuum flange and cylinder trap, a vacuum containing structure was developed to test the principle of a fully printed component holding UHV conditions. The results are awaiting acceptance in a journal, but with an ArXiv pre-print available under the title *Additively manufactured ultra-high vacuum chamber below* 10^{-10} *mbar* [95]. The main result being the successful pump-down of the chamber to $< 10^{-10}$ mbar, and holding of $< 10^{-9}$ mbar for twenty-four hours with no active pumping. The unique coral-like outer skin allowed for a 50% mass reduction when compared to similar chamber sizes.

Continuing with the funnel trap, a series of calculations were carried out to design more optimal trapping geometries. Regimes such as maximum trap curvature, suppression of quartic field terms and fixing of trap depth were considered and compared. By then fixing a MOT geometry, it was quickly shown that most of these regimes were impossible to achieve without allowing conductors in 'forbidden' regions where beams would pass, or without significant currents.

A somewhat simple recirculated design was created instead. By successive calculations of coil density variations, an achievable design was reached which would magnetically capture atoms from a MOT. In-keeping with the aim of maximizing transfer efficiency, the trap designed has geometric properties comparable to that of a MOT of temperature 20 μK. Specifically the magnetic trap properties were: $f_{(x,y,z)} = (18, 22, 5)$ Hz with a minimum depth of ~ 1 mK with an Ioffe-Pritchard style trap configuration carrying 20 A and 13 A for the long and circular conductors, respectively.

In the highly-confining region, the conductor shape would likely be more significant as the atoms would be less than a millimeter away from the conductor surface. Finite element simulations were carried out with four conductor profiles, shown in Fig. 4.9. Effective trap properties were calculated and a concentric segment-like design was found to perform marginally better than other designs. This final trap region had the following calculated properties: $f_{x,y,z} = (1000, 1000, 200)$ Hz, with minimum depth of 4000 μK and a $B_{min} = 1$ G.

Finally, a speculative CAD model was designed and is presented in Fig. 4.10. An additively manufactured chamber is suggested for the main volume, allowing for supporting structures to be

created for the initial magnetic trap. A second conical-like chamber is connected, via a differential pumping tube, and contains the funnel structure and the final trapping region. Such a design would allow for a high vapor pressure region to exist where a MOT can be formed quickly and transferred to the first magnetic trap. Atoms can then be compressed and pushed through the tube and the funnel. The hottest atoms will likely be lost to the edges of the tube. The cloud will be then transferred to the highly confining final trap region where evaporative cooling occurs. Atoms can then either be propelled to a second region, or be interrogated in this secondary volume, benefiting from lower background collision rates.

Atom source: discussion

The specifics of additive manufacturing for quantum technology I will leave for the following section. Here I will discuss the outcome of the calculations and design work carried out in this chapter.

In retrospect, and considering the work in grating and reflector single-beam modes, it is highly possible that the funnel-like structure may be over-engineered. In technology it is often the case that *good enough* is often superior, in the end, to optimal or better performing devices.[2] The funnel trap very well may have a higher MOT atom number, and perhaps may achieve a final lower temperature, but the additional complications of more conductors and precise engineering require may make it prohibitive to construct.

However, the principle of a funnel to taper atoms is interesting and has been around since at least the turn of the millennium [83]. If proven to work experimentally with the suggested benefits of background pressure and final temperature, there would be a clear pathway to then integrating a grating-MOT to simplify the system further. With the recent improvements in vacuum material technology, in particular for atom chips, the highly heat-conductive substrates now available, discussed in the very end of Sec. 4.6, could make the design very achievable, both providing structural support to the three-dimensional funnel as well as quickly dissipating heat.

5.2.4 Additive manufacturing for quantum technology

Considering the work carried out in Refs. [92, 93], and through discussions with our peers in the field, it seemed that additive manufacturing would not at all be suitable for UHV applications. Uncertainties on material and surface quality, structural resilience, outgassing and air pockets were prohibitive to many to even attempt the technique. Especially considering that well established techniques already work.

The work presented here, and the papers derived from it, provide clear evidence as to the suitability of additively manufactured materials in ultracold atom experiments. We have shown not only that the structures printed can conduct sufficient currents to generate magnetic fields for a magneto-optical trap, but also that during operation there is no measurable pressure increase from outgassing. This was taken further with the coral chamber, proving that the components printed can be structurally sound enough to match up to commercial vacuum chambers, as well as being dense enough to block the diffusion of air through the material itself.

[2] See the Betamax vs VHS competition of the late 1970s to 1980s.

Considering the outlook of additive manufacturing in our field, there are distant prospects of combined ceramic and conductor processes, and there is the even greater goal of 3D-printed circuitry. One could envision chamber geometries where conductors and insulators are printed together as one monolithic component, combining trapping and vacuum structures in a miniature device.

A more realistic prospective today is the development of even more detailed vacuum systems for implementation into smaller devices. The proof of principle of additive manufacturing has been established. However it is still not completely clear of the importance of the post processing techniques employed to results, not to mention the outgassing detected at high temperatures in Ref. [95]. There is the scope for atomic magnetometry to provide the answer to some of these material questions [51], which can then be fed back into the manufacture process. Other printed materials are still yet to be tested too, such as titanium, stainless steel or even silver. The author hopes that the outlook of 3D-printing in application to quantum devices is significantly more optimistic than perhaps was the case at the beginning of the research.

Vacuum Pressure Retrospective While we have discussed vacuum pressure in regards to its effect on the trap lifetime, it is worth at this point having a brief retrospective discussion on the vacuum pressures actually required by quantum technology applications. The typical pressures aimed for in this work, $\sim 10^{-11}$ mbar, were originally driven by the highly sensitive work done by our research group as a whole. Each experiment depends critically on the lifetime of a BEC which is being used as a measurement tool. So the work in regards to the Cylinder Trap, Coral Chamber and Funnel Trap used this very high benchmark. However, such pressures are not at all necessary for 'good-enough' sensors which make use of thermal atoms trapped in MOT-environments with vacuum pressures on the order of 10^{-7-8} mbar. The author would like to emphasize that if the pressure requirements are relaxed, the cautious bake-out of the coral chamber may not be required at all. Without the risk of thermal-induced changes during bake-out, one could envision more adventurous exploration of other available materials and printing techniques.

The author speculates that it is in the region of 10^{-7-8} mbar that 3D printing could see significant gain in quantum technology, especially in regards to incredibly weight restrictive space and aerospace applications. The freedom to explore the broader catalog of materials available to SLM and similar printing techniques could allow researchers and product-designers to make significant mass reductions, and provide a pathway to exploit the ceramic-metal combinations discussed above. There are also potentially exciting advancements in polymer printing methods for vacuum applications discussed with our research partners in Added Scientific.

5.2.5 Results summary

The Cylinder Trap

- Production of a printed flange, leak tested without failure and pumped down to UHV successfully.
- Design and printing of monolithic structure, the cylinder trap, for in-vacuum use, producing fields for a MOT.

- Design of cold-atom experiment to test the cylinder.
- Capture of up to 10^8 atoms with sub-Doppler temperatures on the order of $(20.1 \pm 0.2)\,\mu\text{K}$.
- Minimal electrical power consumption achieved for the trap, $\sim 100\,\text{mW}$.

Funnel Trap and Coral Chamber

- Design and production of printed chamber, the coral chamber, as part of a larger collaboration.
- Chamber achieving $< 10^{-10}\,\text{mbar}$ pressures.
- Calculations of optimal trapping regimes for a next-generation device.
- Design of a recirculated-coil based magnetic trap to capture MOT atoms efficiently.
- Design, in CAD, of a multi-stage trapping ensemble, from MOT to ultra-cold temperature atoms, making use of a tapered funnel and differential pumping tube.

References

[1] E. F. Nichols and G. F. Hull. The Pressure Due to Radiation. (Second Paper.). *Phys. Rev. (Series I)*, 17:26–50, 1903.

[2] William D. Phillips. Nobel Lecture: Laser Cooling and Trapping of Neutral Atoms. *Rev. Mod. Phys.*, 70:721–741, 1998.

[3] Horst Schmidt-Böcking, Lothar Schmidt, Hans Jürgen Lüdde, Wolfgang Trageser, Alan Templeton, and Tilman Sauer. The Stern-Gerlach experiment revisited. *The European Physical Journal H*, 41(4):327–364, Nov 2016.

[4] M. Planck. 'The Origin and Development of the Quantum Theory', Nobel Prize in Physics Award Address, 1920, trans. H. T. Clarke and L. Silberstein (Oxford: Clarendon Press, 1922). *Reprinted in The World of the Atom*, 1966:496–500, 1922. cited By 1.

[5] John G. Cramer. The Transactional Interpretation of Quantum Mechanics. *Rev. Mod. Phys.*, 58:647–687, 1986.

[6] Albert Einstein. [Translated] Concerning an Heuristic Point of View Toward the Emission and Transformation of Light (1905). *American Journal of Physics*, 33(5):367, 1965.

[7] P. a. M. Dirac. The Quantum Theory of the Emission and Absorption of Radiation. *Proceedings of the Royal Society A: Mathematical, Physical and Engineering Sciences*, 114(767):243–265, 1927.

[8] G.P. Thomson and A. Reid. Diffraction of Cathode Rays by a Thin Film [1]. *Nature*, 119(3007):890, 1927. cited By 76.

[9] A.I.M. Rae. *Quantum Mechanics*. Taylor & Francis Group, 2008.

[10] N. Zettili. *Quantum Mechanics: Concepts and Applications*. Wiley, 2009.

[11] T.H. Maiman. Optical and Microwave-Optical Experiments in Ruby. *Physical Review Letters*, 4(11):564–566, 1960. cited By 159.

[12] T. W. Hänsch and A. L. Schawlow. Cooling of Gases by Laser Radiation. *Optics Communications*, 13(1):68–69, 1975.

[13] Carl E Wieman, Leo Hollberg, Carl E Wieman, and Leo Hollberg. Using Diode Lasers for Atomic Physics. *Review of Scientific Instruments*, 92(1):1–21, 1991.

[14] A. Ashkin. Acceleration and Trapping of Particles by Radiation Pressure. *Phys. Rev. Lett.*, 24:156–159, 1970.

[15] A. Ashkin. Atomic-Beam Deflection by Resonance-Radiation Pressure. *Physical Review Letters*, 25(19):1321–1324, 1970.

[16] A. Ashkin. Trapping of Atoms by Resonance Radiation Pressure. *Physical Review Letters*, 40(12):729–732, 1978.

[17] D. J. Wineland and Wayne M. Itano. Laser Cooling of Atoms. *Phys. Rev. A*, 20:1521–1540, 1979.

[18] William D. Phillips and Harold Metcalf. Laser Deceleration of an Atomic Beam. *Physical Review Letters*, 48(9):596–599, 1982.

[19] John Prodan, Alan Migdall, William D. Phillips, Ivan So, Harold Metcalf, and Jean Dalibard. Stopping Atoms with Laser Light. *Phys. Rev. Lett.*, 54:992–995, 1985.

[20] Steven Chu, L. Hollberg, J. E. Bjorkholm, Alex Cable, and A. Ashkin. Three-Dimensional Viscous Confinement and Cooling of Atoms by Resonance Radiation Pressure. *Phys. Rev. Lett.*, 55:48–51, 1985.

[21] William D. Phillips, John V. Prodan, and Harold J. Metcalf. Laser Cooling and Electromagnetic Trapping of Neutral Atoms. *Journal of the Optical Society of America B*, 2(11):1751, 1985.

[22] E. L. Raab, M. Prentiss, Alex Cable, Steven Chu, and D. E. Pritchard. Trapping of Neutral Sodium Atoms with Radiation Pressure. *Physical Review Letters*, 59(23):2631–2634, 1987.

[23] Paul D. Lett, Richard N. Watts, Christoph I. Westbrook, William D. Phillips, Phillip L. Gould, and Harold J. Metcalf. Observation of Atoms Laser Cooled below the Doppler Limit. *Phys. Rev. Lett.*, 61:169–172, 1988.

[24] A. M Steane and C. J Foot. Laser Cooling below the Doppler Limit in a Magneto-Optical Trap. *Europhysics Letters (EPL)*, 14(3):231–236, 1991.

[25] P. D. Lett, W. D. Phillips, S. L. Rolston, C. E. Tanner, R. N. Watts, and C. I. Westbrook. Optical Molasses. *J. Opt. Soc. Am. B*, 6(11):2084–2107, 1989.

[26] A. Aspect, E. Arimondo, R. Kaiser, N. Vansteenkiste, and C. Cohen-Tannoudji. Laser Cooling below the One-Photon Recoil Energy by Velocity-Selective Coherent Population Trapping. *Phys. Rev. Lett.*, 61:826–829, 1988.

[27] K. B. Davis, M. O. Mewes, and W. Ketterle. An Analytical Model for Evaporative Cooling of Atoms. *Applied Physics B Laser and Optics*, 60(2-3):155–159, 1995.

[28] M. H. Anderson, J. R. Ensher, M. R. Matthews, C. E. Wieman, and E. A. Cornell. Observation of Bose-Einstein Condensation in a Dilute Atomic Vapor. *Science*, 269(5221):198–201, 1995.

[29] KB B Davis, M.-O Mewes, MR R Andrews, van Druten NJ, DS S Durfee, DM M Kurn, W Ketterle, N J Van Druten, DS S Durfee, DM M Kurn, and % Ketterle. Bose-Einstein Condensation in a Gas of Sodium Atoms. *Physical review letters*, 75(22):3969–3973, 1995.

[30] C. C. Bradley, C. A. Sackett, J. J. Tollett, and R. G. Hulet. Evidence of Bose-Einstein Condensation in an Atomic Gas with Attractive Interactions. *Phys. Rev. Lett.*, 75:1687–1690, 1995.

[31] H. Perrin. Ultra Cold Atoms and Bose-Einstein Condensation for Quantum Metrology. *The European Physical Journal Special Topics*, 172(1):37–55, 2009.

[32] Kai Bongs, Michael Holynski, Jamie Vovrosh, Philippe Bouyer, Gabriel Condon, Ernst Rasel, Christian Schubert, Wolfgang P. Schleich, and Albert Roura. Taking Atom Interferometric Quantum Sensors from the Laboratory to Real-World Applications. *Nature Reviews Physics*, 1(12):731–739, 2019.

[33] Brynle Barrett, P. Gominet, Etienne Cantin, Laura Antoni-Micollier, Andrea Bertoldi, Baptiste Battelier, Philippe Bouyer, Jean Lautier, and Arnaud Landragin. Mobile and Remote Inertial Sensing with Atom Interferometers. *Proceedings of the International School of Physics "Enrico Fermi"*, 188 "Atom Interferometry":493, 2014.

[34] Steven Chu. Nobel Lecture: The Manipulation of Neutral Particles. *Rev. Mod. Phys.*, 70:685–706, 1998.

[35] Andrew D. Ludlow, Martin M. Boyd, Jun Ye, E. Peik, and P. O. Schmidt. Optical Atomic Clocks. *Rev. Mod. Phys.*, 87:637–701, 2015.

[36] W. Markowitz, R. Glenn Hall, L. Essen, and J. V. L. Parry. Frequency of Cesium in Terms of Ephemeris Time. *Phys. Rev. Lett.*, 1:105–107, 1958.

[37] Norman F Ramsey. History of Early Atomic Clocks. *Metrologia*, 42(3):S1–S3, 2005.

[38] Davide Calonico. Lasers, Cold Atoms and Atomic Clocks: Realizing the Second Today. In *European Physical Journal Web of Conferences*, volume 58 of *European Physical Journal Web of Conferences*, page 03002, 2013.

[39] Mark A. Kasevich, Erling Riis, Steven Chu, and Ralph G. DeVoe. RF Spectroscopy in an Atomic Fountain. *Phys. Rev. Lett.*, 63:612–615, 1989.

[40] Brynle Barrett, Rémy Geiger, Indranil Dutta, Matthieu Meunier, Benjamin Canuel, Alexandre Gauguet, Philippe Bouyer, and Arnaud Landragin. The Sagnac Effect: 20 Years of Development in Matter-Wave Interferometry. *Comptes Rendus Physique*, 15(10):875 – 883, 2014. The Sagnac effect: 100 years later.

[41] Alexander D. Cronin, Jörg Schmiedmayer, and David E. Pritchard. Optics and interferometry with atoms and molecules. *Rev. Mod. Phys.*, 81:1051–1129, 2009.

[42] Mark Kasevich and Steven Chu. Atomic Interferometry using Stimulated Raman Transitions. *Phys. Rev. Lett.*, 67:181–184, 1991.

[43] J. Lenz and S. Edelstein. Magnetic Sensors and their Applications. *IEEE Sensors Journal*, 6(3):631–649, June 2006.

[44] Alan Edelstein. Advances in Magnetometry. *Journal of Physics: Condensed Matter*, 19(16):165217, 2007.

[45] D. Budker, W. Gawlik, D. F. Kimball, S. M. Rochester, V. V. Yashchuk, and A. Weis. Resonant Nonlinear Magneto-Optical Effects in Atoms. *Rev. Mod. Phys.*, 74:1153–1201, 2002.

[46] Tim M. Tierney, Niall Holmes, Stephanie Mellor, José David López, Gillian Roberts, Ryan M. Hill, Elena Boto, James Leggett, Vishal Shah, Matthew J. Brookes, Richard Bowtell, and Gareth R. Barnes. Optically Pumped Magnetometers: From Quantum Origins to Multi-Channel Magnetoencephalography. *NeuroImage*, 199:598 – 608, 2019.

[47] Jacob Taylor, Paola Cappellaro, L Childress, Liang Jiang, Dmitry Budker, P. Hemmer, Amir Yacoby, R. Walsworth, and M. Lukin. High-Sensitivity Diamond Magnetometer with Nanoscale Resolution. *Nature Physics*, 4:810—-816, 2008.

[48] G. A. Gibson and S. Schultz. A High-Sensitivity Alternating-Gradient Magnetometer for use in Quantifying Magnetic Force Microscopy. *Journal of Applied Physics*, 69(8):5880–5882, 1991.

[49] E. H. Hall. On a New Action of the Magnet on Electric Currents. *American Journal of Mathematics*, 2(3):287–292, 1879.

[50] W G Jenks, S S H Sadeghi, and J P Wikswo. SQUIDs for Nondestructive Evaluation. *Journal of Physics D: Applied Physics*, 30(3):293–323, 1997.

[51] Amruta Gadge. *A Cold Atom Apparatus for the Microscopy of Thin Membranes*. PhD thesis, University of Nottingham, 2018.

[52] S. Wildermuth, S. Hofferberth, I. Lesanovsky, S. Groth, P. Krüger, J. Schmiedmayer, and I. Bar-Joseph. Sensing Electric and Magnetic Fields with Bose-Einstein Condensates. *Applied Physics Letters*, 88(26):264103, 2006.

[53] Stephan Wildermuth, Sebastian Hofferberth, Igor Lesanovsky, Elmar Haller, L. Mauritz Andersson, Sönke Groth, Israel Bar-Joseph, Peter Krüger, and Jörg Schmiedmayer. Microscopic Magnetic-Field Imaging. *Nature*, 435(7041):440, 2005.

[54] Antonio Acín, Immanuel Bloch, Harry Buhrman, Tommaso Calarco, Christopher Eichler, Jens Eisert, Daniel Esteve, Nicolas Gisin, Steffen J Glaser, Fedor Jelezko, Stefan Kuhr, Maciej Lewenstein, Max F Riedel, Piet O Schmidt, Rob Thew, Andreas Wallraff, Ian Walmsley, and Frank K Wilhelm. The Quantum Technologies Roadmap: a European Community View. *New Journal of Physics*, 20(8):080201, 2018.

[55] A Roadmap for Quantum Technologies in the UK, 2019. Published by Innovate UK and the Engineering and Physical Sciences Research Council on behalf of the Quantum Technologies Strategic Advisory Board.

[56] Fujio Shimizu, Kazuko Shimizu, and Hiroshi Takuma. Four-Beam Laser Trap of Neutral Atoms. *Opt. Lett.*, 16(5):339–341, 1991.

[57] B.M. Xu, X. Chen, J. Wang, and M.S. Zhan. Realization of a Single-Beam Mini Magneto-Optical Trap: A Candidate for Compact CPT Cold Atom-Clocks. *Optics Communications*, 281(23):5819 – 5823, 2008.

[58] K. I. Lee, J. A. Kim, H. R. Noh, and W. Jhe. Single-Beam Atom Trap in a Pyramidal and Conical Hollow Mirror. *Opt. Lett.*, 21(15):1177–1179, 1996.

[59] J.L. Bliss, K.G. Libbrecht, J. Kohel, R.J. Thompson, D.J. Seidel, W.M. Klipstein, and L. Maleki. Generation of a Cold Atom Beam from a Pyramidal Magneto-Optical Trap. In *Quantum Electronics and Laser Science Conference*, page QTuG19. Optical Society of America, 1999.

[60] Matthieu Vangeleyn, Paul F. Griffin, Erling Riis, and Aidan S. Arnold. Single-Laser, One Beam, Tetrahedral Magneto-Optical Trap. *Opt. Express*, 17(16):13601–13608, 2009.

[61] Xuejian Wu, Fei Zi, Jordan Dudley, Ryan J. Bilotta, Philip Canoza, and Holger Müller. Multiaxis Atom Interferometry with a Single-Diode Laser and a Pyramidal Magneto-Optical Trap. *Optica*, 4(12):1545–1551, 2017.

[62] Q. Bodart, S. Merlet, N. Malossi, F. Pereira Dos Santos, P. Bouyer, and A. Landragin. A Cold Atom Pyramidal Gravimeter with a Single Laser Beam. *Applied Physics Letters*, 96(13):134101, 2010.

[63] J. P. Cotter, J. P. McGilligan, P. F. Griffin, I. M. Rabey, K. Docherty, E. Riis, A. S. Arnold, and E. A. Hinds. Design and Fabrication of Diffractive Atom Chips for Laser Cooling and Trapping. *Applied Physics B*, 122(6):172, Jun 2016.

[64] C. C. Nshii, M. Vangeleyn, J. P. Cotter, P. F. Griffin, E. A. Hinds, C. N. Ironside, P. See, A. G. Sinclair, E. Riis, and A. S. Arnold. A Surface-Patterned Chip as a Strong Source of Ultracold Atoms for Quantum Technologies. *Nature Nanotechnology*, 8(5):321–324, 2013.

[65] Matthieu Vangeleyn, Paul F. Griffin, Erling Riis, and Aidan S. Arnold. Laser Cooling with a Single Laser Beam and a Planar Diffractor. *Opt. Lett.*, 35(20):3453–3455, 2010.

[66] James P. McGilligan, Paul F. Griffin, Rachel Elvin, Stuart J. Ingleby, Erling Riis, and Aidan S. Arnold. Grating chips for quantum technologies. *Scientific Reports*, 7(1):384, 2017.

[67] J. Fortagh, H. Ott, A. Grossmann, and C. Zimmermann. Miniaturized Magnetic Guide for Neutral Atoms. *Applied Physics B*, 70(5):701–708, May 2000.

[68] J. Denschlag, D. Cassettari, A. Chenet, S. Schneider, and J. Schmiedmayer. A Neutral Atom and a Wire: Towards Mesoscopic Atom Optics. *Applied Physics B*, 69(4):291–301, Oct 1999.

[69] Albrecht Haase, Donatella Cassettari, Björn Hessmo, and Jörg Schmiedmayer. Trapping Neutral Atoms with a Wire. *Phys. Rev. A*, 64:043405, 2001.

[70] Johannes Denschlag, Donatella Cassettari, and Jörg Schmiedmayer. Guiding Neutral Atoms with a Wire. *Phys. Rev. Lett.*, 82:2014–2017, 1999.

[71] J. Reichel, W. Hänsel, P. Hommelhoff, and T.W. Hänsch. Applications of Integrated Magnetic Microtraps. *Applied Physics B*, 72(1):81–89, 2001.

[72] József Fortágh and Claus Zimmermann. Magnetic Microtraps for Ultracold Atoms. *Rev. Mod. Phys.*, 79:235–289, 2007.

[73] Mark Keil, Omer Amit, Shuyu Zhou, David Groswasser, Yonathan Japha, and Ron Folman. Fifteen Years of Cold Matter on the Atom Chip: Promise, Realizations, and Prospects. *Journal of modern optics*, 63(18):1840–1885, Oct 2016.

[74] John Kitching. Chip-Scale Atomic Devices. *Applied Physics Reviews*, 5(3):031302, 2018.

[75] Jan Rudolph, Waldemar Herr, Christoph Grzeschik, Tammo Sternke, Alexander Grote, Manuel Popp, Dennis Becker, Hauke Müntinga, Holger Ahlers, Achim Peters, Claus Lämmerzahl, Klaus Sengstock, Naceur Gaaloul, Wolfgang Ertmer, and Ernst M Rasel. A High-Flux BEC Source for Mobile Atom Interferometers. *New Journal of Physics*, 17(6):065001, 2015.

[76] Paolo Manini, Andrea Conte, L Viale, A. Bonucci, Fabrizio Siviero, and L Caruso. A Novel Approach in UHV Pumping of Accelerators: The NEXTorr® Pump. *IPAC 2011 - 2nd International Particle Accelerator Conference*, 2011.

[77] Songbai Kang, Russell P. Mott, Kevin A. Gilmore, Logan D. Sorenson, Matthew T. Rakher, Elizabeth A. Donley, John Kitching, and Christopher S. Roper. A Low-Power Reversible Alkali Atom Source. *Applied Physics Letters*, 110(24):244101, 2017.

[78] Lara Torralbo-Campo, Graham D. Bruce, Giuseppe Smirne, and Donatella Cassettari. Light-Induced Atomic Desorption in a Compact System for Ultracold Atoms. *Scientific Reports*, 5(1):14729, 2015.

[79] D.S. Barker, E.B. Norrgard, N.N. Klimov, J.A. Fedchak, J. Scherschligt, and S. Eckel. Single-Beam Zeeman Slower and Magneto-Optical Trap Using a Nanofabricated Grating. *Phys. Rev. Applied*, 11:064023, 2019.

[80] W. Wohlleben, F. Chevy, K. Madison, and J. Dalibard. An Atom Faucet. *The European Physical Journal D - Atomic, Molecular, Optical and Plasma Physics*, 15(2):237–244, 2001.

[81] James R. Kellogg, Dennis Schlippert, James M. Kohel, Robert J. Thompson, David C. Aveline, and Nan Yu. A Compact High-Efficiency Cold Atom Beam Source. *Applied Physics B*, 109(1):61–64, 2012.

[82] Jaime Ramirez-Serrano, Nan Yu, James M. Kohel, James R. Kellogg, and Lute Maleki. Multistage Two-Dimensional Magneto-Optical Trap as a Compact Cold Atom Beam Source. *Opt. Lett.*, 31(6):682–684, 2006.

[83] B.K. Teo and G. Raithel. Magnetic Trapping of Cold Atoms in a Tapered Guide. In *Quantum Electronics and Laser Science Conference*, page QTuE2. Optical Society of America, 2002.

[84] C.F. Roos, P. Cren, J. Dalibard, and D. Gury-Odelin. A Source of Cold Atoms for a Continuously Loaded Magnetic Guide. *Physica Scripta*, T105(1):19, 2003.

[85] Ethan R. Elliott, Markus C. Krutzik, Jason R. Williams, Robert J. Thompson, and David C. Aveline. NASA's Cold Atom Lab (CAL): System Development and Ground Test status. *npj Microgravity*, 4(1):16, 2018.

[86] Vincent Ménoret, Pierre Vermeulen, Nicolas Le Moigne, Sylvain Bonvalot, Philippe Bouyer, Arnaud Landragin, and Bruno Desruelle. Gravity Measurements Below 10-9 g with a Transportable Absolute Quantum Gravimeter. *Scientific Reports*, 8(1):12300, 2018.

[87] Jason Williams, Sheng wey Chiow, Nan Yu, and Holger Müller. Quantum Test of the Equivalence Principle and Space-Time Aboard the International Space Station. *New Journal of Physics*, 18(2):025018, 2016.

[88] G.M. Tino, F. Sorrentino, D. Aguilera, B. Battelier, A. Bertoldi, Q. Bodart, K. Bongs, P. Bouyer, C. Braxmaier, L. Cacciapuoti, N. Gaaloul, N. Gürlebeck, M. Hauth, S. Herrmann, M. Krutzik, A. Kubelka, A. Landragin, A. Milke, A. Peters, E.M. Rasel, E. Rocco, C. Schubert, T. Schuldt, K. Sengstock, and A. Wicht. Precision Gravity Tests with Atom Interferometry in Space. *Nuclear Physics B - Proceedings Supplements*, 243-244:203 – 217, 2013. Proceedings of the IV International Conference on Particle and Fundamental Physics in Space.

[89] Tuan D. Ngo, Alireza Kashani, Gabriele Imbalzano, Kate T.Q. Nguyen, and David Hui. Additive Manufacturing (3D printing): A Review of Materials, Methods, Applications and Challenges. *Composites Part B: Engineering*, 143:172 – 196, 2018.

[90] Stewart Scott and Sol Omolayo. Application of Direct Laser Sintering for Manufacture of Synchrotron Components. *Proceedings of the MEDSI 2014 Conference, Melbourne, Australia*, 2014.

[91] Ashley R. Gans, Matthew M. Jobbins, David Y. Lee, and S. Alex Kandel. Vacuum Compatibility of Silver and Titanium Parts Made Using Three-Dimensional Printing. *Journal of Vacuum Science & Technology A*, 32(2):023201, 2014.

[92] Stéphane Jenzer, Manuel Alves, Nicolas Delerue, Alexandre Gonnin, Denis Grasset, Frederic Letellier-Cohen, Bruno Mercier, Eric Mistretta, Christophe Prevost, Alexis Vion, and Jean-Pierre Wilmes. Study of the suitability of 3D printing for Ultra-High Vacuum applications. *Journal of Physics: Conference Series*, 874:012097, 2017.

[93] Jamie Vovrosh, Georgios Voulazeris, Plamen G. Petrov, Ji Zou, Youssef Gaber, Laura Benn, David Woolger, Moataz M. Attallah, Vincent Boyer, Kai Bongs, and Michael Holynski. Additive Manufacturing of Magnetic Shielding and Ultra-High Vacuum Flange for Cold Atom Sensors. *Scientific Reports*, 8(1):2023, 2018.

[94] R. Saint, W. Evans, Y. Zhou, T. Barrett, T. M. Fromhold, E. Saleh, I. Maskery, C. Tuck, R. Wildman, F. Orucevic, and P. Krüger. 3D-Printed Components for Quantum Devices. *Scientific Reports*, 8(1):8368, 2018.

[95] N. Cooper, L. A. Coles, S. Everton, R. P. Campion, S. Madkhaly, C. Morley, W. Evans, R. Saint, P. Krüger, F. Oručević, C. Tuck, R. D. Wildman, T. M. Fromhold, and L. Hackermueller. Additively Manufactured Ultra-High Vacuum Chamber Below 10^{-10} mbar. *arXiv e-prints*, page arXiv:1903.07708, 2019.

[96] J. H. Metcalf and P. van der Straten. *Laser Cooling and Trapping*. Graduate Texts in Contemporary Physics. Springer, 1992.

[97] Peter van der Straten and Harold Metcalf. *Atoms and Molecules Interacting with Light: Atomic Physics for the Laser Era*. Cambridge University Press, 2016.

[98] W. Demtröder. *Atoms, Molecules and Photons: An Introduction to Atomic-, Molecular- and Quantum-physics*. Advanced texts in physics. Springer, 2006.

[99] C.J. Foot. *Atomic Physics*. Oxford master series in physics. Oxford University Press, 2005.

[100] Thomas J. Barrett. *An Apparatus for the Production of Bose-Einstein Condensates in Tunable Geometries on a Chip*. PhD thesis, University of Nottingham, 2017.

[101] C.S. Adams and E. Riis. Laser Cooling and Trapping of Neutral Atoms. *Progress in Quantum Electronics*, 21(1):1 – 79, 1997.

[102] D. A. Steck. Quantum and Atom Optics. [online] http://atomoptics-nas.uoregon.edu/~dsteck/teaching/quantum-optics/ revision 0.12.6, last updated 23 April 2019, accessed on 21 June 2020.

[103] D. A. Steck. Rubidium 87 D Line Data. [online] https://steck.us/alkalidata/ revision 2.1.5, 13 January 2015.

[104] Claude Cohen-Tannoudji. Manipulating Atoms with Photons. *Physica Scripta*, T76(1):33, 1998.

[105] J. F. Barry, D. J. McCarron, E. B. Norrgard, M. H. Steinecker, and D. Demille. Magneto-Optical Trapping of a Diatomic Molecule. *Nature*, 512(7514):286–289, 2014.

[106] Alejandra L. Collopy, Shiqian Ding, Yewei Wu, Ian A. Finneran, Loïc Anderegg, Benjamin L. Augenbraun, John M. Doyle, and Jun Ye. 3D Magneto-Optical Trap of Yttrium Monoxide. *Physical Review Letters*, 121(21):213201, 2018.

[107] Y. Shevy, D. S. Weiss, P. J. Ungar, and Steven Chu. Bimodal Speed Distributions in Laser-Cooled Atoms. *Phys. Rev. Lett.*, 62:1118–1121, 1989.

[108] J. Dalibard and C. Cohen-Tannoudji. Laser Cooling Below the Doppler Limit by Polarization Gradients: Simple Theoretical Models. *J. Opt. Soc. Am. B*, 6(11):2023–2045, 1989.

[109] D. Boiron, C. Triché, D. R. Meacher, P. Verkerk, and G. Grynberg. Three-Dimensional Cooling of Cesium Atoms in Four-Beam Gray Optical Molasses. *Phys. Rev. A*, 52:R3425–R3428, 1995.

[110] D. Boiron, A. Michaud, P. Lemonde, Y. Castin, C. Salomon, S. Weyers, K. Szymaniec, L. Cognet, and A. Clairon. Laser Cooling of Cesium Atoms in Gray Optical Molasses Down to 1.1 μk. *Phys. Rev. A*, 53:R3734–R3737, 1996.

[111] G Grynberg and J.-Y Courtois. Proposal for a Magneto-Optical Lattice for Trapping Atoms in Nearly-Dark States. *Europhysics Letters (EPL)*, 27(1):41–46, 1994.

[112] D. Rio Fernandes, F. Sievers, N. Kretzschmar, S. Wu, C. Salomon, and F. Chevy. Sub-Doppler Laser Cooling of Fermionic 40K Atoms in Three-Dimensional Gray Optical Molasses. *EPL (Europhysics Letters)*, 100(6):63001, 2012.

[113] Sara Rosi, Alessia Burchianti, Stefano Conclave, Devang S. Naik, Giacomo Roati, Chiara Fort, and Francesco Minardi. L-Enhanced Grey Molasses on the D2 Transition of Rubidium-87 Atoms. *Scientific Reports*, 8(1):1301, 2018.

[114] G D Bruce, E Haller, B Peaudecerf, D A Cotta, M Andia, S Wu, M Y H Johnson, B W Lovett, and S Kuhr. Sub-Doppler Laser Cooling of 40k with Raman Gray Molasses on the ${d}_{2}$ Line. *Journal of Physics B: Atomic, Molecular and Optical Physics*, 50(9):095002, 2017.

[115] Walther Gerlach and Otto Stern. Der experimentelle Nachweis der Richtungsquantelung im Magnetfeld. *Zeitschrift für Physik*, 9(1):349–352, 1922.

[116] John David Jackson. *Classical Electrodynamics*. Wiley, New York, NY, 3rd ed. edition, 1999.

[117] David J Griffiths. *Introduction to Electrodynamics; 4th ed.* Pearson, Boston, MA, 2013. Re-published by Cambridge University Press in 2017.

[118] T. Bergeman, Gidon Erez, and Harold J. Metcalf. Magnetostatic Trapping Fields for Neutral Atoms. *Phys. Rev. A*, 35:1535–1546, 1987.

[119] James Simpson, John Lane, Christopher Immer, and Robert Youngquist. Simple Analytic Expressions for the Magnetic Field of a Circular Current Loop. *Transactions on Magnetics, USA*, 2001.

[120] William H. Press and Saul A. Teukolsky. Elliptic Integrals. *Computers in Physics*, 4(1):92–96, 1990.

[121] Satinder S. Sidhu. Elliptic Integrals and Functions. *Computers in Physics*, 9(3):268–276, 1995.

[122] C. J. Pethick and H. Smith. *Bose–Einstein Condensation in Dilute Gases*. Cambridge University Press, 2nd edition, 2008.

[123] Inc. Wolfram Research. The Best-Known Properties and Formulas for Complete Elliptic Integrals. [online] Accessed: 2019-04-03 http://functions.wolfram.com/EllipticIntegrals/EllipticK/introductions/CompleteEllipticIntegrals/05/.

[124] Yuesen Chu. Numerical Calculation for the Magnetic Field in Current-Carrying Circular Arc Filament. volume 34, pages 502–504, 1998.

[125] Stephen Eckel, Daniel S. Barker, James A. Fedchak, Nikolai N. Klimov, Eric Norrgard, Julia Scherschligt, Constantinos Makrides, and Eite Tiesinga. Challenges to Miniaturizing Cold Atom Technology for Deployable Vacuum Metrology. 55(5):S182–S193, 2018.

[126] I. Maskery, N. T. Aboulkhair, A. O. Aremu, C. J. Tuck, I. A. Ashcroft, R. D. Wildman, and R. J M Hague. A Mechanical Property Evaluation of Graded Density Al-Si10-Mg Lattice Structures Manufactured by Selective Laser Mwelting. *Materials Science and Engineering A*, 670:264–274, 2016.

[127] Kaufui V. Wong and Aldo Hernandez. A Review of Additive Manufacturing. *ISRN Mechanical Engineering*, 2012:1–10, 2012.

[128] Yi Zhang, Linmin Wu, Xingye Guo, Stephen Kane, Yifan Deng, Yeon Gil Jung, Je Hyun Lee, and Jing Zhang. Additive Manufacturing of Metallic Materials: A Review. *Journal of Materials Engineering and Performance*, 27(1):1–13, 2018.

[129] How to Fix Warping. [online] Accessed 2019/10/22 https://ultimaker.com/en/resources/19537-how-to-fix-warping.

[130] Alexander P. Povilus, Caroline J. Wurden, Zak Vendeiro, Marcelo Baquero-Ruiz, and Joel Fajans. Vacuum Compatibility of 3D-Printed Materials. *Journal of Vacuum Science & Technology A: Vacuum, Surfaces, and Films*, 32(3):033001, 2014.

[131] Nesma T. Aboulkhair, Chris Tuck, Ian Ashcroft, Ian Maskery, and Nicola M. Everitt. On the Precipitation Hardening of Selective Laser Melted AlSi10Mg. *Metallurgical and Materials Transactions A: Physical Metallurgy and Materials Science*, 46(8):3337–3341, 2015.

[132] Yunjia Shi, Paul Rometsch, Kun Yang, Frank Palm, and Xinhua Wu. Characterisation of a Novel Sc and Zr Modified Al–Mg Alloy Fabricated by Selective Laser Melting. *Materials Letters*, 196:347–350, 2017.

[133] I. Maskery, N. T. Aboulkhair, M. R. Corfield, C. Tuck, A. T. Clare, R. K. Leach, R. D. Wildman, I. A. Ashcroft, and R. J.M. Hague. Quantification and Characterisation of Porosity in Selectively Laser Melted Al-Si10-Mg Using X-Ray Computed Tomography. *Materials Characterization*, 111:193–204, 2016.

[134] Hyperphysics. Resistivity and temperature coefficients, 2020. Accessed on 2020/01/03.

[135] G.L. Weissler and R.W. Carlson, editors. *Chapter 5: Production of Ultrahigh Vacuum*, volume 14 of *Methods in Experimental Physics*. Academic Press, 1980.

[136] Songbai Kang, Russell P. Mott, Kevin A. Gilmore, Logan D. Sorenson, Matthew T. Rakher, Elizabeth A. Donley, John Kitching, and Christopher S. Roper. A Low-Power Reversible Alkali Atom Source. *Applied Physics Letters*, 110(24):244101, 2017.

[137] E. B. Norrgard, D. S. Barker, J. A. Fedchak, N. Klimov, J. Scherschligt, and S. Eckel. Note: A 3D-Printed Alkali Metal Dispenser. *Review of Scientific Instruments*, 89(5):056101, 2018.

[138] Hélène Perrin, Pierre Lemonde, Franck Pereira dos Santos, Vincent Josse, Bruno Tolra, Frédéric Chevy, and Daniel Comparat. Application of Lasers to Ultra-Cold Atoms and Molecules. *Comptes Rendus Physique - C R PHYS*, 12:417–432, 2011.

[139] Carl E. Wieman and Leo Hollberg. Using Diode Lasers for Atomic Physics. *Review of Scientific Instruments*, 62(1):1–20, 1991.

[140] A. G. Truscott, N. R. Heckenberg, and H. Rubinsztein-Dunlop. Frequency Stabilised Grating Feedback Laser Diode for Atom Cooling Applications. *Optical and Quantum Electronics*, 31(5):417–430, Jul 1999.

[141] Xingkai Lang, Peng Jia, Yongyi Chen, Li Qin, Lei Liang, Chao Chen, Yubing Wang, Xiaonan Shan, Yongqiang Ning, and Lijun Wang. Advances in Narrow Linewidth Diode Lasers. *Science China Information Sciences*, 62, 2019.

[142] S. Saito and Y. Yamamoto. Direct Observation of Lorentzian Lineshape of Semiconductor Laser and Linewidth Reduction with External Grating Feedback. *Electronics Letters*, 17(9):325–327, April 1981.

[143] M. Fleming and A. Mooradian. Spectral Characteristics of External-Cavity Controlled Semiconductor Lasers. *IEEE Journal of Quantum Electronics*, 17(1):44–59, January 1981.

[144] McCarron, D. A Guide to Acousto-Optic Modulators. https://pdfs.semanticscholar.org/9058/09436bc6a2fb3593f98a3c0bddeda35260ad.pdf, 2007. Technical report.

[145] E. A. Donley, T. P. Heavner, F. Levi, M. O. Tataw, and S. R. Jefferts. Double-Pass Acousto-Optic Modulator System. *Review of Scientific Instruments*, 76(6):063112, 2005.

[146] Nabeel A. Riza. Scanning Heterodyne Optical Interferometers. *Review of Scientific Instruments*, 67(7):2466–2476, 1996.

[147] Daryl W. Preston. Doppler-Free Saturated Absorption: Laser Spectroscopy. *American Journal of Physics*, 64(11):1432–1436, 1996.

[148] W. Demtröder. *Laser Spectroscopy: Basic Concepts and Instrumentation*. Advanced Texts in Physics. Springer Berlin Heidelberg, 2002.

[149] David A. Smith and Ifan G. Hughes. The Role of Hyperfine Pumping in Multilevel Systems Exhibiting Saturated Absorption. *American Journal of Physics*, 72(5):631–637, 2004.

[150] Joel A. Silver. Frequency-Modulation Spectroscopy for Trace Species Detection: Theory and Comparison Among Experimental Methods. *Appl. Opt.*, 31(6):707–717, 1992.

[151] W. Ketterle and M. W. Zwierlein. Making, Probing and Understanding Ultracold Fermi Gases. *Proceedings of the International School of Physics "Enrico Fermi"*, 164(June 2006):95–287, 2006.

[152] David A. Smith, Simon Aigner, Sebastian Hofferberth, Michael Gring, Mauritz Andersson, Stefan Wildermuth, Peter Krüger, Stephan Schneider, Thorsten Schumm, and Jörg Schmiedmayer. Absorption Imaging of Ultracold Atoms on Atom Chips. *Opt. Express*, 19(9):8471–8485, 2011.

[153] G. Reinaudi, T. Lahaye, Z. Wang, and D. Guéry-Odelin. Strong Saturation Absorption Imaging of Dense Clouds of Ultracold Atoms. *Opt. Lett.*, 32(21):3143–3145, 2007.

[154] Wolfgang Muessel, Helmut Strobel, Maxime Joos, Eike Nicklas, Ion Stroescu, Jirí Tomkovic, David B. Hume, and Markus K. Oberthaler. Optimized Absorption Imaging of Mesoscopic Atomic Clouds. *Applied Physics B*, 113(1):69–73, 2013.

[155] W. Ketterle, D. S. Durfee, and D. M. Stamper-Kum. Making, probing and understanding Bose-Einstein condensates. *Proceedings of the International School of Physics "Enrico Fermi"*, 140(June 2006):67 – 176, 1992.

[156] Wolfgang Petrich, Michael H. Anderson, Jason R. Ensher, and Eric A. Cornell. Behavior of Atoms in a Compressed Magneto-Optical Trap. *J. Opt. Soc. Am. B*, 11(8):1332–1335, 1994.

[157] Jiho Noh, Sung Jong Park, Chang Yong Park, Won-Kyu Lee, Dai-Hyuk Yu, and Jongchul Mun. High-Performance Experimental Apparatus for Large Atom Number 87-Rb Bose-Einstein Condensates. *Journal of the Korean Physical Society*, 61(7):1021–1027, 2012.

[158] S. N. Atutov, R. Calabrese, V. Guidi, B. Mai, A. G. Rudavets, E. Scansani, L. Tomassetti, V. Biancalana, A. Burchianti, C. Marinelli, E. Mariotti, L. Moi, and S. Veronesi. Fast and Efficient Loading of a Rb Magneto-Optical Trap Using Light-Induced Atomic Desorption. *Phys. Rev. A*, 67:053401, 2003.

[159] B. P. Anderson and M. A. Kasevich. Loading a Vapor-Cell Magneto-Optic Trap Using Light-Induced Atom Desorption. *Phys. Rev. A*, 63:023404, 2001.

[160] C. Klempt, T. van Zoest, T. Henninger, O. Topic, E. Rasel, W. Ertmer, and J. Arlt. Ultraviolet Light-Induced Atom Desorption for Large Rubidium and Potassium Magneto-Optical Traps. *Phys. Rev. A*, 73:013410, 2006.

[161] L. You and M. Holland. Ballistic Expansion of Trapped Thermal Atoms. *Phys. Rev. A*, 53:R1–R4, 1996.

[162] S. Pradhan and B. N. Jagatap. Measurement of Temperature of Laser Cooled Atoms by One-Dimensional Expansion in a Magneto-Optical Trap. *Review of Scientific Instruments*, 79(1):013101, 2008.

[163] C. D. Wallace, T. P. Dinneen, K. Y. N. Tan, A. Kumarakrishnan, P. L. Gould, and J. Javanainen. Measurements of Temperature and Spring Constant in a Magneto-Optical Trap. *J. Opt. Soc. Am. B*, 11(5):703–711, 1994.

[164] Rowan W. G. Moore, Lucie A. Lee, Elizabeth A. Findlay, Lara Torralbo-Campo, Graham D. Bruce, and Donatella Cassettari. Measurement of Vacuum Pressure with a Magneto-Optical Trap: A Pressure-Rise Method. *Review of Scientific Instruments*, 86(9):093108, 2015.

[165] Magnus Haw, Nathan Evetts, Will Gunton, Janelle Van Dongen, James L. Booth, and Kirk W. Madison. Magneto-Optical Trap Loading Rate Dependence on Trap Depth and Vapor Density. *J. Opt. Soc. Am. B*, 29(3):475–483, 2012.

[166] T. Arpornthip, C. A. Sackett, and K. J. Hughes. Vacuum-Pressure Measurement Using a Magneto-Optical Trap. *Phys. Rev. A*, 85:033420, 2012.

[167] J. A. Rushton, M. Aldous, and M. D. Himsworth. Contributed Review: The Feasibility of a Fully Miniaturized Magneto-Optical Trap for Portable Ultracold Quantum Technology. *Review of Scientific Instruments*, 85(12):121501, 2014.

[168] M. De Angelis, M. C. Angonin, Q. Beaufils, Ch Becker, A. Bertoldi, K. Bongs, T. Bourdel, P. Bouyer, V. Boyer, S. Dörscher, H. Duncker, W. Ertmer, T. Fernholz, T. M. Fromhold, W. Herr, P. Krüger, Ch Kürbis, C. J. Mellor, F. Pereira Dos Santos, A. Peters, N. Poli, M. Popp, M. Prevedelli, E. M. Rasel, J. Rudolph, F. Schreck, K. Sengstock, F. Sorrentino, S. Stellmer, G. M. Tino, T. Valenzuela, T. J. Wendrich, A. Wicht, P. Windpassinger, and P. Wolf. ISense: A Portable Ultracold-Atom-Based Gravimeter. *Procedia Computer Science*, 7:334–336, 2011.

[169] A. Camara, R. Kaiser, and G. Labeyrie. Scaling Behavior of a Very Large Magneto-Optical Trap. *Physical Review A - Atomic, Molecular, and Optical Physics*, 90(6):2–9, 2014.

[170] Savas Dimopoulos, Peter W. Graham, Jason M. Hogan, and Mark A. Kasevich. Testing General Relativity with Atom Interferometry. *Phys. Rev. Lett.*, 98:111102, 2007.

[171] K. Dieckmann, R. J.C. Spreeuw, M. Weidemüller, and J. T.M. Walraven. Two-Dimensional Magneto-Optical Trap as a Source of Slow Atoms. *Physical Review A - Atomic, Molecular, and Optical Physics*, 58(5):3891–3895, 1998.

[172] J. Schoser, A. Batär, R. Löw, V. Schweikhard, A. Grabowski, Yu B. Ovchinnikov, and T. Pfau. Intense Source of Cold Rb Atoms from a Pure Two-Dimensional Magneto-Optical Trap. *Physical Review A - Atomic, Molecular, and Optical Physics*, 66(2):1–10, 2002.

[173] Saptarishi Chaudhuri, Sanjukta Roy, and C. S. Unnikrishnan. Realization of an Intense Cold Rb Atomic Beam Based on a Two-Dimensional Magneto-Optical Trap: Experiments and Comparison with Simulations. *Physical Review A - Atomic, Molecular, and Optical Physics*, 74(2), 2006.

[174] E. Pedrozo-Peñafiel, F. Vivanco, P. Castilho, R. R. Paiva, K. M. Farias, and V. S. Bagnato. Direct Comparison Between a Two-Dimensional Magneto-Optical Trap and a Zeeman Slower as Sources of Cold Sodium Atoms. *Laser Physics Letters*, 13(6), 2016.

[175] J. Lee, J. A. Grover, L. A. Orozco, and S. L. Rolston. Sub-Doppler Cooling of Neutral Atoms in a Grating Magneto-Optical Trap. *J. Opt. Soc. Am. B*, 30(11):2869–2874, 2013.

[176] J. Alibert, B. Décamps, M. Bordoux, B. Allard, and A. Gauguet. A Millimeter Magnetic Trap for a Dual (85Rb and 87Rb) Species Atom Interferometer. *Review of Scientific Instruments*, 88(11):113115, 2017.

[177] Alan L. Migdall, John V. Prodan, William D. Phillips, Thomas H. Bergeman, and Harold J. Metcalf. First Observation of Magnetically Trapped Neutral Atoms. *Physical Review Letters*, 54(24):2596–2599, 1985.

[178] S.P. Ram, S.K. Tiwari, S.R. Mishra, and H.S. Rawat. Optimization of Transfer of Laser-Cooled Atom Cloud to a Quadrupole Magnetic Trap. *Pramana - Journal of Physics*, 82(2):419–423, 2014. cited By 0.

[179] Ritayan Roy, Paul C. Condylis, Vindhiya Prakash, Daniel Sahagun, and Björn Hessmo. A Minimalistic and Optimized Conveyor Belt for Neutral Atoms. *Scientific Reports*, 7(1):1–8, 2017.

[180] Immanuel Bloch, Jean Dalibard, and Sylvain Nascimbène. Quantum Simulations with Ultracold Quantum Gases. *Nature Physics*, 8(4):267–276, 2012.

[181] Bjoern Lekitsch, Sebastian Weidt, Austin G. Fowler, Klaus Mølmer, Simon J. Devitt, Christof Wunderlich, and Winfried K. Hensinger. Blueprint for a Microwave Trapped Ion Quantum Computer. *Science Advances*, 3(2), 2017.